Extreme Ground Motions and Yucca Mountain

U.S. Department of the Interior
U.S. Geological Survey

U.S. Department of the Interior
SALLY JEWELL, Secretary

U.S. Geological Survey
Suzette M. Kimball, Acting Director

U.S. Geological Survey, Reston, Virginia: 2013

Cover.   Yucca mountain crest with a dusting of snow, looking north. Photo from the Department
of Energy, Office of Civilian Radioactive Waste Management.

Contents

Figures

Tables

Abbreviations, Acronyms, and Symbols

a_{rms}	Root-mean-square acceleration
DEM	Digital elevation model
$\Delta\sigma$	Stress drop for a crustal earthquake
DFS	Doser/Fridrich/Swan
DOE	U.S. Department of Energy
DSHA	Deterministic seismic hazard analysis
ECRB	Enhanced Characterization of the Repository Block
ESF	Exploratory Studies Facility
ExGM	Extreme ground motions
FGS	Fragile geologic structure
γ	High-frequency spectral decay rate
g	Acceleration due to gravity
GMC	Ground motion characterization
GMP	Ground-motion prediction
GMPE	Ground motion prediction equation
HLW	High level waste
LMT	Lower mean tuff
m/s	Meters per second
M	Moment magnitude
M_0	Seismic moment
m_b	Body-wave magnitude
NGA	New Generation Attenuation (a project to update ground-motion prediction equations)
NTS	Nevada Test Site
OCRWM	Office of Civilian Radioactive Waste Management
PBR	Precariously balanced rock
pdf	Probability distribution functions
PGA	Peak ground acceleration
PGV	Peak ground velocity
PiHS	Points in hazard space
PSHA	Probabilistic seismic hazard analysis
PVHA	Probabilistic volcanic hazard analysis
SCEC	Southern California Earthquake Center
SCF	Solitario Canyon Fault
SH95	Nevada State Highway 95
SSC	Seismic source characterization
UGM	Unexceeded ground motions
U_{max}	largest reported vertical displacement
U_{mean}	mean vertical displacement
UMT	upper mean tuff
UNE	underground nuclear explosion
VML	varnish microlamination

V_{S30} time-weighted average of shear-wave velocity from the surface to a depth of 30 m

ω angular frequency

WWSSN   World Wide Standardized Seismograph Network

YMP   Yucca Mountain Project

Extreme Ground Motions and Yucca Mountain

By Thomas C. Hanks[1] (chair), Norman A. Abrahamson,[2] Jack W. Baker,[3] David M. Boore,[1] Mark Board,[4] James N. Brune,[5] C. Allin Cornell,[6] and John W. Whitney[1]

Our interest's on the dangerous edge of things.—Robert Browning

Introduction

Yucca Mountain is the designated site of the underground repository for the United States' high-level radioactive waste (HLW), consisting of commercial and military spent nuclear fuel, HLW derived from reprocessing of uranium and plutonium, surplus plutonium, and other nuclear-weapons materials. Yucca Mountain straddles the western boundary of the Nevada Test Site, where the United States has tested nuclear devices since the 1950s, and is situated in an arid, remote, and thinly populated region of Nevada, ~100 miles northwest of Las Vegas (fig. 1).

Yucca Mountain lies within the extensional regime of the Basin and Range Province, in the southwestern Nevada volcanic field. It is built of a sequence of middle-Miocene volcanic rocks, the product of massive ash-flow tuffs effluent from the Timber Mountain Caldera during ~14–11 Ma. The volcanic units underlying Yucca Mountain have been back-tilted to the east and offset ~300 m by down-to-the-west normal faulting along the west-dipping Solitario Canyon Fault (fig. 2). Seismic, tectonic, and volcanic activity continue to the present day but at rates much lower than those of the middle Miocene and also at rates much lower than those in currently active tectonic terrains.

Yucca Mountain was originally considered as a potential underground repository of HLW because of its thick units of unsaturated rocks, with the repository horizon being not only ~300 m above the water table but also ~300 m below the Yucca Mountain crest (Winograd, 1974). The fundamental rationale for a geologic (underground) repository for HLW is to securely isolate these materials from the environment and its inhabitants to the greatest extent possible and for very long periods of time.

Once the repository is closed, decades to centuries after all the HLW is emplaced, the essential concern is the integrity of the 40.6 miles of emplacement drifts containing the canisters of HLW. The principal concern has always been—and still is—penetration of percolating groundwater into the emplacement drifts, driven possibly by wetter climates than the present one, that will corrode the canisters, dissolve and transport the exposed radionuclides, and carry them to the water table below. That this will happen is not at issue, given long enough periods of time; what matters is "just how much water gets into the mountain, exactly where it goes once it does, how fast it gets to where it is going, and its temperature and chemical composition once it gets there"(Hanks and others, 1999).

---

1 U.S. Geologicial Survey
2 Pacific Gas & Electric Co.
3 Stanford University
4 Hecla Mining Co.
5 University of Nevada, Reno
6 Deceased
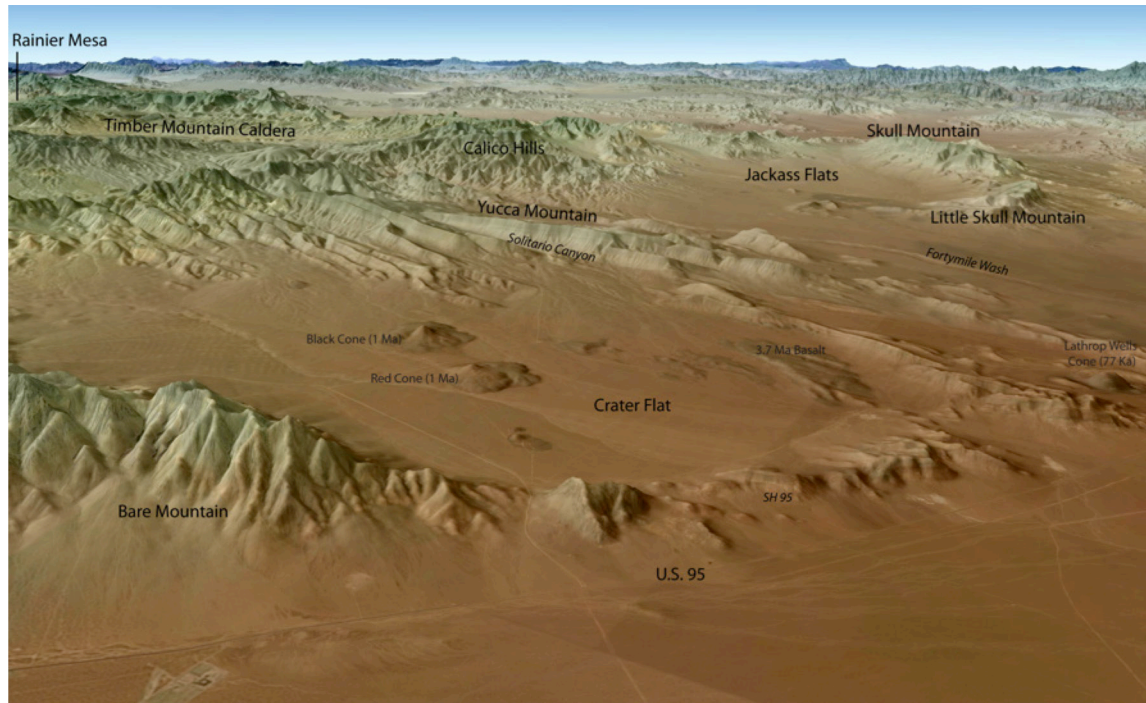
Figure 1. Google Earth image overlain on a digital elevation map, color-coded according to elevation, looking northeast over Bare Mountain and Crater Flat to Yucca Mountain and beyond, southwestern Nevada. Pahute Mesa lies off this image to the left, northwest of Rainier Mesa, of which only the southern end is shown. Image by J. Luke Blair, U.S. Geological Survey.

Given the present climate conditions and what is known about the current hydrologic system and conditions around and in the mountain itself, one would anticipate that the rates of infiltration, corrosion, and transport would be very low—except for the possibility that repository integrity might be compromised by low-probability disruptive events, which include earthquakes, strong ground motion, and (or) a repository-piercing volcanic intrusion/eruption. Probabilistic Seismic Hazard Analysis (PSHA) for Yucca Mountain was completed in 1998. The procedures, methods, and results of that PSHA are described in Stepp and others (2001), mostly in the context of a hazard level of 10^{-4} per year for ground motion at Point A, a hypothetical, reference rock-outcrop site with shear-wave velocity and attenuation properties thought to hold at the elevation of the emplacement drifts within the mountain. Probabilistic Volcanic Hazard Analysis (PVHA) was conducted for Yucca Mountain in the 1990s (CRWMS M&O, 1996), and an update of that study with much new data was recently completed (Sandia National Laboratory, 2008).
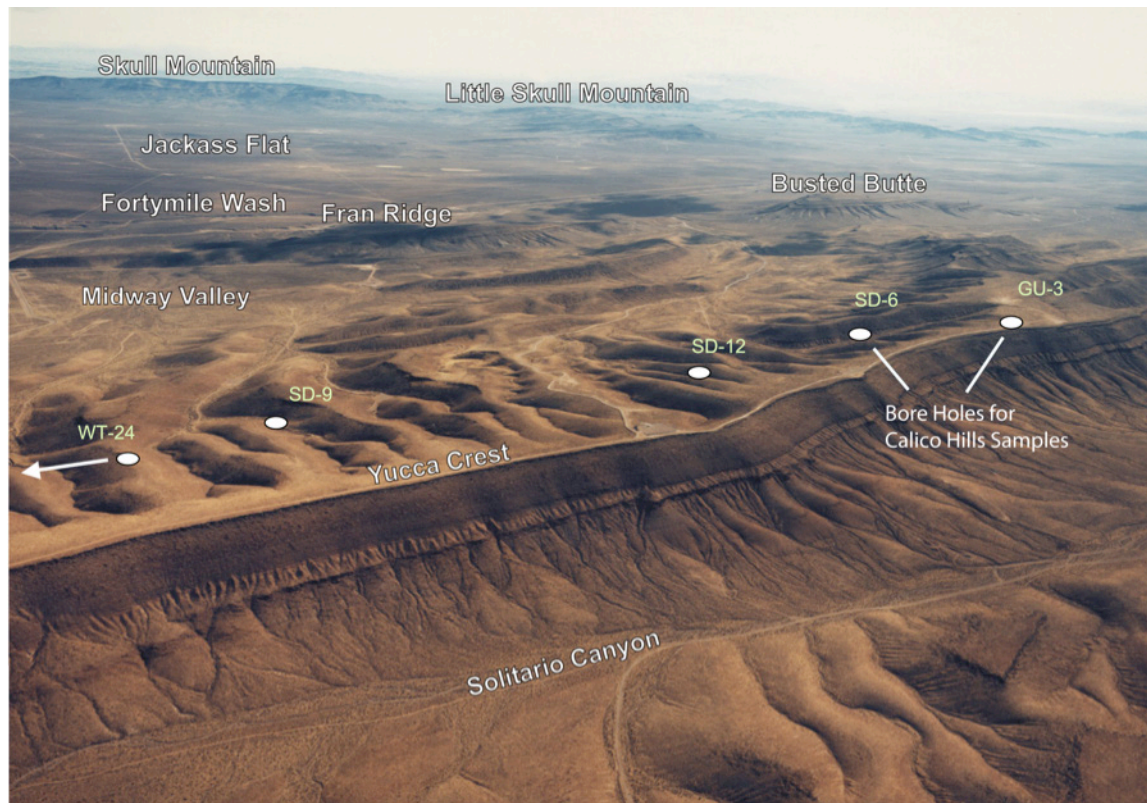
Figure 2. Aerial photo looking southeast across the steep west face of Yucca Mountain, the ~10-million-year-old scarp of the Solitario Canyon Fault at its base. The cliff-forming units are the Tiva Canyon Tuff, which forms the Yucca Mountain crest, and the Topopah Spring Tuff at midslope, the "Middle Ledge." Borehole locations are where the weakest samples of tuffs from the Calico Hill Formation were taken to determine their mechanical strength and energy-dissipation properties. From Lockner and Morrow (2008), modified from Andrews and others (2007).

Extreme ground motions, as we use the phrase in this report, refer to the extremely large amplitudes of earthquake ground motion that arise at extremely low probabilities of exceedance (hazard). They first came to our attention when the 1998 probabilistic seismic hazard analysis for Yucca Mountain was extended to a hazard level of 10^{-8}/yr (a 10^{-4}/yr probability for a 10^4-year repository "lifetime"). In its time, the 1998 Yucca Mountain PSHA was the most complex PSHA ever undertaken. It was the first PSHA to implement the Level-4 procedures of the Senior Seismic Hazard Analysis Committee (SSHAC, 1997). Informally known as the SSHAC Guidelines, SSHAC (1997) is primarily devoted to the theory and practice of expressing, aggregating, and quantifying expert opinion in the presence of uncertainty. In practice, this has turned out to be a complicated and time-consuming process (Hanks and others, 2009). Analysis and inclusion of both aleatory and epistemic uncertainty were significant and time-consuming aspects of the 1998 PSHA, which took place over three years and involved several dozen scientists, engineers, and analysts.

Aleatory uncertainty (from the latin word for dice, *alea*) measures the random variability in a set of observations about an average value, fixed by our present knowledge and available physical models that predict these observations. It might be the variability of earthquake stress drops for some earthquake selected for its relevance to Yucca Mountain, for example. Epistemic uncertainty, a concept less familiar and often perplexing to earth scientists, measures the difference among viable alternative models capable of explaining the same observations. As its Greek root (*episteme*) suggests, epistemic

uncertainty arises from incomplete knowledge, our ignorance of how the Earth works to generate earthquake ground motion, for example.

Because of these uncertainties, the 1998 Yucca Mountain PSHA provides for progressively higher ground motions as it is extended to progressively lower hazard levels: at mean hazard levels of 10^{-6}/yr, 10^{-7}/yr, and 10^{-8}/yr, the resulting peak ground accelerations (PGA) are 3 g, 6 g, and 11 g, (figure 3), and peak ground velocities (PGV) are 3 m/s, 6.5 m/s, and 13 m/s (figure 4) at Point A. These *extreme ground motions*, the consequence of untruncated ground-motion distribution functions taken to very low probability levels, have generated considerable consternation in the scientific, engineering, and regulatory communities: the upper end of these PGVs and PGAs have never been recorded for earthquakes, present exceptional challenges to the design and construction of underground facilities, and are regarded by most qualified seismologists as physically unrealizable, in part because of research described in this report.

In response to these concerns, the Science and Technology Program (S&T) in the Office of Civilian Radioactive Waste Management (OCRWM) of the United States Department of Energy (DOE) formed a committee in September 2003 to investigate the nature and plausibility of these extreme ground motions. The Extreme Ground Motion Committee (ExGMCom; table 1) took on as its first order of business a comprehensive assessment of extreme ground motions across many disciplines of the earth sciences, achieved through the Workshop on Extreme Ground Motions at Yucca Mountain, held in Menlo Park, California, August 23–25, 2004. The heart of this workshop was the 29 presentations made over three days, although the commentary and criticism of all the invited participants figured prominently in the outcome. The report on the workshop (Hanks and others, 2006) includes a written summary of all the presentations together with findings and recommendations; it also includes, in a lengthy appendix, short papers written by the invited speakers on the topics of their presentations.

While not formally published until 2006, the workshop report was available in draft form in June 2005, and it laid out the basic framework of the extreme ground motion (ExGM) research program. It included three areas of emphasis: the physical limits to ground motion, unexceeded ground motions, and frequency of occurrence of ground-motion amplitudes (such as PGA and PGV, or source properties related to them, like stress drops and faulting displacements). The DOE then launched the ExGM research program as a 5-year program, funded at $1 million per year.

The DOE required that ExGM engage the broad earth-science community, which was effected through the Southern California Earthquake Center (SCEC). In September 2005, approximately 100 SCEC scientists met for three days (September 8–10) after the SCEC Annual Meeting to discuss and review the workshop draft report. The SCEC written review of the workshop report, prepared by Paul Somerville, was taken into account in preparing the final report (Hanks and others, 2006).
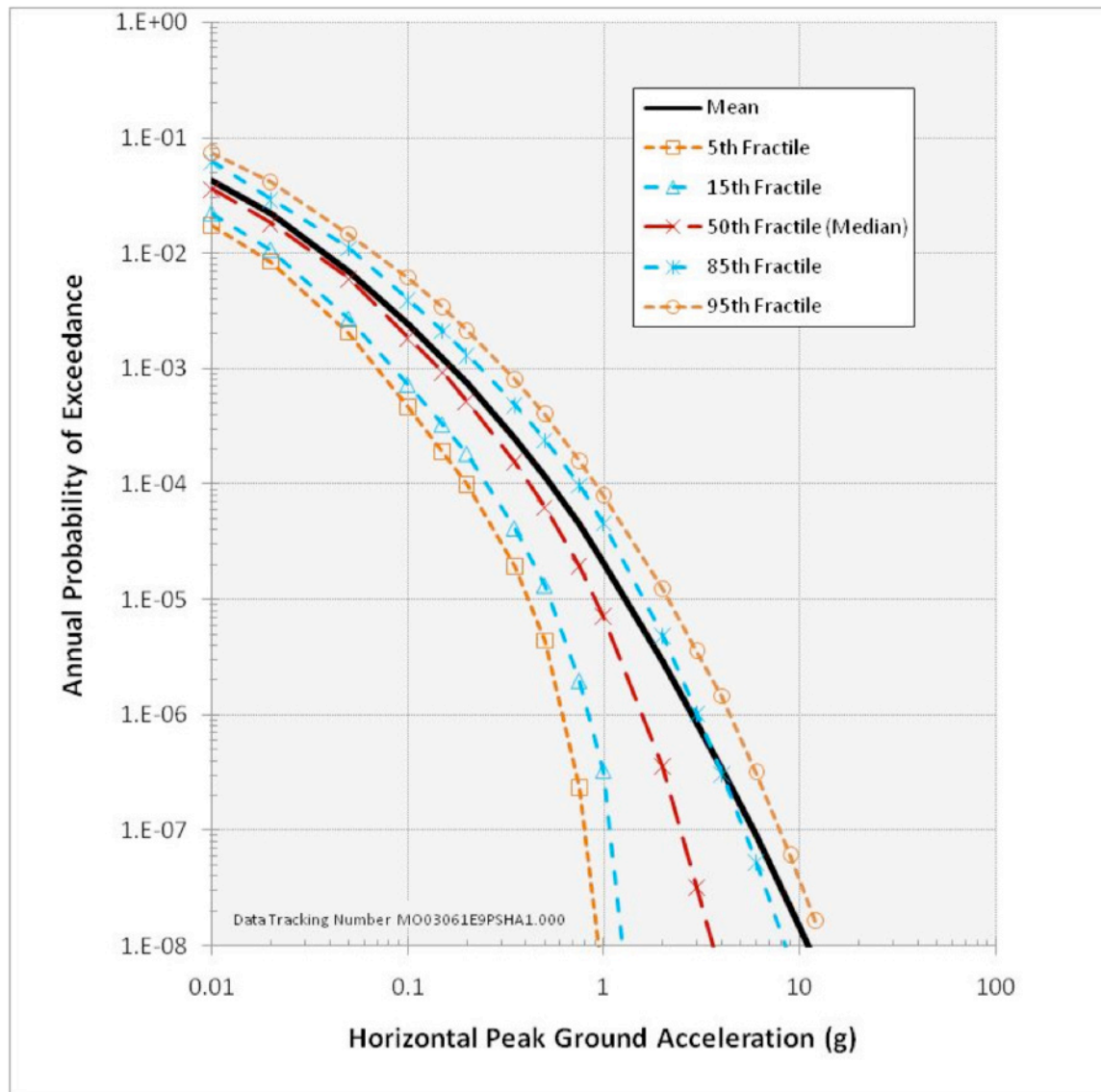
Figure 3. Plot showing probability-of-exceedance calculations for horizontal peak ground acceleration at Point A, a hypothetical, reference rock-outcrop site at the repository horizon (Stepp and others, 2001; from the 1998 Yucca Mountain Probabilistic Seismic Hazard Analysis, extended to 10-8 per year, BSC [2004]).
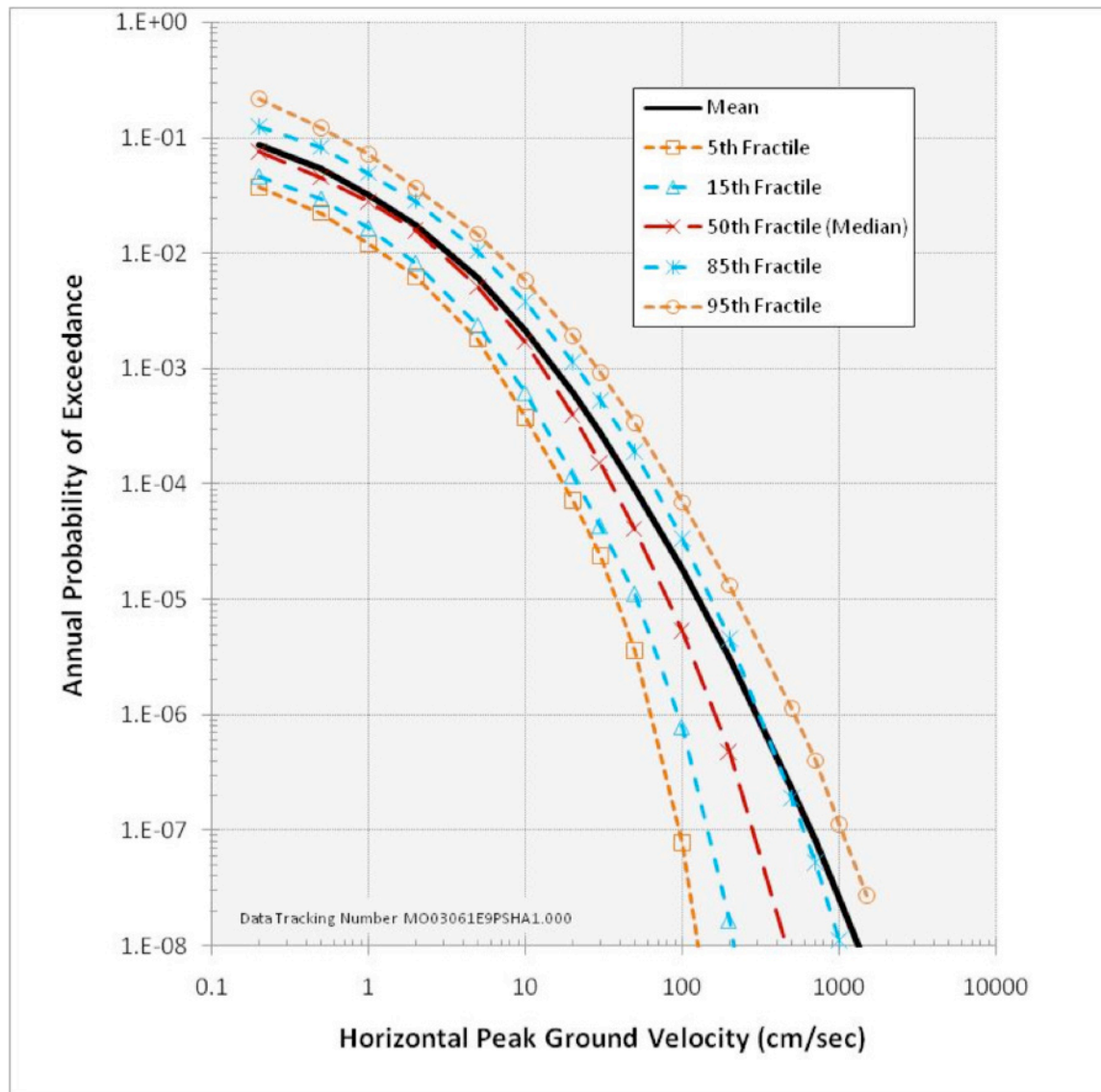
Figure 4. Plot showing probability-of-exceedance calculations for horizontal peak ground velocity at Point A, a hypothetical, reference rock-outcrop site at the repository horizon (Stepp and others, 2001; from the 1998 Yucca Mountain Probabilistic Seismic Hazard Analysis, extended to 10^{-8} per year, by BSC [2004]).

Approximately one-third of the ExGM budget has been placed at SCEC, to support its scientists working on the ExGM research program, as well as to support the highly successful SCEC/ExGM annual workshops. Held in 2006, 2007, and 2008 before the annual meeting, these workshops summarized the ExGM research results of the preceding year; each of these workshops was attended by more than 100 interested scientists, most of who were not supported by ExGM.

The primary purpose of this report is to summarize the principal results of the ExGM research program as they have developed over the past five years, beginning with the 2004 workshop; what follows below will be focused on Yucca Mountain, but not restricted to it. We begin, however, with a brief conceptual discussion of how the ExGM research program sits in the context of PSHA, especially for Yucca Mountain.

Table 1. Members of the Extreme Ground Motion Committee (ExGMCom), past and present.

Member	Affiliation	Participation period
N.A. Abrahamson	Pacific Gas & Electric Co	2003 to present
D.M. Boore	U.S. Geological Survey	2003 to present
J.N. Brune	University of Nevada, Reno	2003 to present
C.A. Cornell	Stanford University, deceased	2003 to 2007
T.C. Hanks, Chair	U.S. Geological Survey	2003 to present
M. Board	Itasca	2004 to present
J. Baker	Stanford University	2008 to present
W.U. Savage	U.S. Geological Survey, Liason to Department of Energy	2007 to present
J.W. Whitney	U.S. Geological Survey	2009 to present
Ex Officio		
R.J Budnitz	Lawrence-Berkeley National Laboratory	2003 to present
Doug Duncan	U.S. Geological Survey, Liason to S&T, Department of Energy	2005 to 2007
C. Fairhurst	Pofessor Emeritus, Univ. of Minnesota	2005 to present
J. Ake	U.S. Nuclear Regulatory Commission	2005 to 2007
L.S. Cluff	Pacific Gas & Electric Co., retired	2005 to present
J.R.Dyer	OCRWM, Department of Energy, retired	2007 to 2009

Extreme Ground Motions and PSHA

Most scientific analyses, including PSHA, are based on things that have happened: earthquakes that have occurred in this region or on that fault, for example, and have generated these ground motions. Extreme ground motions force us to deal with things that have not happened and, perhaps, cannot happen, presenting new and unusual challenges for earth scientists in general and PSHA practitioners in particular. We will develop some new definitions in this section to deal with extreme ground motions in the context of PSHA and also present some of the ideas we will put into play specifically for Yucca Mountain.

At first blush, estimating ground motion at Yucca Mountain at a hazard level of 10^{-8}/yr, roughly equivalent to the ground motion that occurs once every 100 million years, seems not only impossible but pointless: Yucca Mountain has only existed for 10 million years or so. Because the rate of earthquake occurrence is so low at Yucca Mountain, however, things are nowhere near as bad as they may seem.

The basic element of any PSHA calculation is that any one earthquake has a certain probability of occurring and that once it does occur, some ground-motion level has a certain probability of being exceeded, given the magnitude and distance of that earthquake. The probability of exceeding that ground motion for this single earthquake is the product of the earthquake probability and its ground-motion probability, generally expressed on a per annum basis. Customarily, PSHA involves summing the contributions of all such earthquakes at all magnitudes and at all distances, calculated for whatever range of ground motions or hazard levels is of interest to the analyst or client.

If, however, one is interested in large ground motions in a seismotectonic regime dominated by a single fault expressing the majority of slip rate throughout the regime, the PSHA integral collapses (mostly) to the single-fault contribution, determined by the rate at which large (or perhaps characteristic) earthquakes occur on this fault and the probability that the ground motion from that earthquake will exceed whatever ground-motion level one chooses. It is in these circumstances that PSHA comes closest to deterministic seismic hazard analysis (DSHA), although a probability of exceedance is still specified. For the underground repository at Yucca Mountain, the Solitario Canyon Fault and the Paintbrush Canyon-Stagecoach Road Fault are the principal players because of their high slip rates (relatively speaking), total throws, longer lengths, and proximity to the site. (These faults will be discussed in more detail in the following section, "Geologic and Tectonic Setting of Yucca Mountain.")

The general point of this discussion is that some ground-motion amplitude estimated for a hazard level of 10^{-6}/yr does not mean one-in-a-million ground motion. In the case of these faults, with a recurrence interval of ~50,000 to 100,000 years for magnitude (**M**)=6.5 to 7.0 earthquakes, for example, what we are really interested in is the 1 in 20 (or 10) PGA and PGV at close distances to estimate ground motions at hazard levels of 10^{-6}/yr. We will use this and other simplified source models in the following sections.

Within the context of PSHA, extremely large ground motions are tied to extremely low probabilities of exceedance. Something that has a very low probability of happening, however, is not something that will never happen, at least not within the strictures of conventional probability theory and in its PSHA applications. Nevertheless, most earthquake scientists can agree that there are physical limits to ground motion. Ground motions larger than these physical limits cannot occur, ever. Physical limits to earthquake ground motion, then, if they can be plausibly demonstrated and calculated, provide the simplest and surest way to assess extreme ground motions. They also provide a solid basis for truncating the upper tails of ground-motion distributions, heretofore a subjective and often contentious subject among PSHA practitioners.

Physical limits to earthquake ground motion do not exist in the realm of linear elasticity, where earthquake seismologists have worked so successfully for more than a century: they arise from nonlinear, dissipative deformation mechanisms that are fundamentally due to the finite strength of crustal rocks and their erosional detritus. Physical limits to ground motion might arise from the strength of rocks at or near the site of interest, in the source region at 10–15 kilometers (km) depth, or anywhere along the path in between. Quite generally, the strength of rocks increases with confining pressure, so we may expect that rock properties at or near the site will place more stringent limits on ground motions than will rock properties at midcrustal depths, where most earthquakes occur. Moreover, rocks at shallow depth are easily accessible, allowing for both direct observation of their structure and fabric as well as sampling for laboratory testing. Such analyses, however, are inevitably site specific, at least to some degree. More general physical limits on earthquake ground motion exist, we believe, in the form of limiting conditions on the source excitation of crustal earthquakes. These more general conditions, however, are more difficult to discern with confidence, given the inaccessibility of what goes on at midcrustal depths and the short record of instrumental recordings of earthquakes.

In contrast to ground motions that cannot occur because of physical limits are ground motions that have not yet occurred—but may occur at any time. Fragile geologic structures, such as precarious rocks, precipitous cliffs, natural bridges and arches, and delicate speleothems, speak to ground-motion amplitudes that have not occurred since the formation of these structures. We refer to these ground motions as *unexceeded ground motions*, where it is implicit that a certain period of time is involved. Unexceeded ground motions, then, are not ground motions that cannot occur; they are ground motions

that have not occurred in the lifetime of the fragile geologic structure of interest. Of the many and diverse types of fragile geologic structures, precariously balanced rocks (PBR) are the most ubiquitous. J.N. Brune and colleagues first recognized PBRs as evidence of unexceeded ground motions and their implications for PSHA in southern California (Brune and Whitney, 1992; Brune, 1996; Anderson and Brune, 1999).

Fragile geologic structures in seismically active regions that have been damaged, of course, do speak to the occurrence of earthquakes capable of generating the damaging ground motion. Kagan and others (2005) used fallen speleothems in caves located 40 km west of the Dead Sea Transform Fault to develop a 185-ka chronology of earthquakes in that part of the eastern Mediterranean landscape. Correlation with the ages of disturbed layers in cores of the Dead Sea sediments reveals that most of the speleothem damage was caused by major earthquakes on the Dead Sea Transform Fault. Much can be learned from fragile speleothems in the limestone caves of western Kentucky and Tennessee, for example, which might extend the earthquake record of the New Madrid Seismic Zone back to tens, perhaps hundreds of thousands of years.

In addition to considering physical limits to ground motion and unexceeded ground motions in addressing extreme ground motions, we are also interested in event frequencies, or the frequency of occurrence of things that control or parameterize earthquake ground motions. In the case of extreme ground motions of large amplitude, such parameters include the frequency of occurrence of very large earthquake stress drops, very large single-event faulting displacements, very large PGA and PGV values, (among other ground-motion metrics), and ground-motion outliers. Because of the way we have defined extreme ground motions, we anticipate that they will be associated with ground-motion amplitudes and (or) earthquake source parameters that occur only rarely.

In the end, of course, PSHA is just concerned with the frequency of things, specifically the rates at which earthquakes occur and the distribution functions of the ground motions they radiate, expressed finally as probabilities of exceeding various ranges and types of ground-motion amplitudes.

Geologic and Tectonic Setting of Yucca Mountain

Yucca Mountain lies within the Basin and Range Province, between the Colorado Plateau on the east and the Sierra Nevada on the west. It has been actively extending and opening in a predominantly east-west direction for 20 m.y. or so, and this extension continues to the present day. In the brittle upper crust, this extension is accommodated by brittle failure (earthquakes) on steeply dipping normal faults; the down-thrown block becomes a basin filled by the erosional detritus from the range formed by the up-thrown block. In the lower crust and upper mantle, extension occurs by viscous, aseismic flow. The resulting basins and ranges trend primarily north-south, with a wavelength of ~30 km between successive basins (or ranges). The "basins" and "ranges" and their controlling faults near Yucca Mountain, however, have spacings an order of magnitude smaller than is typical for the Basin and Range (figs. 5 and 6).

The rocks of Yucca Mountain are the solidified remnants of massive, silicic, ash-flow tuffs effused from the Timber Mountain Caldera (fig. 1) from ~14 Ma to ~11 Ma. Since then, these units have been offset ~300 m by down-to-the-west normal faulting along the Solitario Canyon Fault (SCF) and the Paintbrush Canyon-Stagecoach Road Fault (PSF)—the Yucca Mountain block-bounding faults— and by lesser amounts on other nearby faults. The SCF bounds the down-dropped, volcanically active Crater Flat block on the east. Crater Flat is bounded on the west by the east-dipping Bare Mountain Fault (fig. 6), a major range-bounding fault with a low Quaternary slip-rate (~0.01 mm/yr; Anderson and Klinger, 2004). About 65 percent of the extension in Crater Flat took place between 12.7 and 11.6

Ma. After 11.6 Ma, extension decreased dramatically through the late Miocene, and the late Quaternary extension rate is less than one percent of the initial rate (Fridrich and others, 1999).

Basaltic volcanism began in Crater Flat at 11.3 Ma, coincident with the end of the magmatism that built Yucca Mountain (Crowe and others, 1995), and a second episode occured again at 3.7 Ma, when a large lava flow and a group of scoria cones were emplaced in southeastern Crater Flat (fig. 5). Subsequent offset of the flow by the Windy Wash fault indicates that its low average displacement rate since the Pliocene has continued into the late Quaternary (Whitney and Berger, 2000). Several volcanic cones developed in Crater Flat at ~1 Ma (figs. 1 and 5) and the latest eruption (~77 ka) created the Lathrop Wells cone at the south margin of Crater Flat, depositing black ash in open fissures of several Yucca Mountain faults that ruptured and extended at the same time.

Ongoing extension of Crater Flat is also evidenced by displacements along the other normal faults, but the late Pleistocene slip rates across them are also small, as we detail below. Recent rates of volcanism, and deformation across Crater Flat and in the vicinity of Yucca Mountain, then, have diminished considerably in the Plio-Pleistocene. Modern, geodetically determined strain rates are also very low, ~ 20 nanostrain/yr (see Hammond and others, 2010, for a recent analysis and references therein). Likewise, modern, regional earthquake rates based on historic earthquake catalogues as well as instrumental rates of seismicity near the Yucca Mountain area are very low (Stepp and others, 2001).

The principal faults of the Yucca Mountain environs are block-bounding, normal faults spaced 1–5 km apart and dipping 50° to 80° to the west. From east to west, they are the Paintbrush Canyon, Bow Ridge, Solitario Canyon, Fatigue Wash, and Windy Wash Faults (figs. 7 and 8), and all show evidence of multiple, surface-rupturing earthquakes during the Quaternary (Simonds and others, 1995; Keefer and others, 2004). Displacements along these faults are mainly dip-slip, down to the west, with subordinate oblique slip displayed by some faults. Seismic reflection data suggest that the faults penetrate and offset the Tertiary-Paleozoic contact beneath Yucca Mountain (Brocher and others, 1998).
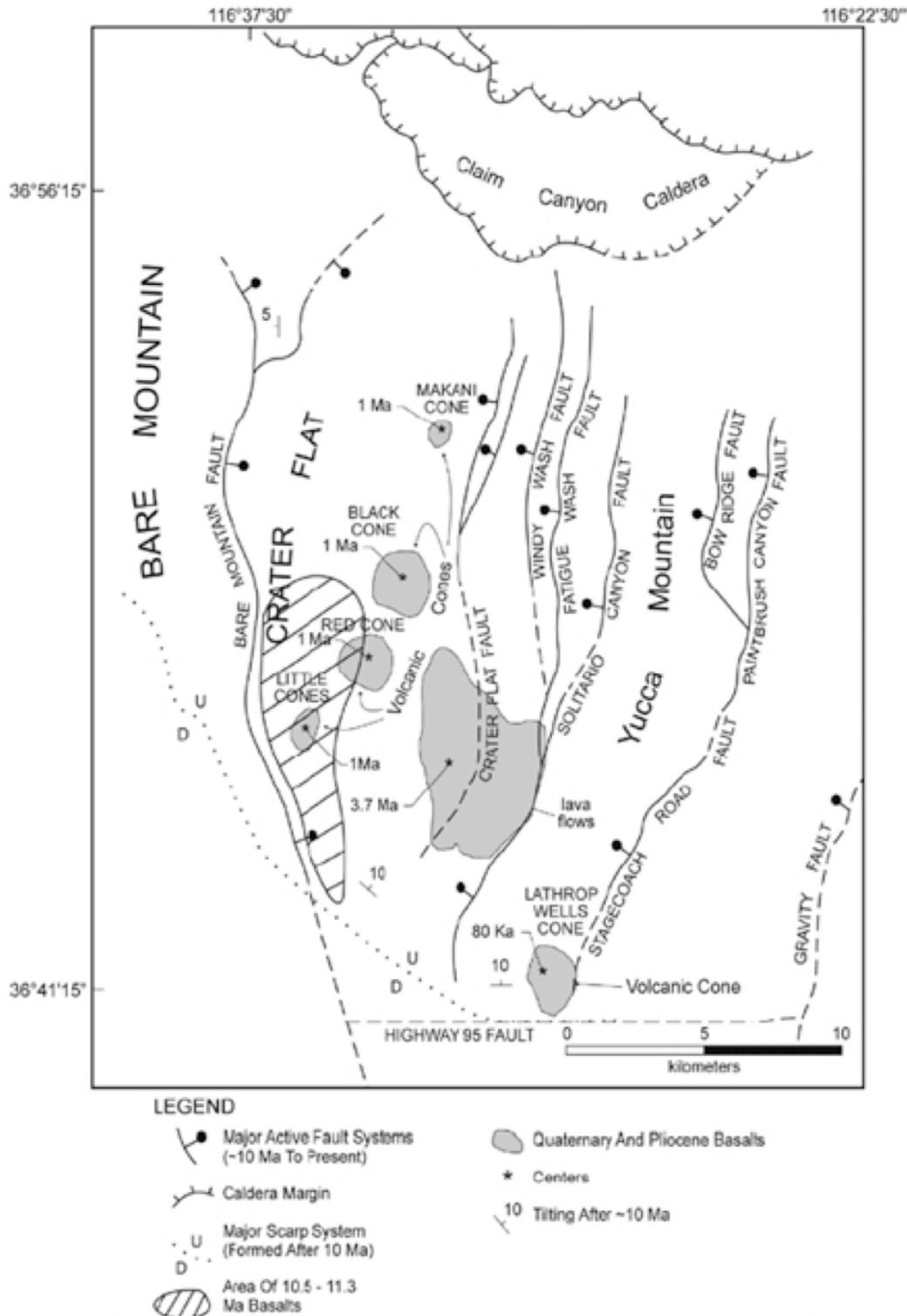
Figure 5. Simplified geologic map showing principal faults, blocks, and volcanic centers from Yucca Mountain to Bare Mountain, from Fridrich and others (1999).
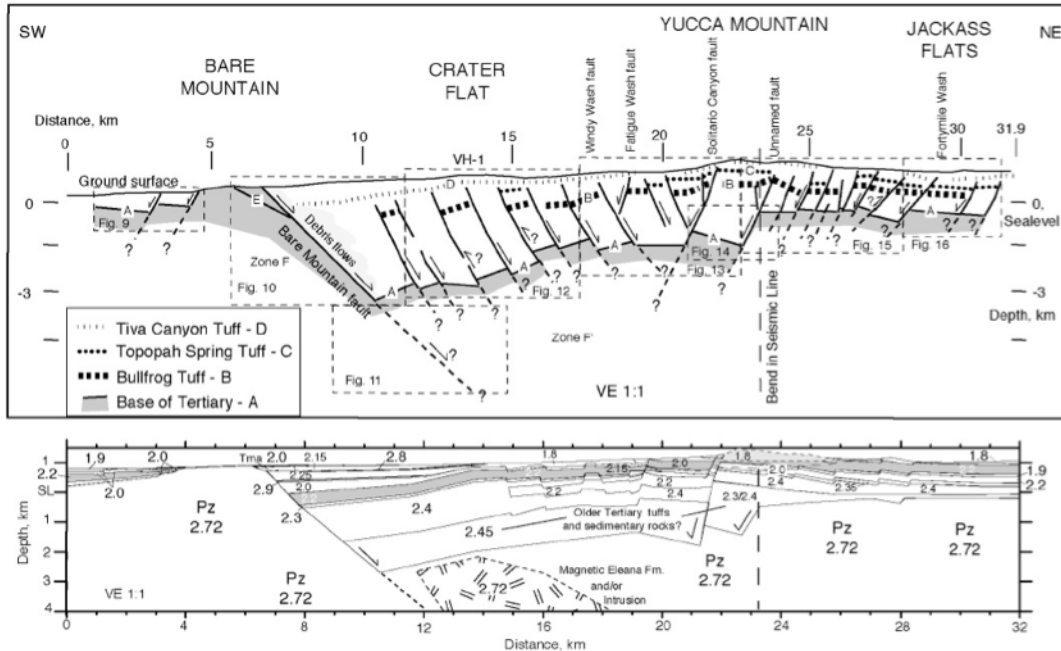
Figure 6. Cross section showing interpretation of seismic profiling across southern Crater Flat in terms of upper crustal (depth<4 km) blocks and faults (top) and stratigraphy and density (bottom). Pz=Paleozoic; VE=vertical exaggeration. From Brocher and others (1998).

The anastomosing pattern, relatively short lengths (4–25 km), and close spacing between the faults indicate probable structural interconnection between some faults, either along strike or at depth. Several interblock faults were also identified; however, no evidence for Quaternary displacement has been found on these bedrock faults (Taylor and others, 2004).

Paleoseismic studies of the block-bounding faults indicate slip rates of 0.001 to 0.05 mm/year (table 2) and average recurrence intervals of 10,000 to more than 100,000 years; these are very low slip rates for active faults in the Great Basin (Slemmons and DePolo, 1986). Average coseismic displacements range from 20 to 127 cm and maximum displacements on the Yucca Mountain faults range from 32 to 205 cm. Preferred surface rupture lengths, as assessed by the six seismic source teams assembled for the 1998 PSHA teams, range from 6 to 8 km on the shorter faults and 19 to 27 km on the Paintbrush Canyon, Solitario Canyon and Windy Wash faults (Stepp and others, 2001). Based largely on these characteristics, the largest earthquake magnitude estimated for the 1998 PSHA ranged from 6.6 to 7.0, with a recurrence interval of ~100,000 years (Stepp and others, 2001).
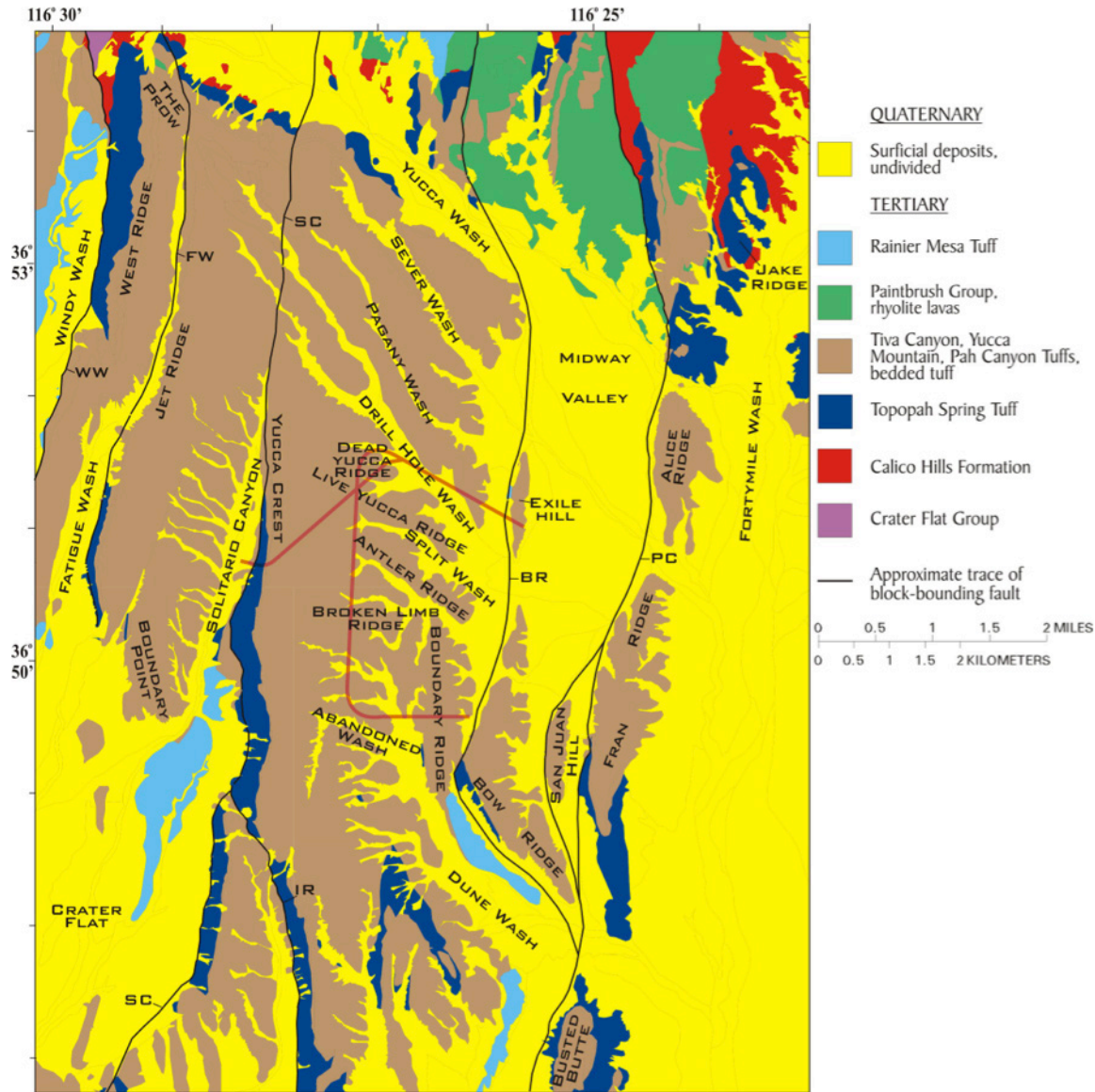
Figure 7. Geologic map of Yucca Mountain and vicinity showing principal geologic units, major faults, and various geographic features. Faults are shown with solid lines, although some segments are concealed or inferred beneath Quaternary deposits; BR, Bow Ridge Fault; FW, Fatigue Wash Fault; IR, Iron Ridge Fault; PC, Paintbrush Canyon Fault; SC, Solitario Canyon Fault; WW, Windy Wash Fault. The longer Exploratory Studies Facility (ESF) and Enhanced Characterization of the Repository Block (ECRB) tunnels are shown as red lines. From Keefer and others (2007), generalized from Day and others (1998).
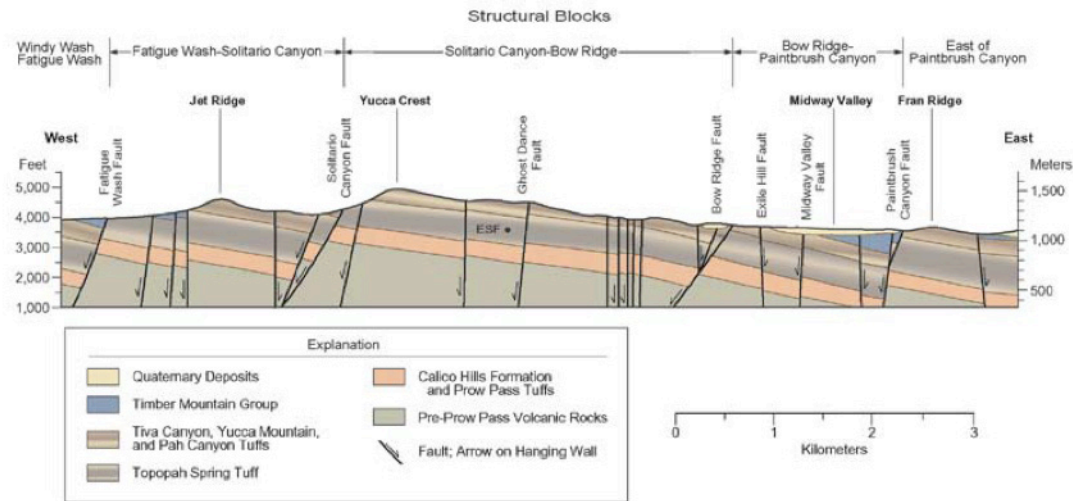
Figure 8. East-west cross section showing structure across Yucca Mountain at the latitude of the proposed repository. Datum is mean sea level. ESF, position of Exploratory Studies Facility tunnel at intersection with line of section. Simplified from Day and others (1998a, cross section B–B′).

The paleoseismic history for each of the faults in table 2 for the past 100 ka is summarized by Keefer and Menges (2004). In terms of both Quaternary slip rate (0.01 to 0.02 mm/yr) and total offset, Solitario Canyon Fault and the Paintbrush Canyon Fault, the block-bounding faults of Yucca Mountain, are the dominant members of this set of faults (Ramelli and others, 2004; Menges and others, 2004).

Table 2. Characteristics of significant local faults of the Yucca Mountain area (from Stepp and others, 2001).

[LL-N, left-lateral strike slip and normal]

Fault name	Rupture length (km)	Distance[1] (km)	Sense of slip	Fault dip	Slip rate[2] (mm/yr)	Probability of activity
Solitario Canyon	16–19	1	LL-N	60º	0.01–0.03	1.0
Iron Ridge	6–9	2.5	LL-N	60º	0.002–0.004	0.1–1.0
Bow Ridge	6–8	2.5	LL-N	60º	0.002–0.003	0.4–1.0
Fatigue Wash	9–17	3.5	LL-N	60º	0.002–0.009	0.9–1.0
Paintbrush Canyon	12–19	4	LL-N	60º	0.002–0.017	1.0
Windy Wash	5–27	4.5	LL-N	60º	0.003–0.03	0.6–1.0
North Crater Flat	6–13	6	LL-N	60º	0.001–0.003	0.5–1.0
South Crater Flat	6–8	8	LL-N	60º	0.001–0.008	0.5–1.0
Stagecoach Road	4–10	10	LL-N	60º	0.016–0.05	1.0

Despite the abundant evidence for the geologic and tectonic setting of the Yucca Mountain being fundamentally governed by the crustal extension of the Basin and Range Province in which it lies, there are a number of features of this place that are atypical of Basin and Range characteristics, including normal faults that are quite short by Basin and Range standards, just 10 to 20 km in length, and also are closely spaced, just 1 to 5 km apart.

While the Yucca Mountain domain experienced significant volcanic activity and tectonic deformation in the late Miocene, these rates diminished dramatically in more recent times, as we have noted previously. Deformation rates and fault-slip rates here are low by an order of magnitude or more compared to active normal faults in the Basin and Range. Where the faults are exposed at the surface near their northern ends, they are all west-dipping; in contrast, as is evident from the cross section (fig. 6) and based on seismic profiles across southern Crater Flat, many of these faults are apparently *east* dipping. Few of them, however, are exposed at the surface, given the heavy influx of Quaternary alluvium in the southern and western parts of Crater Flat. Templeton and others (2009) have used numerical simulations to find that faulting displacements on the west-dipping Solitario Canyon Fault will tend to lock up the east-dipping faults to the west shown by Brocher and others (1998), contrary to what occurred on the Fatigue Wash and Windy Wash faults during the 77-ka earthquake.

These oblique faults, with left lateral and extensional displacement, seem to form a radial splay to the south, from a locus near the Timber Mountain Caldera. Quaternary slip rates on these faults also increase to the south, over very short distances by Basin and Range standards. All of these fault features suggest that the extensional opening and down dropping of the Crater Flat block is a complicated and fairly localized process, perhaps more a function of the shear wrenching induced by Walker Lane tectonics than conventional Basin and Range extension (O'Leary, 2007). Hammond and others (2010) note the similarity between southern Walker Lane and Yucca Mountain tectonics as expressed in modern Global Positioning System (GPS) data.

Within the context of extreme ground motions, the possibility of very large earthquakes and resulting ground motions on subhorizontal detachment faults at depth beneath Yucca Mountain naturally arises. Detachment faults and related processes of core complexes were widespread in mid-to-late Miocene time through the extensional domain of what is now the southwestern U.S., yet considerable uncertainty remains as to how they actually work mechanically (Axen, 2004). Although seismological evidence for subhorizontal faulting has been reported for a localized region of the Woodlark Basin in the southwest Pacific Ocean, there is little direct evidence that low-angle detachment faulting in present-day continental crust is seismogenic, leaving us uncertain as to whether such structures can even generate earthquakes, and if so, what their ground motions are likely to be.

Despite the existence of detachment faults in the vicinity of Yucca Mountain, there is no evidence to demonstrate that they are active at the present time, here or anywhere else in the Basin and Range. O'Leary (2007) considered at length the evidence for and against detachment faults as a tectonic model for Yucca Mountain. None of the four tectonic models reviewed by O'Leary (2007), of which detachment faults were one, was considered to be an adequate explanation of the observations and deformation history.

Distributed surface ruptures have occurred simultaneously on multiple faults that are spatially close to one another (only a kilometer or so at the surface) and possibly coalesce at depth. The Windy Wash and Fatigue Wash Faults ruptured in concert with the Solitario Canyon Fault at the time of the last eruption of Lathrop Wells at 77 ka; volcanic ash from that eruption was deposited in the open fissures of all three faults, and also in surficial cracks along the Bow Ridge Fault (Ramelli and others, 2004; Keefer and Menges, 2004). This unusual volcano/seismo/tectono event was associated with maximum fault displacements of 1.0 m on the Windy Wash Fault, 0.4 m on the Fatigue Wash Fault, and 1.3 m on the Solitario Canyon Fault, making it the largest known faulting event in the paleoseismic record in the Yucca Mountain region.

This 77-ka earthquake is perhaps the one most likely to reflect detachment faulting, if the three faults that broke become one at (presumably shallow) depth and then "listric" into a sub-horizontal detachment fault. Whether this is the case or there is a single, steeply-dipping plane that is the root for

all three faults (the model favored by the geologists assembled for the 1998 PSHA), there is nothing special about the ground motion generated by this faulting event, as we shall see in later sections. Two or more faults may also have been active simultaneously around 3, 13, 20–30, and 50 ka (Keefer and Menges, 2004), but these possibilities exist with less certainty.

In addition to its low rates of recent volcanic, tectonic, and seismic deformation, Yucca Mountain area has experienced a low rate of erosion during the past ~1 million years, the subject of the next section. Whitney and Harrington (1993) first noticed that a long Quaternary record is preserved in the Yucca Mountain region, reflecting low rates of erosion and tectonic deformation. Whitney and others (2004) recount the evidence for the abundance and preservation of mid-to-late Quaternary deposits, the multiple climate cycles they record, and the pedogenic carbonate horizons that have developed, all of which point to low rates of erosion and deformation in the Yucca Mountain area, which in turn make for the exceptionally long and well-documented paleoseismic record. Fifty trenches and natural exposures evince numerous fault-slip events on the eight principal faults local to Yucca Mountain in the last 100,000 years (Keefer and Menges, 2004), for which the fault-slip event history seems reasonably complete. Fault-slip events significantly older than 100 ka have also occurred on these Yucca Mountain faults. Trenches on several of them exposed U-series-dated carbonate horizons as old as 250 ka, and the Bishop Ash (760 ka) is present at the base of a sand ramp offset by the Paintbrush Canyon Fault.

Equally important for ExGM, these low rates of deformation and erosion make for the "million-year-old landscape," with important consequences for the evolution of Yucca Mountain in the late Quaternary, especially the formation of precariously balanced rocks (PBR) on its the west face.

The "Million-Year-Old Landscape"

There are two important erosional processes at work on the crest and west face of Yucca Mountain. The first is the "block-by-block" retreat of the cliff-forming ledges of the densely welded Tiva Canyon Tuff (fig.9A), which forms the crest of Yucca Mountain, and the midslope, Topopah Springs Tuff, in which the repository is planned. Boulders of ~1–2 m dimension, determined by the spacing of cooling joints, fall out of these cliffs and roll or slide down the west face of Yucca Mountain. This process governs the formation rate of PBRs within the cliff-forming units. We estimate this lateral retreat rate with the geometry of figure 9B, which shows ~130 m of retreat from a 60° west-dipping fault plane extrapolated to the elevation of the Yucca Mountain crest over 12.7 m.y., yielding a lateral retreat rate of ~1m per 100,000 years. This block-by-block retreat of the west face of Yucca Mountain is driven by retreat of the more erodible slopes beneath the cliff-forming ledges, undercutting these ledges.
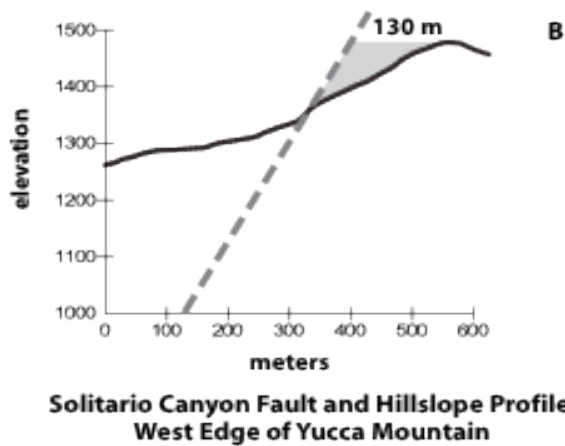
Figure 9. *A*, Photo of the Tiva Canyon Formation forming the Yucca Mountain crest, looking north. Cooling fractures spaced at 1–2 m spawn boulders of this size that roll down the slope to the left, dots in left center. Surface lowering of the crest is much slower, 1–2 m/m.y. *B*, Plot showing lateral retreat of the west face of Yucca Mountain, solid line, with respect to the Solitario Canyon Fault, where dashed line is extrapolated to the elevation of the present-day crest as a 60°west-dipping normal fault. The lateral retreat at the crest has been ~130 m over 12.7 m.y., averaging 10 m/m.y.

The second process is "grain-by-grain" weathering that is responsible for the lowering of the Yucca Mountain crest and determining the residence times of the boulders on the slopes below the cliffs (fig. 10). It is also responsible for some weathering of boulders still perched on the cliffs, especially in the cooling fractures of the Tiva Canyon Tuff (fig. 9*A*). A very low bedrock erosion rate of 1.38 m/m.y. on the surface of Yucca Mountain was determined from a whole-rock [10]Be method (Gosse and others, 1996). That rate has recently been substantiated by analyses that we will discuss in more detail later: an erosion rate of 1.7 m/m.y. measured by [36]Cl analysis of feldspar minerals extracted from the Tiva

Canyon Tuff and a rate of 1.4 m/m.y. obtained by a ^{10}Ne cosmogenic analysis, both from samples taken on the Yucca Mountain crest.

The Tiva Canyon Tuff is more erodible than the Middle Ledge of the Topopah Springs Tuff, apparently because of the greater abundance of *lithophysae*, cavities formed by exsolving gases as the volcanic tuffs cool. Lithophysae are also known as *fiamme*, but fiamme can also develop through flattening of pumice clasts and their subsequent erosion due to material heterogeneity in the tuffs. We use lithophysae here, perhaps not always correctly, because it is used throughout the Yucca Mountain literature.

(As a result of the ExGM research program, many new surface-exposure ages, of the sort mentioned briefly in the paragraph above, are available to determine erosion rates and boulder residence times, both on Yucca Mountain and other nearby sites. These results, put to use in several different places in the remainder of this report, are derived from the cosmogenic abundances of ^{10}Be and ^{36}Cl. All of these new results are presented in appendix I, together with the sample-preparation essentials.)

Comparisons of the structural relief to the topographic relief along two profiles across Yucca Mountain, separated by ~1 km along the strike of the crest, suggest between 16 and 21 m of erosion of the crest of Yucca Mountain in the 12.7 m.y. since the Tiva Canyon Tuff was laid down. This yields average vertical lowering erosion rates of ~1–2 m/m.y. for the past 12.7 m.y. If the alluvial fill in Midway valley is mostly derived, with no loss of fill, from the grain-by grain erosion of the Yucca Mountain bedrock to the west, the ~30 m of alluvium in Midway Valley also suggests a bedrock lowering rate of ~2 m/m.y.

Other things being equal, then, the west face of Yucca Mountain changes very slowly. In simple, average terms, a 1-m cubic block of rock is released from the cliff-forming units every 100,000 years for every meter along strike and for every meter of cliff-forming thickness. Along the northern reach of Yucca Mountain, where the Middle Ledge of the Topopah Spring Tuff has dipped beneath the surface, the lone cliff-forming unit, the Tiva Canyon Tuff that forms the crest, is ~10 m thick. Thus, ten 1-m cubic blocks per meter along strike should exist for every 100,000 years that they endure on the slopes in view. We will explore this possibility shortly, with an interest in what the 77-ka earthquake might have done such that "other things" were not equal. But first we will address the rate of the block-by-block cliff retreat hypothesis and then determine the residence time of boulders fallen from above onto the slopes below.

To test the block-by block retreat model, exposure ages were determined along two cliff profiles just beneath the Yucca Mountain crest. The southern profile ran from the lower part of the Tiva Canyon Tuff to the top of the crest and out onto the flat behind it. With the exception of the sample from the top of the crest, which was dated to 286 ka (and which reflects the secular, grain-by-grain erosion rate of ~ 2 m/m.y.), all of these ages are between 110 and 160 ka, in approximate agreement with new faces being exposed every 100,000 years or so. The northern cliff profile near PBR Nichole (discussed in the section called "Precariously Balanced Rocks (PBRs)") shows that cliff retreat along the Yucca Mountain crest is not spatially uniform and that sections of the cliff have not been eroded for over 250 ka. Or perhaps we should keep an eye out for 2-m blocks that are released every ~200,000 years; they are not hard to find on the surfaces below (fig. 10).

Determining the residence time of boulders on these slopes is not simply a matter of sampling the unshielded boulder top. The problem here is that, while still in place on the cliffs, some of these rock faces were exposed to incoming cosmic rays (which we regard as inheritance with respect to the actual residence time on the slopes below) and others were not. Our sampling strategy, then, was to sample the youngest faces on these boulders, the ones most likely to have been shielded while on the cliff. This was done on the basis of several geomorphic considerations, including orientation of the lithophysae

(approximately horizontal when in place on the cliffs), relative weathering and pitting expressed by the different faces, and rounding of originally angular corners. There is no guarantee, however, that we were always successful in these determinations. Even so, we have found that our relative assessments of antiquity based on field observations agree well, if not completely, with the ordered exposure ages.

Figure 10. Photo of an older boulder on the pediments at the base of the west face of Yucca Mountain, with an exposure age of 218 ka. The pothole on top is 1m deep. Dylan Rood for scale.

We do not have a large set of exposure ages on the Yucca Mountain pediments (appendix I, table 2, bottom group) but we do have ages on the nearby Cholla, Castle Rock, and Highway 95 (SH95) surfaces (appendix I, table 1). These surfaces are littered with boulders of the Ammonia Tanks Tuff, itself a high-standing cliff-former, and these boulders, too, can endure for hundreds of thousands of years on the pediments below. The Ammonia Tanks Tuff contains free quartz, and our exposure ages for these boulders were based on the abundances of ^{10}Be. Prior to the development of the ^{36}Cl methodology for alkali feldspar mineral separates by R.C. Finkel and D.H. Rood in 2008, which allowed us to analyze Yucca Mountain samples, our only control on dates and rates of geomorphic processes in the vicinity of Yucca Mountain was from the Cholla, Castle Rock, and SH95 sites. Appendix I, table 3 shows comparisons of exposure ages using abundances of ^{10}Be and ^{36}Cl.

The results from Cholla, Castle Rock, and SH95 are comparable to what we obtained at Yucca Mountain: the boulders released from the cliffs above can endure on the slopes below for hundreds of thousands of years, at least. Indeed, one Castle Rock boulder that we sampled has a minimum exposure

age, assuming no erosion, of 523 ka. This boulder, however expresses abundant evidence of spheroidal rounding, incipient degradation, and mass loss; it may have resided here for more than a million years.

Finally, a remarkable consequence of the low deformation and erosion rates affecting the Yucca Mountain landscape is that it has not changed much in the last million years: the crest has been uplifted vertically by 10 to 20 m, it has been eroded down by 1 to 2 m, and has retreated laterally by ~10 m. A 10 m-resolution digital elevation model (DEM) of Yucca Mountain made a million years ago would not be much different from one made today, allowing us to "see" much further into the past than is ordinarily possible.

The Many Dimensions of Extreme Ground Motions

Assessing seismic hazard at probabilities of exceedance for 10^{-6} to 10^{-8}/yr requires thinking about PSHA in ways very different than those with which we are familiar. From the very beginning, ExGMCom was convinced that there would be no silver bullet with which to slay this dragon, only a preponderance of evidence that pointed in similar directions. Within the basic framework of physical limits to ground motion, unexceeded ground motions, and the frequency of occurrence of various things, the ExGM research program has followed a dozen distinct lines, as well as subsidiary paths related to them. These research activities have involved several dozen scientists working at a number of different institutions. The principal theme to be drawn collectively from all of this work is that the 1998 PSHA, when extended to hazard levels of 10^{-6} to 10^{-8}/yr, significantly overstates the true seismic hazard for Yucca Mountain (Abrahamson and Hanks, 2008); indeed, we now find this to be true at hazard levels of 10^{-5} and 10^{-4}/yr.

Several of these lines of research have had a disproportionate impact on our thinking about extreme ground motions, and we will begin with brief discussions of them. These include physical limits to ground motion determined by stress-conditioned failure of crustal rocks, an investigation led by D.J. Andrews; qualitative and quantitative comparisons of the very different landscapes of the Nevada Test Site (NTS) and the fault-controlled, steep west face of Yucca Mountain; the absence of observable effects of the 77-ka earthquake, the largest event known in the paleoseismic record, on the west face of Yucca Mountain; and points in hazard space, a graphical presentation of most of the significant ExGM research findings on a single plot.

The presentation by D.J. Andrews at the 2004 workshop on physical limits to ground motion at Yucca Mountain (Andrews, 2006; Andrews and others, 2007) spoke most directly to limiting conditions on crustal earthquake stress drops and the ground motions that result from them, for both elastic and inelastic rheologies. Even before the ExGM research program began, Andrews had demonstrated that physical limits to earthquake ground motion in rock exist in the form of limits to the strength of geologic materials. Nonelastic stress-wave calculations are required to determine these physical limits to ground motion, however, and the absolute state of stress must be known to initialize these calculations.

Andrews' workshop presentation pointed to several other important matters as well. The surface faulting displacement for the "Andrews earthquake" (defined in Andrews and others, 2007, and described in more detail in the section "Physical Limits to Earthquake Ground Motion") is 15 m, and such a fault scarp would endure in the Yucca Mountain environment for millions of years. This result motivated a study of the largest known surface faulting displacements for continental, normal-fault earthquakes (Hecker and others, 2010) to determine the frequency of occurrence of earthquakes with large faulting displacements. Likewise, a study of stress-drop distributions for crustal earthquakes determined from the very large, global m_b-M data set was undertaken by Dewey and Boore (2008).

J.N. Brune's research on precariously balanced rocks near Pahute Mesa on the Nevada Test Site (NTS)(Brune and others, 2003), the setting for hundreds of underground nuclear explosions (UNE)

during the latter part of the 20th century, focused ExGMCom's attention on the ground motions generated by UNEs. At close distances, UNEs generate PGAs and PGVs comparable to those for the Yucca Mountain PSHA at hazard levels of 10^{-7} to 10^{-8}/yr, namely 5 to 10 g and 5 to 10 m/s, respectively. The close-in, radiated field of UNEs, mostly composed of impulsive P-waves, is very different from earthquakes, of course, but these very large ground motions are just what concerns the ExGM research program. Such ground motions leave a dramatic signature on nearby landscapes.

Figure 11is a Google Earth image of Pahute Mesa, showing the crater of the UNE site Boxcar on the left, the nation's first underground megaton device detonated on April 26, 1968. The diameter of the crater in the intensely damaged region (white, exposing pedogenic carbonate) is ~300 m, but the faint, outermost ring fractures encompass a diameter of >400 m. It is ~50 m deep at the center of the crater. About 1.5 km east of the center of the Boxcar Crater is a small mesa of densely welded tuffs (~9 Ma) of the Thirsty Canyon Group, a place we call Boxcar Bluff (lower right of fig. 11). Segments of extensional opening cracks, exposing pedogenic carbonate, are faintly observable in white on the surface of Boxcar Bluff, and huge boulders, ~5 m in diameter, have broken off of the cliffs.

Figure 12 is a photograph taken on the southwest side of Boxcar Bluff, at the tail of the arrow in figure 11, looking up at Boxcar Bluff. Scientists in the middle left provide scale; the large white boulder to their left is encircled in figure 11. Boxcar Bluff has been intensely shattered by Boxcar and other nearby UNEs. White faces on the boulders are again due to pedogenic carbonate accumulation in the cooling fractures of the volcanic tuffs, which determine boulder dimensions.

Figure 11. Google Earth image of the crater of underground nuclear explosion sites Boxcar (left) and Boxcar Bluff (right). The white arrow denotes the camera direction for figure 12, and the white circle encloses the large white boulder on the left side of figure 12.

Before-and-after aerial photographs (not shown here) confirm that most but not all these boulders were thrown down as a result of the ground motion from the Boxcar detonation; most of the remaining boulders were thrown down by other nearby UNEs. Only a few boulders on the slopes demonstrate antiquity in their present locations. There is not much variability in the size distribution of particles on this talus slope, because boulder dimensions are primarily determined by the preexisting cooling joints, with spacing of ~5 m. While many boulders break as they roll down the slope, there is only minor shattering or crushing of these welded tuffs by the UNE ground motions.

Figure 13 shows a photo of the fault-controlled, northern reach of the steep west face of Yucca Mountain, the ~10 Ma scarp of the Solitario Canyon Fault (SCF) buried beneath the alluvium in the foreground. Have ground motions comparable to what UNEs have produced on Pahute Mesa occurred at Yucca Mountain? We think not, at least not in the residence times of the sparsely distributed boulders on and near the base of this steep surface. These boulders are derived from the Tiva Canyon Tuff that forms the crest of Yucca Mountain. This unit, about 10 m thick at this location, is weathering in place as well as shedding boulders that roll down the steep west face. Exposure-age analysis of these boulders, discussed earlier, reveals that they can endure for hundreds of thousands of years in this environment.

Figure 12. Photo looking up at Boxcar Bluff from the southwest. Note scientists for scale in middle left and to the right of the large white boulder.

Figure 13. Photo of the northern reach of the west face of Yucca Mountain. Sparsely distributed boulders are derived from the Tiva Canyon Formation, which forms the Yucca Mountain crest. The proposed repository lies behind this face, at a depth of ~100 m below the elevation of the foreground.

The paleoseismic record of faults local to Yucca Mountain is believed to be complete for fault-slip events, amounting to >10–15 cm since 100 ka (Keefer and Menges, 2004). Assuming that the individual slips on the Solitario Canyon, Fatigue Wash, and Windy Wash Faults are additive at depth on a single master fault, the 77-ka earthquake would be the largest slip event in the past 100 k.y. and perhaps as far back as Bishop Ash time (760 ka). The combined normal fault surface displacement on these three faults is 2.7 m for the 77-ka earthquake event, with an estimated moment magnitude of 6.7. Since 150 ka there have been two slip events on the Paintbrush Canyon-Stagecoach Road Fault; fault slip is less than 1 m for these events, and probably less than 50 cm. None of these events seems to have had much effect on the slope morphology shown in figure 13, given the long residence times of boulders on the west face of Yucca Mountain and other surfaces of this region.

With J.W. Whitney, Susan Buckingham has made detailed counts of the boulders and boulder volumes beneath the northern Yucca Mountain crest and "Rickey Ridge," a long, linear ridge shattered by the underground nuclear explosion Rickey on Pahute Mesa, ~50 km north of Yucca Mountain. The details of her results and calculations for the west face of Yucca Mountain are shown in appendix II. There are two important conclusions of this work. First, the Rickey explosion caused 2 to 4 m of retreat of Rickey Ridge (appendix II, fig. 2) at the time of this explosion, equivalent to 200 to 400 k.y. of cliff retreat on Yucca Mountain. Second, there is a boulder deficit on the pediments with respect to our hypothetical, block-by-block retreat rate of 1m/100 k.y.

Buckingham and Whitney can only account for 47 percent of the estimated boulder volume (and detritus derived from them) that should be on these pediments in 100,000 years and just half that in 200,000 years (if these boulders can endure for 200,000 years which we believe to be the case). While some of these boulders may be buried in the alluvium that underlies these surfaces, this alluvium is generally thin

(≤2–3 m) and unlikely to hide much in the way of boulders but more in the way of the surficial fragments counted as "ground cover" in appendix II. Significant fragmentation of boulders can occur as they bounce down the ~200 m of topographic relief (appendix II, fig. 3), and there is also a noticeable component of grain-by-grain weathering of the Tiva Canyon Tuff on the Yucca Mountain crest (appendix II, fig. 4), with an unknown amount of fine material removed from these slopes and transported down Solitario Canyon wash. Even so, it is remarkable that these estimates agree as closely as they do, given the very average nature of the block-by-block erosion rate, both spatially and temporally, and uncertainties in the boulder-mass calculations.

The important matter here is that there is no surplus of boulders on these slopes, as should be expected if extreme ground motions had occurred in the view of figure 12 in the past several hundred thousand years. Indeed, there is a decided deficit, even for 200,000 years. Neither is there any discernible effect of the 77-ka earthquake. While we do not associate extreme ground motions with this earthquake, it is still the largest known event in the ~800-k.y. paleoseismic record. As we shall see later, only two of the PBRs constrain the 77 ka earthquake ground motion, but both of them are quite fragile. The absence of discernible geomorphic effects of this earthquake suggests weak ground motion for it, a recurring but unresolved theme for extensional-regime, ground-motion excitation compared to compressional-regime excitation, a theme we shall revisit later.

Finally, in order to deal with the many different threads of extreme ground motions, we have developed a graphical view of PSHA inclusive of a far wider range of pertinent data and observations than a conventional PSHA hazard curve or map, a format we refer to as points in hazard space. It arose from presentations at the 2006 ExGM/SCEC workshop, after which ExGMCom convened a meeting on February 27, 2007, to discuss then-available observations amenable to this graphical framework. Figure 14 is the most recent incarnation of this approach, showing the physical limits to earthquake ground motion at Point B developed in Andrews and others (2007), unexceeded ground motions represented by the lithophysal units and PBRs on the west face of Yucca Mountain, and two simplified hazard models for Yucca Mountain. Hazard space is defined by the probability of exceedance, or hazard level, on the ordinate and some ground motion amplitude (PGV, in our case) on the abscissa. As in figure 4, calculated for Point A, the blue and black curves in figure 14 are the PGV mean seismic hazard curves and its fractiles, respectively, for Yucca Mountain, calculated here for the repository horizon (Point B).

Points A, B, and C are defined and located with respect to an east-west crosssection of Yucca Mountain through the repository horizon, located ~300 m beneath the Yucca Mountain crest (as in Stepp 2001, fig. 2). Point A is a reference rock outcrop at the repository elevation. Point B is a site at the repository horizon, with 300 m of volcanic tuff above it. Point C is a site atop Yucca Mountain. The 1998 Yucca Mountain PSHA was calculated for Point A, at a time when insufficient material-property data were available for calculations at Point B. We reference the ExGM calculations in this study to Point B, where the radioactive-waste canisters will reside.

In general, points and curves that fall well below the mean hazard curve (blue) for Yucca Mountain are inconsistent with it, indicating that the mean hazard curve is too high. Data close to or well above this curve do not indicate that the mean hazard curve is too low; they simply do not provide real constraints on it. Physical limits to earthquake ground motions are ground motions that cannot be exceeded at any hazard level and thus are vertical lines, solid red for the Andrews earthquake in an elastic medium and solid green for the Andrews earthquake in a plastic medium.

Figure 14 will appear again as the last figure of the main text of this report (fig. 46), where we develop in detail the calculations by which these results are plotted. We show it here to anticipate the various theoretical and observational constraints that can be applied to quantitatively test the veracity of the 1998 Yucca Mountain PSHA. Readers who have followed the development of the ExGM program

from its early days will know that even the earliest, preliminary versions of figure 14 all pointed to the conclusion that the 1998 Yucca Mountain mean seismic hazard curve significantly overstated the seismic hazard at Yucca Mountain (Abrahamson and Hanks, 2008). At the end of this report, we shall place that conclusion on a more rigorous foundation.
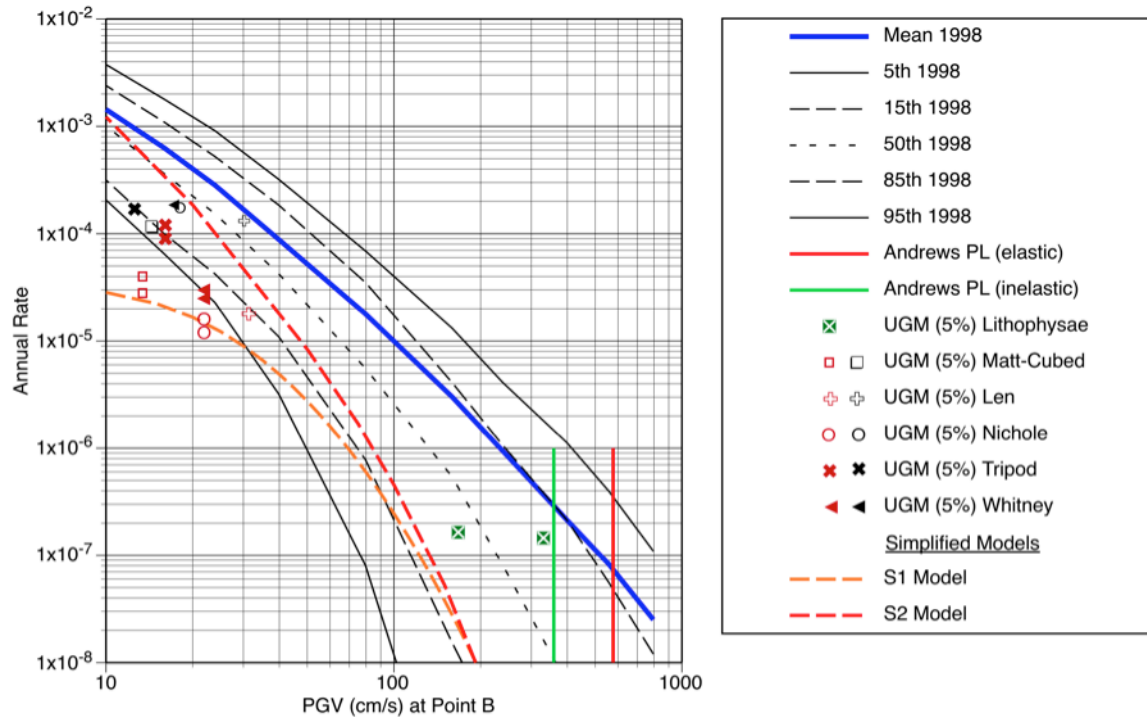
Figure 14.   A points-in-hazard-space graphic, showing physical limits to ground motion (vertical lines), the undamaged lithophysal limits (green symbols), precarious rocks (red and black symbols) for several choices of the age for which the rocks have existed in a precarious state, and two simplified hazard models using the more recent Next Generation Attenuation (NGA) ground-motion relations.

Physical Limits to Earthquake Ground Motion

At the August 2004 workshop, D.J. Andrews pressed the problem of physical limits to earthquake ground motion at Yucca Mountain to its intellectual limits by assuming a nearly complete stress-drop earthquake on the Solitario Canyon Fault. On the basis of the data of Stock and others (1985), and Zoback and Healy (1984), the Solitario Canyon Fault is thought to be just marginally stable to normal faulting on a plane dipping 60° to the west. Andrews' workshop presentation, which may be found as an appendix to Hanks and others (2006), is amplified considerably in Andrews and others (2007).

The maximum-slip, maximum-stress-drop model, hereafter the Andrews earthquake (figure 15), is a two-dimensional, super-shear, dynamic rupture calculation, nucleated at 10 km depth, with shear stresses dropping from those consistent with a static coefficient of friction of 0.7 to a dynamic coefficient of friction of 0.1. It results in 15 m of surface-faulting displacements, far larger than any faulting displacements known in the paleoseismic history for the Yucca Mountain faults and more than twice as large as any faulting displacement known for any historic or late Quaternary normal-fault

earthquake on Earth (Hecker and others, 2010). The shear stress released dynamically in the course of the Andrews earthquake averages to about 20 MPa over the full fault depth; the static stress drop estimated from the quotient of 15 m of displacement divided by 12 km of down-dip fault length is almost 40 MPa, again a very large number.

Ground velocities calculated at the repository level for elastic wave propagation resulted in a vertical PGV of 5.78 m/s and a horizontal PGV of 4.33 m/s. Given the large faulting displacement of the Andrews earthquake, its abrupt stress drop, and the strong directivity toward the repository, Andrews and others (2007) considered these ground motions to be near maximal, but went on to note that limiting conditions of the initial stress state (coefficient of friction of 0.6) and dynamic friction (equal to 0) would allow for ground velocities and the faulting displacement to be larger by a factor of 4/3. The horizontal PGVs are still less than the 10^{-8}/yr PGVs of the 1998 PSHA extended to these hazard levels. The inclusion of Mohr-Coulomb plastic yielding reduces the horizontal PGV to 3.59 m/s and the vertical PGV to 4.29 m/s.
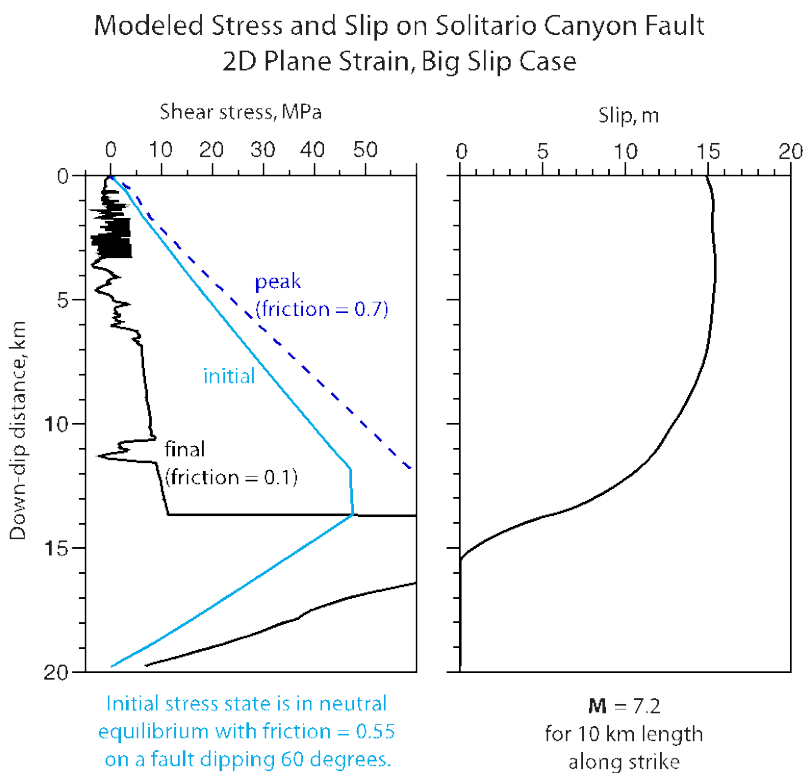
Figure 15. Plots of stress and fault slip on the fault plane as a function of down-dip distance for the Andrews earthquake, a hypothetical, two-dimensional, complete stress-drop earthquake on the Solitario Canyon Fault. Note that this event produces 15 meters of surface faulting. Modified from Andrews and others (2007, figure 7).

These calculations are complicated and time-consuming, and it was important to the ExGM research program that they be reproducible. This was achieved through the SCEC Dynamic Rupture-Code Validation Group, led by Ruth Harris (USGS). Beginning in 2003, this focus group of ~20 scientists has patiently and painstakingly worked through a series of modeled benchmark earthquake ruptures of increasing complexity to validate various numerical methods to calculate ground motions arising from the various benchmark ruptures (Harris and others, 2009). Benchmarks 12 and 13 are simplified versions of the Andrews earthquake, using a uniform medium with no depth-dependence of

the velocity structure. Benchmark 12 is for the elastic case and 13 for the inelastic case. Each benchmark includes two- and three-dimensional model ruptures (the Andrews and others [2007] calculations were limited to two dimensions); neither benchmark includes topography or velocity structure, which were included in the Andrews and others (2007) models. Results from all participants in these benchmark exercises showed good agreement in both the elastic and inelastic cases (for example, figures 16 and 17 from Harris and others [2007]). In the 3D cases, PGV is about 0.6 times that in the 2D cases.

Benchmark: tpv13-2d (2D Version of TPV13)

File: body-010st000dp003 (body -1.0 km, strike 0.0 km, depth 0.3 km)

Field: v-vel (vertical velocity)

(Back to Field List)   (Logout)

(<<) (<)   Page 1 of 1   (>) (>>)
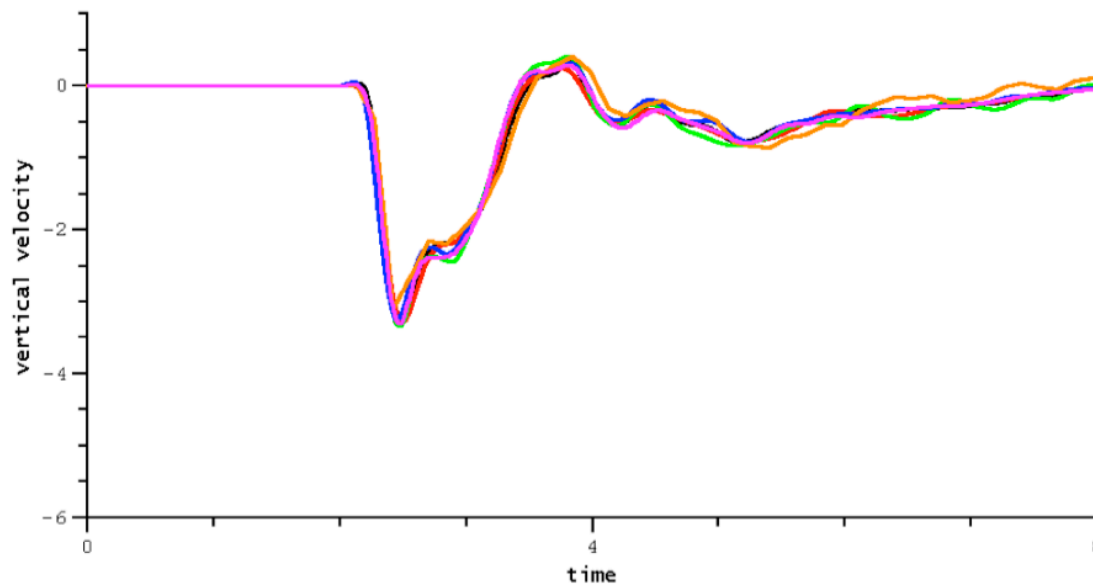
Figure 16.   Plot showing dynamic rupture code comparisons for benchmark 13 (plastic case), two-dimensional fault model, vertical velocity (meters per second, m/s), using parameters from Harris and others (2009). A low-pass Butterworth filter at 3.0 Hertz has been applied. Time is in seconds, and velocity is in m/s.
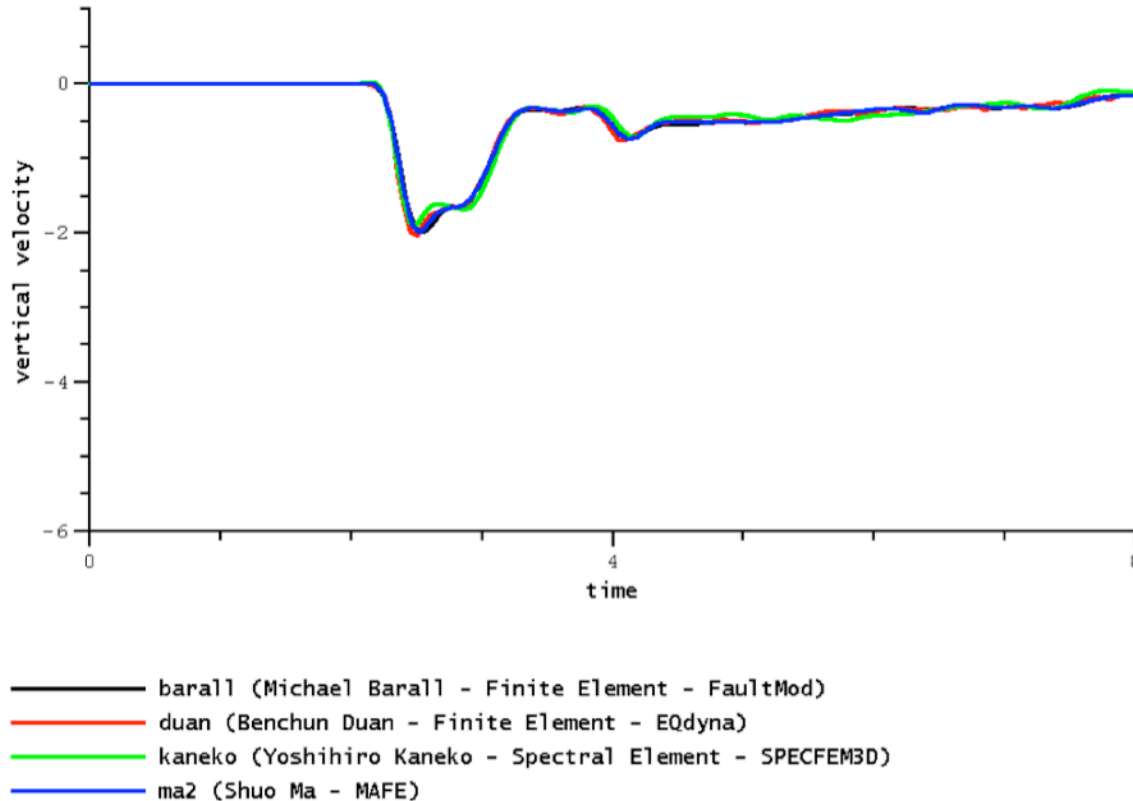
Figure 17.   Plot showing dynamic rupture code comparisons for benchmark 13 (plastic case), three-dimensional fault model, vertical velocity (meters per second, m/s), using parameters from Harris and others (2009). A low-pass Butterworth filter at 3.0 Hertz has been applied. Time is in seconds, and velocity is in m/s. Note also that modelers are not all the same as for figure 16, depending on the capability of their existing codes. The two-dimensional Andrews and others (2007) calculations are not shown here.

Figure 18 compares the two-dimensional calculations for the Andrews earthquake for vertical velocity at the repository site, as done in Andrews and others (2007), which includes both topography and crustal structure at depth, and as done by D.J. Andrews for benchmark 13, which includes neither. There is not much difference, which is to say that there is not much amplification arising from the near-surface tuffs.

The large vertical PGVs calculated at the repository level for the Andrews earthquake result from the strong directivity in the forward propagation direction amplified by the super-shear-wave speed (near the P-wave velocity) rupture induced by the strong and abrupt stress drop for this

28

earthquake. Andrews and others (2007) anticipated reduction of large vertical PGVs by means of irreversible compaction of the Calico Hills Formation, a sequence of low-strength, high porosity volcanic tuffs that underlies Yucca Mountain. At the 2007 ExGM/SCEC workshop, Andrews presented calculations with compaction occurring in the Calico Hills Formation. The compaction constitutive relation was adopted from data on sandstone, with the crushing strength adjusted to be only slightly greater than stress in the Calico Hills Formation. The resulting horizontal PGV was hardly changed, but the vertical PGV in the event with 15 m slip was reduced to 3.1 m/s.
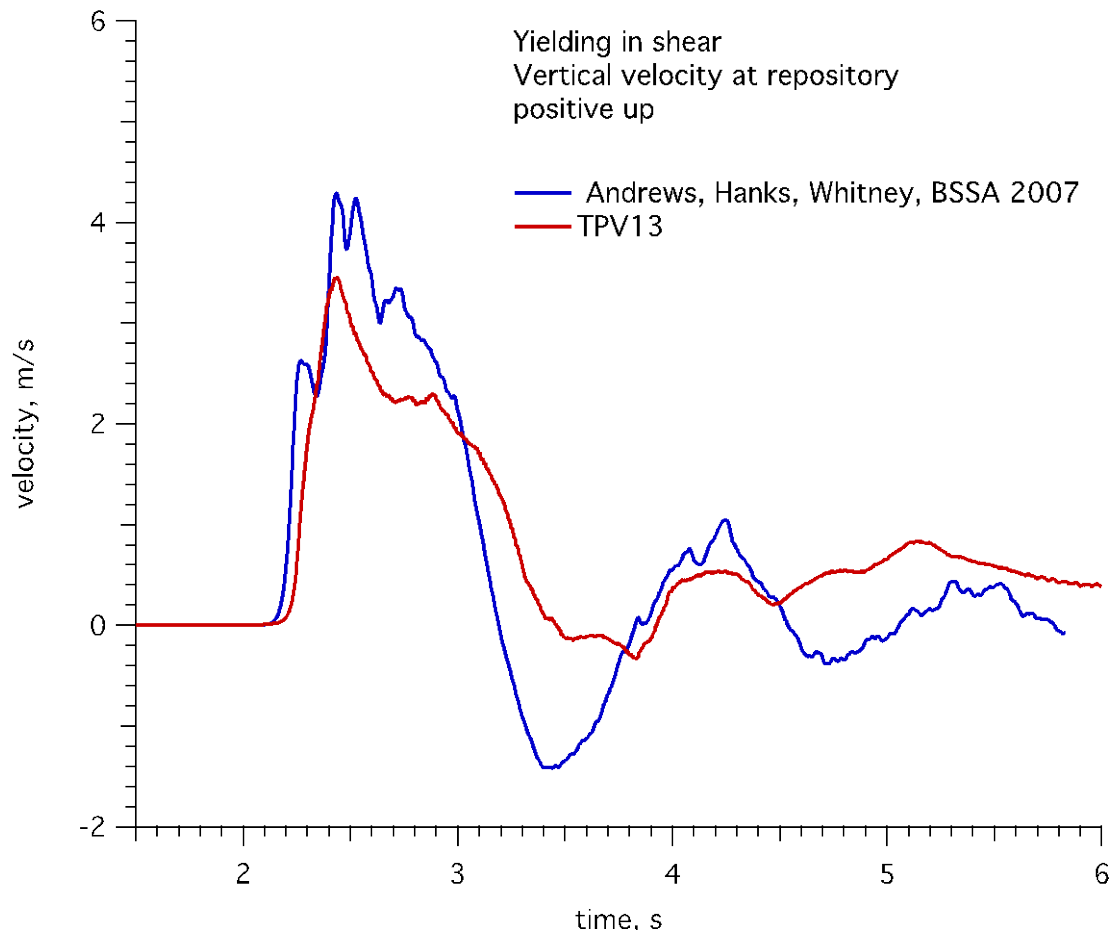
Figure 18. Plot showing comparison of the vertical velocity at the repository for the Andrews earthquake, from Andrews and others (2007) and for the Benchmark 13 calculation, inelastic, uniform half-space, no topography.

The Calico Hills Formation is a series of ash-flow tuffs with highly variable porosity, degree of vitrification, and mechanical properties. Just above the water table, this formation underlies the proposed repository by ~300 m (fig. 8) and the Yucca Mountain crest by 600–700 m. It is exposed at the surface, however, in its type locality, the Calico Hills northeast of Yucca Mountain and Fortymile Wash (fig. 1). As part of the site characterization studies, laboratory strength tests were conducted on Calico Hill Formation samples. These tests, however, were focused on Coulomb failure of the stronger members of the formation. Lockner and Morrow (2008) tested core samples of the poorly vitrified, low-strength, high-porosity members of the Calico Hills Formation. They found that these weak tuffs were prone to fail by pore collapse or by shear-induced compaction, similar to the failure mechanisms of porous sandstones. These failure mechanisms, characterized by distributed rather than localized strain,

can involve up to 90 percent irrecoverable energy losses (exceeding 10^6 Joules per cubic meter [J/m^3] for 0.1 percent strain). This pore collapse mechanism should lead to significant energy dissipation of dynamic stress waves that traverse the Calico Hills Formation. The weakest samples of the Calico Hills Tuff had a crushing strength consistent with the value Andrews used for his presentation at the 2007 ExGM/SCEC 2007 workshop, so the maximum vertical PGV in an event with 15 m slip can be expected to be roughly 3.1 m/s. Ground-motion calculations using the constitutive relation derived from the laboratory data for the Calico Hills samples remain to be done.

In studies motivated in part by Andrews and others (2007), Duan and Day (2009), and Templeton and others (2010) have investigated the dynamics of nonplanar faults with off-fault plastic yielding. Duan and Day (2009) used rupture simulations with Mohr-Coulomb strength limits to explore the sensitivity of extreme ground motion estimates at Yucca Mountain to both the numerical method and physical assumptions. The model and calculations of Andrews and others (2007) form the starting point for the study. Calculated time histories closely track those of Andrews and others (2007) with the small differences (for example, typically ~5–10 percent differences in peak ground velocity) being easily attributable to small differences in the calculation of the initial equilibrium stress state.

Duan and Day (2008) examined how inelastic strain concentrates near a fault kink and the manner in which plastic yielding at the kink then affects both dynamic rupture and seismic radiation. They found that extensive inelastic deformation concentrates near a restraining bend, particularly on the side of the fault associated with rupture-front extensional strains. The extensive inelastic deformation reduces high-frequency radiation from the kink and the reduction is significant above several Hertz.

Templeton and others (2010) investigated dynamic branch activation for the Solitario Canyon Fault (SCF), finding that the only likely candidates for branch activation in the hanging wall of the SCF are the more steep, westward-dipping intrablock splay faults. Like Duan and Day (2010), Templeton and others (2010) found that elastic-plastic response near a branch junction reduces peak ground velocities and accelerations at the proposed repository site.

The additional studies mentioned in this section support the findings of Andrews and others (2007) that physical limits to earthquake ground motions can be set by physical limits to stress differences that can arise in the source region or by inelastic, dissipative rheologies between the source region and surface (or near-surface) sites. Crustal earthquake stress drops are typically much smaller than the stress drop set for the Andrews earthquake, which, according to the research of Dewey and Boore (described later in this report in the section "m_b-**M** Stress Drops for Continental Crustal Earthquakes subsection of the Event Frequencies"), is some 2 to 3 standard deviations removed from the (logarithmic) mean of 65 bars.

Unexceeded Ground Motion

Unexceeded ground motions at Yucca Mountain are expressed in the ages of fragile geologic structures that have survived in the absence of some level of ground motions, which, had they occurred, would have damaged/destroyed these features. At Yucca Mountain, there are two classes of such fragile geologic structures: the lithophysal units of the Topopah Spring Tuff, the repository host horizon, and precariously balanced rocks (PBR) and stacks of rocks on the west face of Yucca Mountain.

Lithophysal Units

The Topopah Spring Tuff Formation underlies Yucca Mountain and is the host horizon for the underground repository. It consists of ~300 m of silica-rich, densely welded, pyroclastic flow units laid down 12.8 million years ago and contains the distinctive upper (Tptpul) and lower (Tptpll) lithophysal

units. Lithophysae are cavities that form in pyroclastic flows and volcanic tuffs as a result of the volcanic gases exsolved during the cooling process, forming bubbles within the cooling rock mass. These cavities constitute approximately 10–30 percent of the rock mass volume. Tptpul lithophysae tend to be roughly spherical, uniform in size and distribution, and small in dimension (diameters of 1 to 10 cm); the matrix material is largely unfractured.

Tptpll lithophysae are more irregular in shape, size, and distribution (fig. 19). They range in size from about 1 cm to nearly 2 m in dimension and have spacing that ranges from about 10 to 50 cm, but may be more closely spaced in local regions. The shapes range from elliptical or spherical to irregular, cuspate and merged cross sections, or elongate along fractures. The matrix between lithophysae often has a fabric of short length (<1m) and discontinuous cooling fractures that have a primary vertical orientation. These fractures typically are not interconnected and do not intersect lithophysal cavities.

Approximately 85 percent of the emplacement drifts of the repository are to be excavated within the lower lithophysal unit (Tptpll), 250 to 300 m below the ground surface. The overall porosity of Tptpll due to the lithophysae is ~20 percent, weakening this unit considerably with respect to the passage of seismic waves. Very few of these lithophysae are cut by cooling fractures or joints, and none show appreciable effects of damage, offsets, or collapse that can be attributable to the passage of seismic waves.

The Yucca Mountain Project (YMP) was aware long ago that these observations spoke against ground-motion amplitudes of the sorts associated with extreme ground motions (BSC, 2005). Section 6.3.4, Conclusions from Geologic Observations, of BSC (2005) reads:

> Data from the systematic characterization of fractures in boreholes and detailed examination of panel maps and photographs in the ECRB Cross-Drift supports a cooling-related origin for most fractures observed in underground exposures of lithophysal rock of the Topopah Spring Tuff. Collapsed lithophysae and widespread fractures with characteristics (shear offset, inter-lithophysal connections) that would be expected if the shear strain threshold for lithophysal rock had been exceeded at Yucca Mountain are not seen. Although the samples used in the studies are limited in size and scale relative to the entire rock mass, one of the underlying strengths of these studies is that samples and study locations are spatially and stratigraphically distributed throughout the rock mass. Thus it is concluded that the shear-strain threshold for failure of lithophysal rock at Yucca Mountain has not been exceeded since the rocks were deposited about 12.8 million years ago.

YMP then initiated a series of laboratory strength tests of very large samples (288 mm diameter) and discrete-element numerical simulations to define the shear-strain threshold for observable lithophysal rock-mass damage, as well as the types of damage that should be observable, had these shear strains been reached or exceeded. Shear strains at failure mostly ranged from 0.10 to 0.25 percent, with a mode of the strain distribution of 0.16 percent. The Particle Flow Code PFC2D (Itasca, 2012) was the basis for determining the types of failures that would arise in the lithophysal units under these shear strains. Ground-motion simulations were then calculated on the basis of the point-source stochastic model to determine the PGV values that could generate these shear strains. For these calculations, the dynamic-failure properties of the tuff were grouped in two bunches, upper mean tuffs (UMT, stronger, more linear) and lower mean tuffs (LMT, weaker, less linear).

For the LMTs, PGVs of 1.0 to 2.3 m/s produce the failure shear strains given above; the peak of these PGV distributions is near 1.7 m/s. For the UMTs, PGVs of 1.7 to 4.8 m/s are necessary to achieve the failure strains; the peak of the UMT PGV distributions is near 3.2 m/s. BSC (2005) took these values as a "bound to horizontal PGV experienced at the waste emplacement level at Yucca Mountain." In our framework, they are unexceeded ground motions, ground motions that have not been exceeded since the lithophysal units solidified ~12.7 Ma.

A 17-page summary of the lengthy BSC (2005) report was prepared by Mark Board, from which the prose above has been developed. It is included here as appendix III.
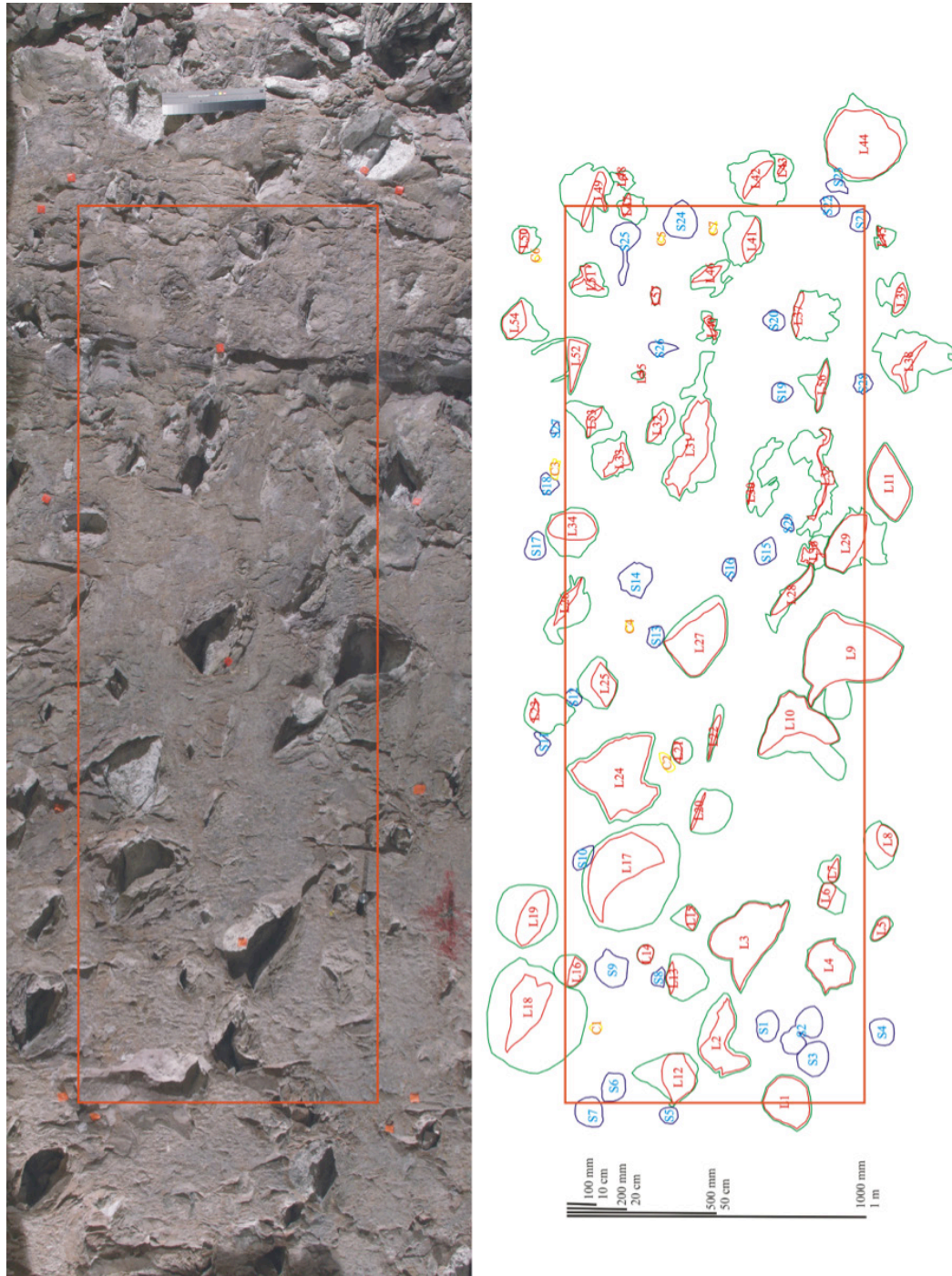
Figure 19. Photograph and panel map (3 m x 1 m) from the Enhanced Characterization of the Repository Block tunnel sidewall in the lower unit of the Topopah Springs Tuff, showing traces of lithophysal cavities and vapor-phase alteration rims. Up is to the left.

Precariously Balanced Rocks (PBRs)

Over the past 15 years, J.N. Brune and his colleagues at the University of Nevada, Reno, have discovered and documented the locations of ~100 PBRs on the west face of Yucca Mountain. An early reference is Brune and Whitney (2000), and the most recent is Purvance and others (2009), from which most of this section is abstracted. The word "precarious" is used loosely here, unconstrained by the early terminology of Brune (1996) that a "precarious rock" would topple at ≤0.3 g while a "semiprecarious rock" would topple at 0.3 to 0.5 g.

PBRs commonly form along or within the Middle Ledge, an exposure of the densely welded, crystal-rich member of the Topopah Spring Tuff. The abundance of PBRs in the Middle Ledge is due to its angular, subhorizontal cooling joints and its relative resistance to erosion; the Middle Ledge is the most obvious cliff-forming unit on the west face of Yucca Mountain. PBRs are found less frequently in the Tiva Canyon Tuff, which forms the west-facing crest of Yucca Mountain but is less resistant to erosion due to the presence of lithophysae. PBRs of the Middle Ledge and Yucca Mountain crest are on the footwall of the Solitario Canyon Fault, within a kilometer of the repository footprint to the east and the Solitario Canyon fault to the west. Figure 20 shows the PBR Tripod, a marginally stable stack of rocks located in the Middle Ledge.

We need to know two things about these PBRs: the amplitude and frequency range of the ground motions necessary to topple or overturn them, and the length of time that these PBRs have been in their fragile state of existence. The susceptibility of PBRs to overturning motions is encapsulated in the rock (or stacks of rocks') fragilities. Fragility calculations have evolved a great deal in the past 20 years, from simple horizontal load tests to estimate a toppling acceleration for the rock, given approximate estimates of its mass, center of gravity, and balance points, to three-dimensional determinations of the rock's shape and volume through sophisticated photogrammetry techniques and advanced numerical techniques that simulate the three-dimensional response to ground motion of rocks or complex arrangements (stacks) of rocks (Purvance and others, 2009). Parameterizing the toppling/overturning motions has become more complicated as well, depending on both PGA and PGV.

Purvance and others (2009) have determined the three-dimensional fragilities of nine of these fragile geologic structures, five of them single balanced rocks, often with complex geometry, and the remaining four being stacks of rocks with very complex geometry.

For this report M.D. Purvance has calculated the 10-, 50-, and 90-percent overturning probabilities as a function of PGA and the ratio PGV/PGA, shown in figure 21. At 50 percent overturning probability, the single rocks Matt Cubed, Nichole, and Sue will all overturn at PGA of ~0.5 *g*, even if PGV is small (note that the Sue and Nichole curves are virtually identical and overlap); for modest PGVs of tens of cm/s they will overturn at smaller PGAs. The rock stacks Tripod and Whitney are similarly unstable (unsurprisingly in the case of Tripod, fig. 20) for these earthquake ground motions, which seem to us to be modest for sites nearly straight updip of the **M**~6.5 earthquakes on the SCF that we are interested in, specifically the 77-ka earthquake.

Figure 20. Photo of the precariously balanced rock called "Tripod," a marginally stable stack of rocks in the Middle Ledge of the Topopah Spring Tuff, west face of Yucca Mountain. The stack is approximately 1.5 m tall. Photograph by T.C. Hanks.
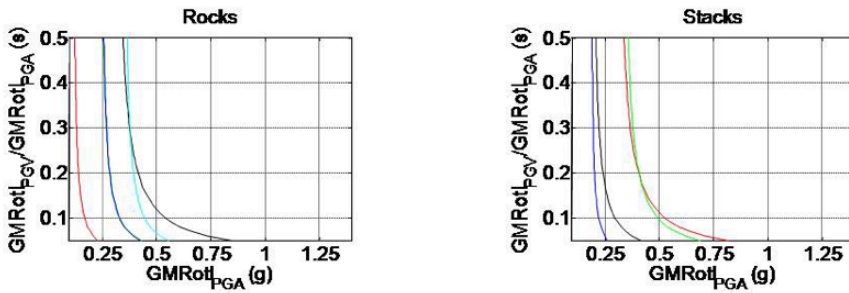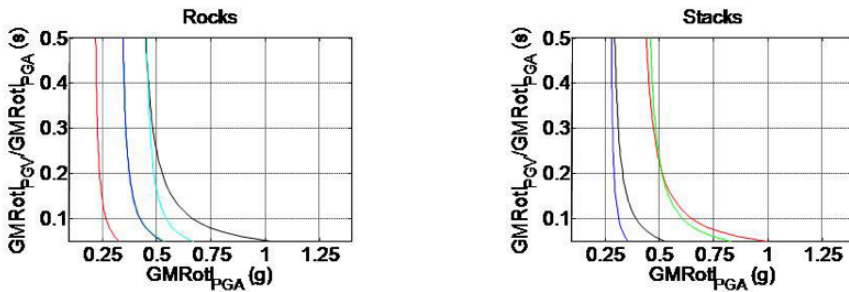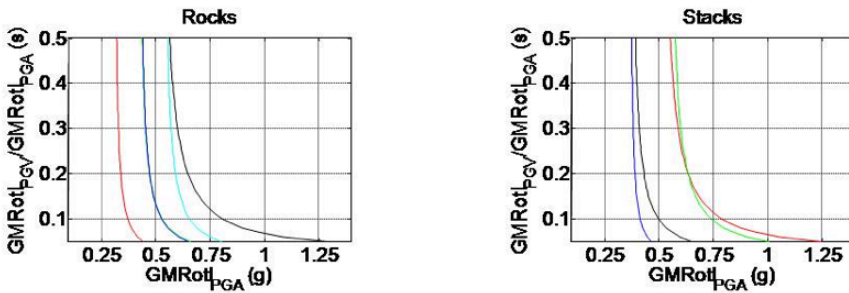
Figure 21. Plots showing overturning probabilities in terms of peak ground acceleration (PGA; abscissa) and the ratio peak ground velocity to peak ground acceleration (PGV/PGA; ordinate) for the rocks (left) and stacks of rocks (right) on the west face of Yucca Mountain (PGA and PGV are obtained from the sensor-orientation-independent measures of ground motion GMRotI, as defined in Boore and others, 2006). Top, 10 percent; middle, 50 percent; bottom, 90 percent. Color keys for the several PBRs are given below the 90 percent overturning probabilities.

Purvance and others (2009)subjected all nine of these structures to ground motions calculated for the 77-ka earthquake by Andrews and others (2007), which offers several models of the 77-ka earthquake based on the fault-displacement hazard calculated for the SCF by Stepp and others(2001). According to Purvance and others (2009):

The 1.3 m subshear event overturns two of the objects (Matt Cubed and Whitney) and the 2.7 m subshear event overturns five of the nine objects investigated (Matt Cubed, Nichole, Pillow, Tripod, and Whitney). The 1.3 m supershear event, on the other hand, overturns none, and the 2.7 m supershear overturns three of the objects (Matt Cubed, Tripod, and Whitney). Should all of these objects have resided in their current positions for the past 77 ka, they would indicate that the 2.7-m slip scenarios as modeled by Andrews and others (2007) produce unrealistically high amplitude ground motions. In fact, the 1.3 m subshear scenario is also inconsistent with 77-ka ages for these Yucca Mountain features.

We saw earlier, however, that ground motions arising from two-dimensional calculations are typically 1.5 times greater than for three-dimensional realizations of these earthquakes along the SCF. Purvance and others (2009) also subjected these nine fragile structures to 16 ground-motion time histories created by Wong (2004) at Point B (the repository horizon; Stepp and others,2001) at 10^{-5}/yr and 10^{-6}/yr hazard levels for postclosure analysis of repository performance. Thirteen of the sixteen ground-motion time-histories at 10^{-5}/yr overturned most or all of the nine PBRs. The 10^{-6}/yr ground motions toppled almost all of them.

Were these fragile geologic structures in similar states of fragility at the time of the 77-ka earthquake—or even older times? Implicit here are a host of questions of how erosion/weathering works to isolate a rock or stack of rocks from the (often massive) geologic formation that used to surround them. Moderate to steep slopes are necessary to carry away the erosional detritus of the material surrounding the incipient PBR, as is at least modest precipitation to transport this material. The rate at which isolation will occur will also depend on the rock lithology, density, and in the case of these volcanic rocks, the extent of welding.

We noted earlier the two erosional mechanisms in play on the west face of Yucca Mountain: the block-by-block retreat of the cliff-forming units in which the PBRs are located, and the grain-by-grain weathering of these blocks, whether they are weathering in place or in their new homes as boulders on the pediment slopes below. The latter process proceeds very slowly, ~2 m/m.y. in these parts due to the semiarid climate of the Holocene and the rare episodes of accelerated periglacial weathering during the Pleistocene.

The retreat rate of the cliff-forming units, ~1 m/100 ka is controlled by the block-by-block rate, which we regard as the rate-limiting factor in the formation of PBRs on the west face of Yucca Mountain. This is to say that we do not often expect to find PBRs much older than ~200 ka. They can, however, be much younger, depending on recent of falls of adjacent rocks.

Finally, the block-by-block retreat of the Tiva Canyon Formation and the Topopah Spring Tuff is controlled by the (cooling) joint spacing within these units, which typically ranges from 0.5 to 3.0 m. Important to the stability of the PBRs, once formed, is that these units are back-tilted to the east by ~5°, away from the unstable, down-slope direction to the west. All of this presents unusual challenges for determining the fragility age of each of the rocks and stacks of rocks of interest here.

The ExGM research program determined exposure ages of various, presently exposed faces either on the PBR of interest or on the bedrock adjacent to or below it, using abundances of ^{36}Cl extracted from alkali feldspar mineral separates. Appendix I table 2 shows the exposure-age data we have assembled for the Yucca Mountain PBRs, northern and southern cliff profiles at the crest, and boulders now residing on the slopes beneath the cliffs. Minimum ages (for zero-erosion rate) are given

with their one-sigma internal uncertainties. Uncertainties for the preferred ages (the minimum age corrected for 2 m/m.y.) are probably best given by multiplying the uncertainty of the minimum age times the ratio of preferred/minimum ages. When the minimum age is ≥244 ka, we consider it to be an equilibrium erosion rate, the true exposure age of the surface in question then being indeterminate.
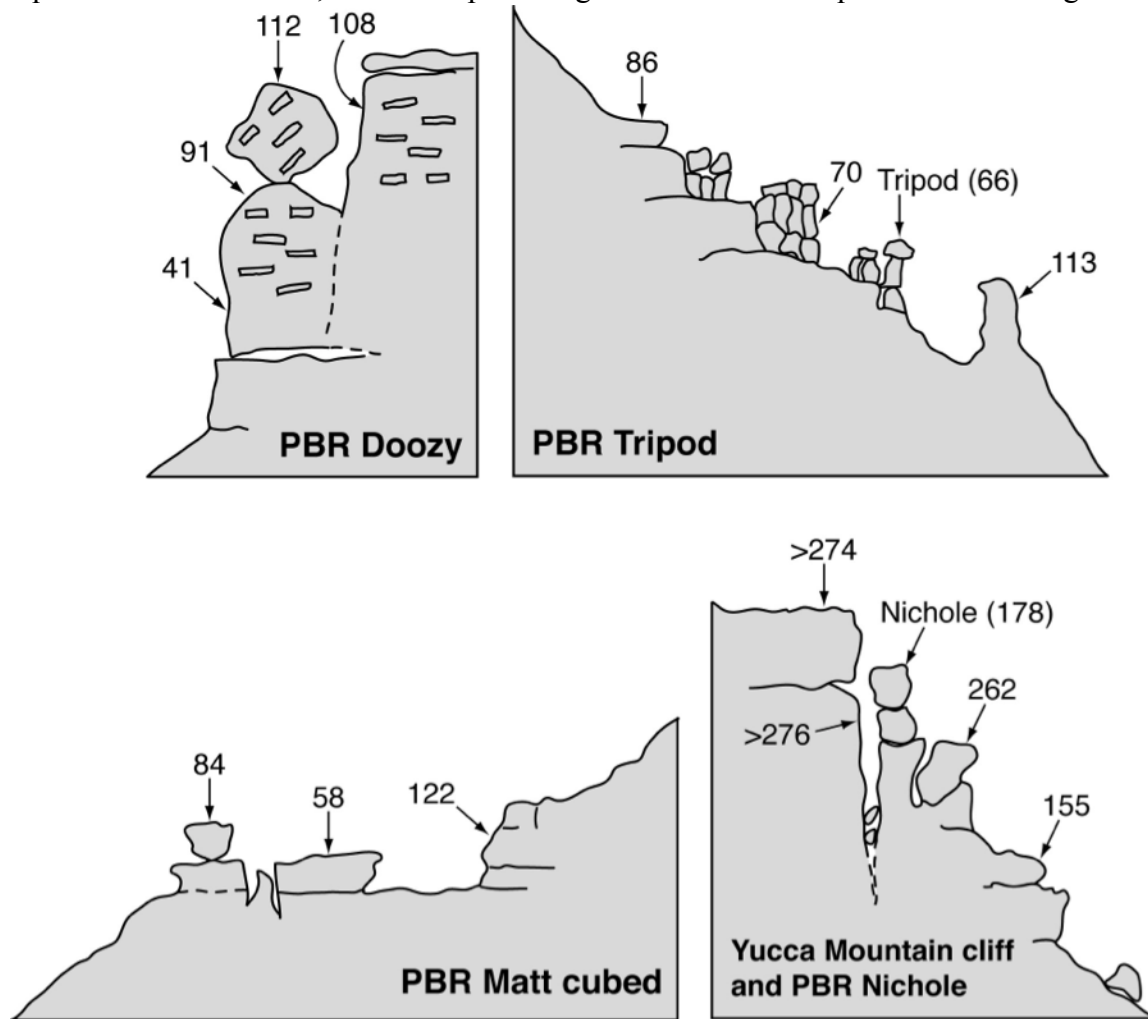
Figure 22. Elevation profile sketches of the PBRs Doozy, Tripod, Matt Cubed, and Nichole. The downhill direction is to the west. The numbers specify exposure ages, in ka (appendix I table 2).

The sampling strategies, exposure ages, and our estimates of fragility ages are discussed below for four PBRs, with reference to figure 22, a simplified two-dimensional representation of what is often a complicated, three-dimensional problem (fig. 23). The exposure ages we report below are mostly the minimum ages, corrected for the low, grain-by-grain erosion rates of 2 m/m.y. For exposure ages of 244 ka and greater, however, we are no longer retrieving minimum ages but rather the secular erosion-rate abundances that attend the nominal erosion rate of ~2 m/m.y.

The PBR Doozy is located in the Tiva Canyon cliff, just below the crest of Yucca Mountain. Doozy became a balanced rock by pronounced erosion of both the balanced boulder and the pedestal rock below it. Exposure ages of the top surface of Doozy (112 ka) and the joint face behind it (108 ka) are nearly the same, indicating that Doozy has been separated from the cliff for more than 100 ka. A date of 91 ka on the upper surface of the pedestal rock beneath Doozy suggests that erosion along the

horizontal joint between the two rocks was well advanced by 91 ka and that Doozy was fragile at that time. Doozy is very fragile at present due continued erosion.

The tilted lithophysal cavities in the boulder indicate that Doozy has rotated at some remote time in the past, perhaps as long ago as 108–112 ka. Unfortunately, fragility calculations were not performed for Doozy (because it has rotated), but it is the most unstable PBR we know of on the west face of Yucca Mountain. We estimate its fragility age to be 90–110 ka and believe it survived the ground motion of the 77-ka earthquake.

Tripod and Matt Cubed have been etched out of the Middle Ledge of the Topopah Springs Tuff. The exposure age of 66 ka on Tripod, with a similar age of 70 ka on an adjacent surface, indicates that Tripod was likely a freestanding stack at 66 ka. Similar to Doozy, continued erosion at the base of Tripod and along joints has made Tripod a more fragile feature now than it was 66 ka. We estimate the fragility age of Tripod to be 60–75 ka, making it an unlikely constraint on the 77-ka earthquake.

Matt Cubed is a freestanding boulder on an eroded horizontal bedrock joint. The exposure age of the top of Matt Cubed is 84 ka, and the exposure age of 58 ka on bedrock surface upon which it sits suggests that Matt Cubed was freestanding at that time. At the present time, Matt Cubed is the least stable of the nine rocks and stacks of rocks analyzed by Purvance and others (2009), but probably was more stable at the time of the 77-ka earthquake. We estimate the fragility age of Matt Cubed to be 50–70 ka.

Nichole is a PBR in the Tiva Canyon cliff of the Yucca Mountain crest. Both the cliff face behind Nichole and the crest surface yield minimum exposure ages of 274 ka; the true ages may be significantly older. An upper surface of a remnant of the former cliff located about 2 m down slope of Nichole is 262 ka, which indicates the present topography around Nichole is older than 250 ka. The upper surface of Nichole is 178 ka, which suggests that Nichole has been an unstable boulder stack for at least 178 ka.

Len is a boulder stack in the Middle Ledge (fig. 23); note how the faulting-controlled, back-tilted cooling joint (to the east) of the volcanic units stabilizes Len against failure to the west. The exposure age of the outer surface of the uppermost rock in this stack is 104 ka; the adjacent bedrock surface behind the stack has been exposed for 63–77 ka, indicating this stack was isolated by 63 ka and was likely fragile at that time.

In addition to the exposure ages we have just discussed, fragility ages are also available for these PBRs from the "varnish microlamination" (VML) methodology described by Liu (2003). Desert varnish, when present on late Quaternary boulder or rock-wall faces in arid environments, accumulates in climatically controlled Mn-rich/Si-poor and Mn-poor/Si-rich laminations, developing a micro-stratigraphy that can be accurately dated. For PBRs well covered by these varnish laminations, it is likely that a PBR shape has changed hardly at all over the varnish accumulation time. The VML ages for Yucca Mountain PBRs (T.Z. Liu, unpub. data, 2012), are 12 to 17 ka, which we take here to be 15 ka. We also take 15 ka to be the minimum fragility ages of the Yucca Mountain PBRs.

The exposure ages we discussed earlier in this section are much older than this 15 ka lower-bound fragility age and thus more likely to be closer to maximum fragility ages, insofar as local (grain-by-grain) erosion has had more time to make these structures more fragile. The amount of local erosion is quite variable from one PBR to another, however, and probably has a lithologic dependence. Doozy in the Tiva Canyon Tuff, for example, shows considerable rounding due to local erosion, while the rock stack Len in the Middle Ledge (fig. 23) shows very little.

For all of this, only Doozy and Nichole are likely to provide constraints on ground motion amplitudes that were not exceeded during the 77-ka earthquake. Each of these PBRs, however, is a point in hazard space, as we have already seen (fig. 13) and will see again at the end of this report. We also

develop a time-dependent fragility model to explore the sensitivity of these PBR unexceeded ground motions to fragilities that evolve with age in the concluding section of this report.
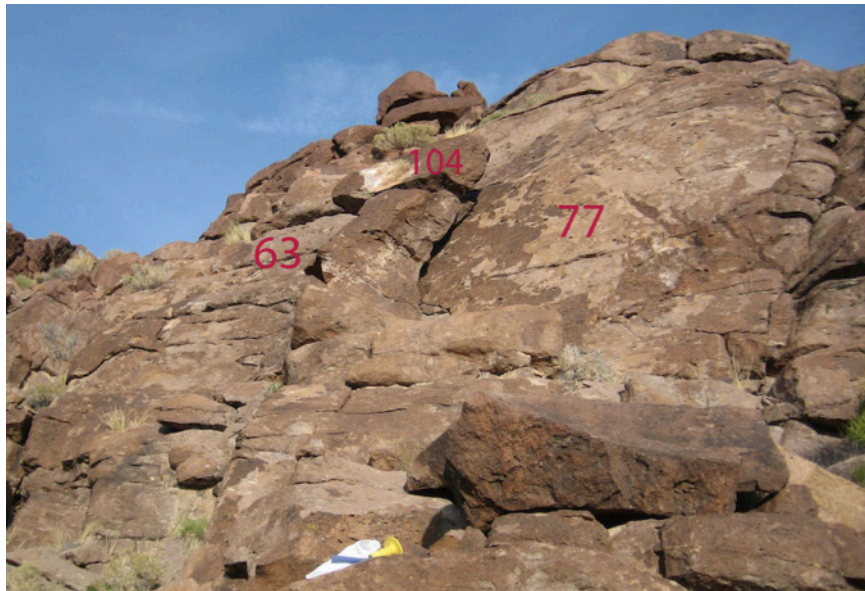
Figure 23. Photo of the rock stack Len in the Middle Ledge of the Topopah Spring Tuff, ~0.5 km south of Tripod. Red numbers denote surface exposure ages in ka.

Event Frequencies

An event frequency describes the rate at which the event occurs, which, if small enough, is also the probability of the event occurring. PSHA employs one event-frequency model for earthquake occurrence (seismic source characterization, SSC) and another for the occurrence of ground motions given the earthquake (ground motion characterization, GMC). SSC describes the chance of an earthquake with a specific magnitude occurring at a specific location. GMC describes the chance of a ground motion occurring at a specific site given that an earthquake of a given magnitude and location has occurred. In quantitative analyses, these "event frequencies" are given as probability distribution functions (pdf).

The shape of these pdfs, in turn, determine the shape of the hazard curves constructed from them. In general, narrow pdfs lead to steep hazard curves (those that decrease rapidly with increasing ground-motion amplitude) and broad pdfs lead to flat hazard curves. In most cases, the upper tail of the ground-motion distribution controls the hazard curve at low annual probability levels. Of particular interest to ExGM–and quite generally to any PSHA–is whether or not the GMC pdfs truncate at low-probability, large-amplitude ground motions, which is to say, for extreme ground motions.
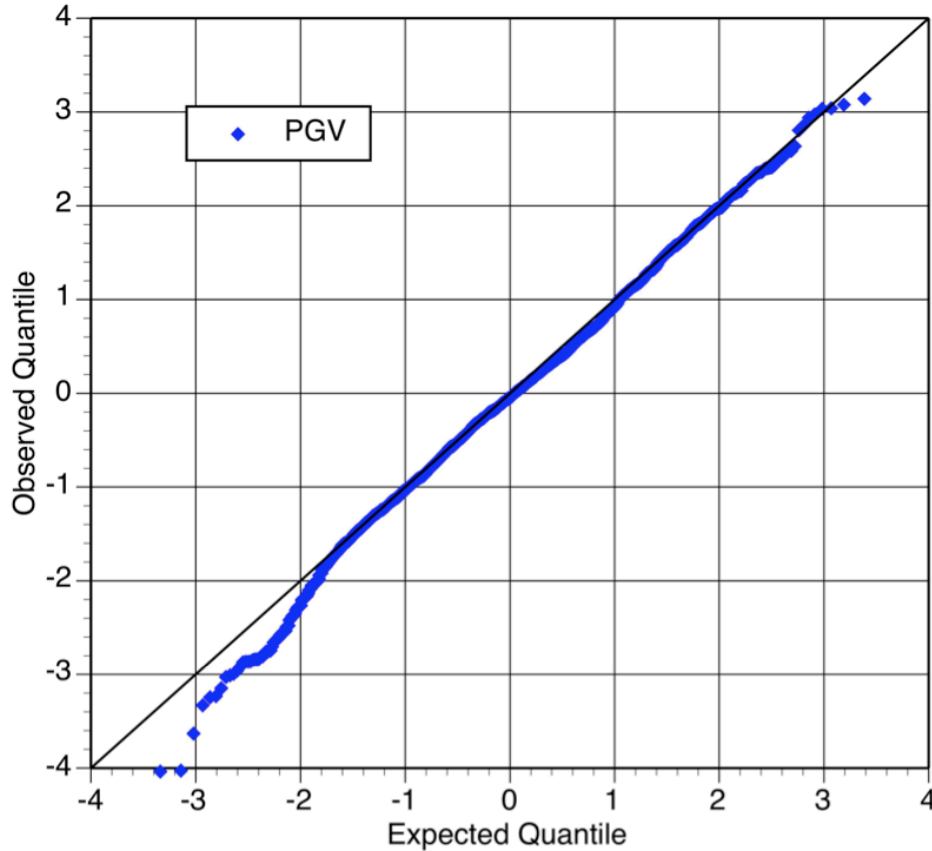
Figure 24. Plot showing the observed versus expected quantiles of peak ground velocities (PGV), in a log-normal distribution for the Next Generation of Attenuation database (Chiou and others, 2008). Quantiles are defined in the text.

Figure 24 is a "quantile-quantile" plot, sometimes referred to as a normal probability plot, of Next Generation of Attenuation (NGA) PGV residuals with respect to the Abrahamson and Silva (2008) NGA model. (The Next Generation of Attenuation project [Power and others, 2008] was a major effort beginning in 2003 to update ground-motion prediction equations [GMPE]. Abrahamson and Silva [2008] is one of the four NGA GMPE models published in 2008.) In figure 24, the "expected quantiles" are logarithmic PGV residuals divided by the standard deviation (epsilon values, ε) of the log-normal pdf. It shows that there is no basis for truncating the log-normal pdf for PGV at its upper end up to at least $\varepsilon=3$. Most of the large, positive residuals in figure 24, however, are derived from small or modest PGVs that happened to be large with respect to the median prediction. ExGM is more concerned with the larger/largest PGVs and their pdfs for which the data sets are much smaller and the corresponding uncertainties are larger.

The ExGM research program included studies of the frequency of the largest recorded PGAs and PGVs and the largest reported surface displacements for both historical and late Quaternary normal-faulting earthquakes. Dewey and Boore (2008) investigated the distribution of crustal earthquake stress drops inverted from the large, global set of m_b-M_w pairs. Also, Baltay and others (2010) explored a long-standing, seismological curiosity little known to Yucca Mountain scientists and engineers, the increase of apparent stress with magnitude for the western U.S., first reported by Mayeda and Walter (1996).

Of particular interest here to ExGM are two issues. First, what are the largest reported/known values of ground-motion amplitudes, faulting displacements, and earthquake stress drops? Second, what do their pdfs look like and, in particular, is there any observational basis for truncating them?

Exceptionally Large PGAs and PGVs

Instrumental recordings of strong ground motion have always been the heart of the ground-motion characterization (GMC) half of PSHA, and the aleatory variability of various ground-motion amplitude measures, including PGA and PGV, are the principal cause of the extreme ground motions that concern us here. As we have seen in figure 24, these ground-motion pdfs are well characterized by logarithmically normal (Gaussian) functions ("log-normal distibutions"). A typical (logarithmic) standard deviation (sigma) of these ground-motion pdfs corresponds to a multiplicative factor of 1.5 to 2. In practice, then, these pdfs are often truncated at their upper end, typically at 2 to 3 sigma, but there is no empirical or theoretical justification for such truncations (fig. 24), with the exception of true physical limits.

Anderson (2010) is a thorough examination of the 100 largest instrumentally recorded PGAs and PGVs, drawn from a list of 255 records for which at least one component of acceleration is >0.5 g or at least one component of velocity is >0.5 m/s (Anderson, 2010, table 1). This list, in turn, is drawn from a collection of more than 100,000 accelerograms. Of the 100 largest PGAs, 35 were in excess of 1 g, but only one was in excess of 2 g: a 2.4 g record of the Nahanni (Dec. 23, 1985; **M**=6.8) earthquake. (Anderson (2010) does not include the Iwate-Miyagi earthquake (June 14, 2008; **M**=6.9) and its 4 g vertical accelerations at station IWTH25. Of the 100 largest PGVs, 40 were in excess of 1 m/s, but only two were in excess of 2 m/s (3.2 and 2.45 m/s), both from the Chi-Chi earthquake (Sep. 20, 1999; **M**=7.6). Earthquakes as small as **M**=4.8 contributed to the list of the 100 largest PGAs, while **M**=5.7 was the smallest event for the PGV list. A total of 79 different earthquakes contributed one or more records to this data set. Normal-faulting, crustal earthquakes of interest to Yucca Mountain, however, provide fewer than 5 percent of the records in the databases searched by Anderson (2010) and an even smaller percentage of the 100 largest PGA and PGV records. Again with respect to Yucca Mountain, very few of the largest PGAs and PGVs are recorded on hard rock (V_{S30}>1500 m/s). Strasser and Bommer (2009) conducted a study similar to Anderson (2010), compiling and analyzing all records with PGAs>1g and PGVs>1 m/s. This study found that large PGAs and PGVs arise from a variety of disparate source, wave-propagation, and site effects.

Figure 25 shows PGV as the geometric mean of the two horizontal components (the square root of their product) for the largest values in Anderson (2010) as a function of magnitude; site condition is parameterized with V_{S30}, determined from the average slowness of the upper 30 m, shown in color.
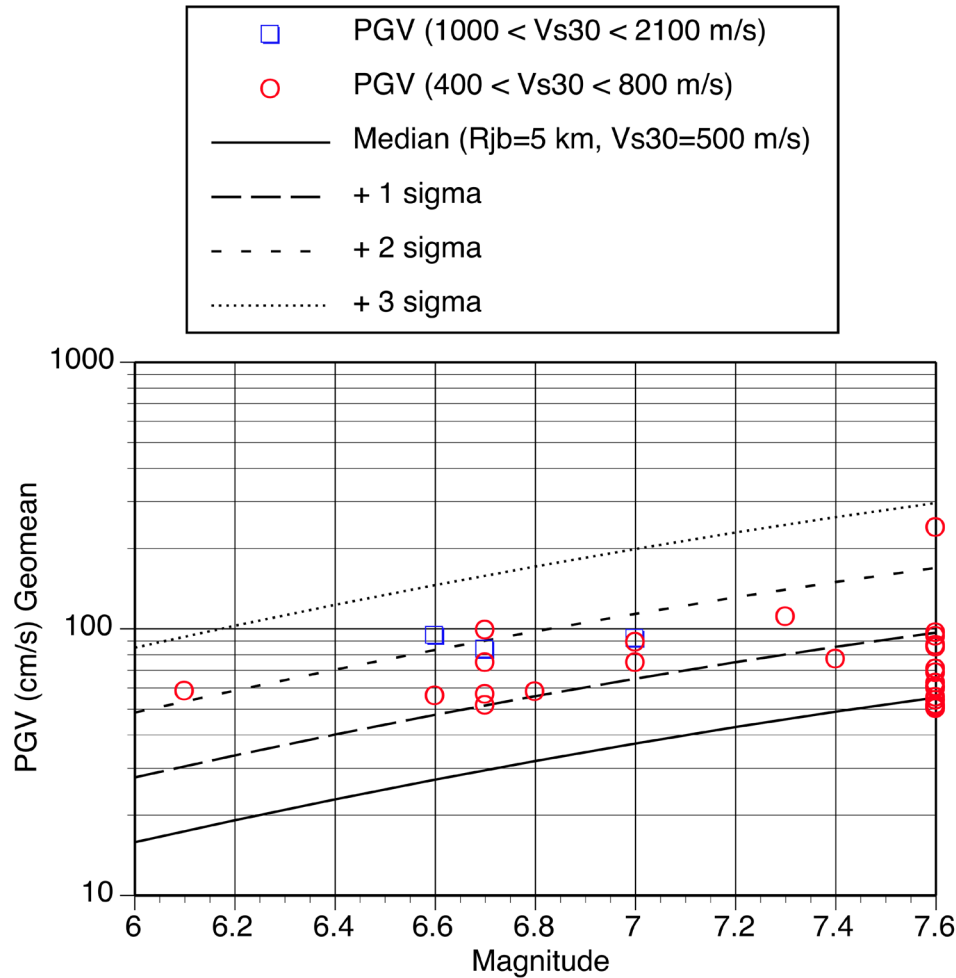
Figure 25. Plot showing geometric mean of the largest Anderson (2010) peak ground velocities (PGVs) as a function of magnitude. $V_{S30} > 800$ m/s is the engineering definition of hard rock, while V_{S30} of 400–800 m/s is regarded as soft rock. The solid and dashed lines denote the magnitude dependence of the median Next Generation Attenuation PGV values and the 1, 2, and 3-sigma with respect to this median at a Joyner-Boore distance of 5 kilometers.

These largest values, essentially outliers for their respective magnitudes, exhibit little dependence on either magnitude or site condition, unlike the median dependences. Figure 25 displays an apparent bound of PGV at ~1 m/s, independent of magnitude. In figure 25, the largest PGV value (at **M**=7.6, the Chi-Chi earthquake) is believed to record the near-field slip velocity of the earthquake rupture, to which we will return shortly. Otherwise, it appears from this plot that geometric-mean PGVs have reached an upper bound of ~1 m/s.

The median PGV calculation at a Joyner-Boore distance of 5 km (the Joyner-Boore distance is defined but not named on p. 2013-2014 of Joyner and Boore, 1981), together with the 1-, 2-, and 3-sigma estimates, reveals, however, that at least for **M**< 7.5, the largest PGV values in Anderson (2010) are in the +1 and +2 sigma range. While it is not possible to calculate pdfs from the Anderson (2010) database, restricted in advance to the 100 largest values, we can do this for the large NGA database (Chiou and others, 2008), and these results are shown in figure 26 in half-magnitude intervals for Joyner-Boore distances ≤15 km.
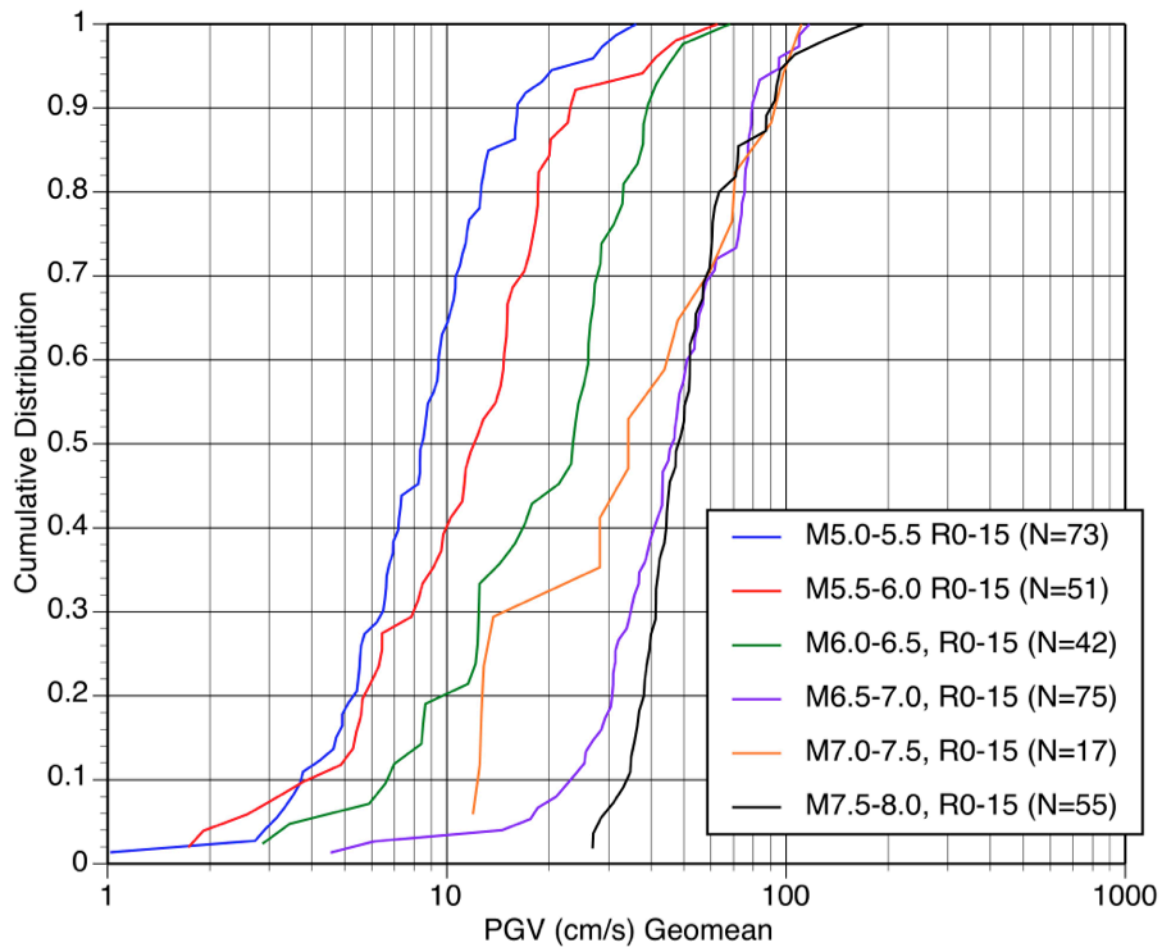
Figure 26. Plot showing cumulative distributions of peak ground velocities in the Next Generation Attenuation database in half-magnitude intervals.

Log PGV is expected to increase as $1/3\log M_0$ (or ½**M**) for far-field observations of constant stress drop earthquakes, but should "saturate" at half the fault-slip velocity in the near-field, that is, for the larger earthquakes at close distances. This "saturation PGV" will depend on the strength of crustal fault zones. McGarr and Fletcher (2007) show that both laboratory results and earthquake observations are consistent with maximum fault-slip velocities of 5 to 6 m/s and PGVs of 2.5 to 3 m/s.

An important feature of figure 26 is the *decrease* in PGV excitation in the 7.0≤**M**≤7.5 interval from the 6.5≤**M**≤ 7.0 interval. While saturation of PGV with increasing **M** for **M**≥7 is expected, a decrease in PGV is not (although this may be due to the small amount of data that contribute to the 7.0≤**M**≤7.5 interval). This interval decrease for 7.0≤**M**≤7.5 is not evident in figure 25 because the model fit to the data was constrained to have PGV monotonically increase with **M**.

Figure 25 suggests that PGVs of 2.5 to 3 m/s would be 3- to 4-sigma removed from the median values, depending on **M**, and also that the largest Chi-Chi PGV is essentially at the limit estimated by McGarr and Fletcher (2007). While the distribution functions in figure 26 permit some constraint on +2 sigma PGVs, they do not allow us to say much about the frequency of occurrence of larger values. Neither, however, does the absence of such values to date permit the truncation of these pdfs at 2 sigma, or even 3 sigma, until a physical limit can be firmly established.

Finally, for the once-every-50,000-to-100,000-year **M**=6.8 earthquake near Yucca Mountain we need the 1-in-a-1,000 or 3-sigma ground motion to reach a hazard level of 10^{-8}/yr. For PGV that we use here, figure 25 shows that this corresponds to a PGV of ~2 m/s. Adjusting this value to Point B, the repository level of Yucca Mountain, puts the 10^{-3} PGV at 1.2–1.3 m/s, in good agreement with the NGA hazard curves shown in figure 14 and in the next section.

Normal-Faulting Surface Displacements

Hecker and others (2010) have compiled determinations of the largest reported vertical displacements (U_{max}) for continental normal-faulting earthquakes with documented surface faulting, for both the historical and paleoearthquake eras. The historical U_{max} data come from 13 earthquakes in the western Cordillera of the U.S. and 79 other global earthquakes. The global historical dataset thus consists of 92 U_{max} estimates. The paleoearthquake dataset comes exclusively from the western Cordillera and includes 175 events, earthquakes that have occurred prior to the historical record but after ~15 ka. The western Cordillera data set, then, includes 188 historical and paleoearthquakes.

For the 92 historical earthquakes, seven events have U_{max} between 5 and 6 m, with none greater than 6 m; three of these earthquakes occurred in the western Cordillera. For the 175 western Cordillera paleoearthquakes, 15 events have U_{max} between 5 and 6 m and two more with U_{max} of 6.1 (eastern Bear Lake fault in Utah) and 6–6.5 m (Bear River fault zone in Utah-Wyoming).

As known from historical ruptures, these U_{max} values typically occupy a small to vanishingly small portion of the total length of rupture, but they also occur in places where the adjoining vertical displacements are a significant fraction of U_{max}. Questions thus arise as to what has been missed. Specifically, have vertical normal-faulting displacements significantly larger than 6–6.5 m actually occurred and not been identified as discrete events or, in the case of the paleoearthquakes, significantly degraded since they occurred?

Hecker and others (2010) address this issue through ratios of U_{max}/U_{mean}, where U_{mean} is the mean vertical displacement, U_{max}/U_{mean} = 2.9 for the historical earthquakes but just 1.6 for the paleoearthquakes, which Hecker and others (2010) attribute to sampling and preservation issues that result in smaller maximum value and a larger mean values for the paleoearthquakes. Hecker and others (2010) go on to conclude that vertical normal-faulting displacements (U_{max}) could be as large as 9 m.

This estimate, while much smaller than the 15 m mean value arising in the Andrews earthquake, nevertheless raises questions as to why nothing has been observed for U_{max} between 6.5 and 9 m. But for extreme ground motions, we are not especially concerned with fault-displacement values that occupy such small fractions of the fault length/plane. Of more interest is U_{mean}, which seems to be ≤4 m for both the historical and paleoearthquakes compiled by Hecker and others (2010). This value is still larger than for any paleoearthquake examined in the Yucca Mountain studies and is 50 percent larger than the 2.7 m estimated for the 77-ka earthquake that ruptured the Solitario Canyon Fault, presumably because of the shorter fault lengths in the Yucca Mountain area.

In the context of PSHA, we would like, ideally, to have a set U_{max} for a number of earthquakes with known magnitudes. Upon removing the average magnitude dependence of U_{max} on **M**, we could then compute the distribution of residuals and determine the shape of the upper tail in the case of extreme ground motions. This distribution could be used then to check or constrain the distribution of faulting displacements arising from numerical simulations of the source process.

Unfortunately, most of what is known about magnitudes of paleoearthquakes is derived from the same fault-displacement data, providing no independent estimate of magnitude for the paleoearthquakes. An alternative route would be to develop a relationship between fault displacement and surface rupture length for the paleoearthquakes, as have Hecker and others (2010, fig. 9). There is,

however, much variability in the results: faults with lengths of just 20–30 km, typical of fault lengths in the Yucca Mountain area, can still have faulting displacements of 5 to 6 m, considerably larger than any single-event displacements known for the Yucca Mountain faults.

m_b-M Stress Drops for Continental Crustal Earthquakes

Body-wave magnitude (m_b) and surface-wave magnitude (M_S) pairs were the first successful discriminant of underground nuclear explosions (UNE) from naturally occurring crustal earthquakes. Radiating most of their seismically observable energy as impulsive, compressional P-waves, UNEs typically have noticeably larger m_b than for crustal earthquakes of the same M_S (since about 1980 moment magnitude (**M**) has been used instead of M_S). With the completion of the World Wide Standardized Seismograph Network (WWSSN) in the early 1960s, uniform, global seismic recording of earthquakes and explosions became possible down to **M**~4.5. Since then, m_b-**M** pairs have been determined for more than 10,000 crustal earthquakes.

In principle, m_b-**M** data carry information about relative earthquake stress drops; for two crustal earthquake of the same **M**, the one with the higher m_b will have the higher stress drop. Obtaining absolute stress drops, however, requires the application of a ground-motion model and its assumptions. The point-source, finite-duration, Gaussian white noise representation for far-field ground accelerations (Hanks and McGuire, 1981; Boore, 1983, 2003), more briefly known as the stochastic model, is the basis for the model calculations in figures 27 and 28, as formulated most recently in the SMSIM code (Boore, 2005). The calculations in figures 27 and 28 also employ techniques for applications to teleseismic recordings described in Boore (1986). Because the body-wave magnitude scale is relative, the calculations of absolute stress drop require the "pinning" of a selected stress drop to a selected m_b-**M** pair, 65 bars at m_b=5.71 and **M**=6.0 for these results. The resulting stress drops shown in the figures are most closely related to the a_{rms} (root-mean-square acceleration) stress drops of Hanks and McGuire (1981).

Figure 27 shows m_b-**M** data for 3,374 earthquakes of all mechanism types occurring in continental crust; the number of events represented by any symbol is color-coded logarithmically. None of these earthquakes have m_b>7, the predicted saturation level of m_b for constant stress-drop earthquakes (Hanks, 1979). There is considerable variability of stress drop as estimated here (more below), a factor of ten or more at any **M**; this is true, however, for all measures of earthquake stress drop. The very large stress drops and compression of the constant stress-drop curves on the left-hand side of the plot reflects the instability of the inversion of m_b to a_{rms} stress drop at m_b~5½ and smaller, as the earthquake corner frequency passes through the m_b bandwidth; at smaller magnitudes both m_b and **M** measure only seismic moment.

Only normal-faulting events (N=774) are shown in figure 28; the number of events represented by any symbol is also color-coded logarithmically, but not so strongly as in figure 27. The stress-drop variability is somewhat less in figure 28 than in figure 27, but so is the number of events. Both figure 27 and 28 indicate an increase in stress drop for m_b=**M**≤5½, but no dependence of stress drop on magnitude for **M**≥5½. There is no discernible difference between figure 27 and 28 in terms of the median m_b-**M** trend.

Compared to the number of **M**≥5 earthquakes recorded by local strong-motion instrumentation, the number of **M**≥5 earthquakes recorded teleseismically is huge, as evidenced by the m_b-**M** graphics above. Unfortunately, the number of normal-faulting earthquakes in both datasets constitutes a small fraction of the number of events. The strong-motion earthquake set is not large enough to assure us that it is representative of all crustal earthquakes, especially normal-faulting events, nor is it large enough to reach to 3-sigma stress drops (for which ~1000 events would be necessary).

The teleseismic data set, however, is large enough, although we are yet unsure about what to do with those earthquakes for which the inversion of m_b to a_{rms} stress drop approaches instability, where the lines of constant a_{rms} stress drop converge. Figures 27 and 28 both include well known earthquakes for which m_b and **M** are well determined, and independent determinations of the a_{rms} stress drop for these events would serve to calibrate/corroborate the a_{rms} values given in figures 27 and 28.
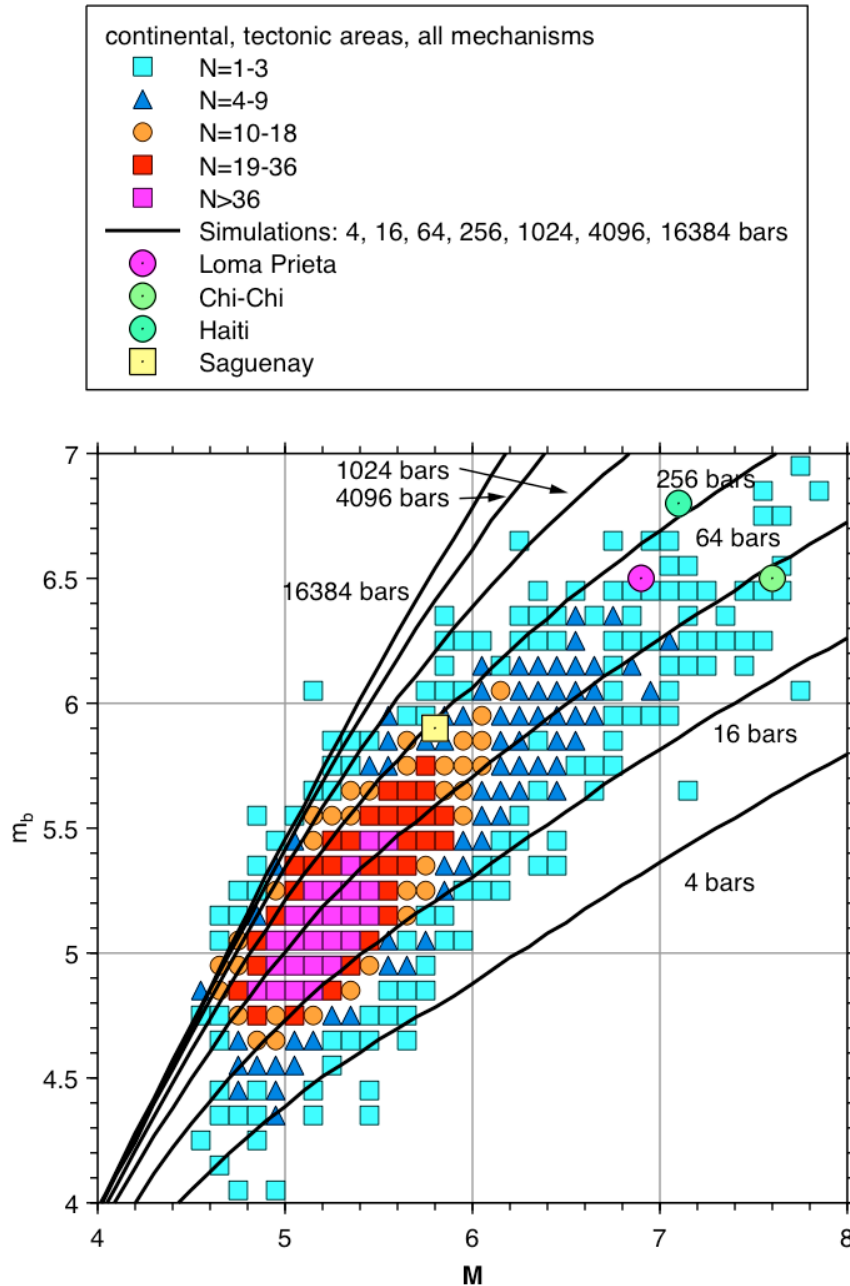
Figure 27. Plot showing pairs of body-wave magnitude (m_b) and moment magnitude (**M**) for 3,374 continental crustal earthquakes of all mechanism types with a_{rms} stress-drop contours, from Boore (2005). Four specific earthquakes are identified in this data-density plot.
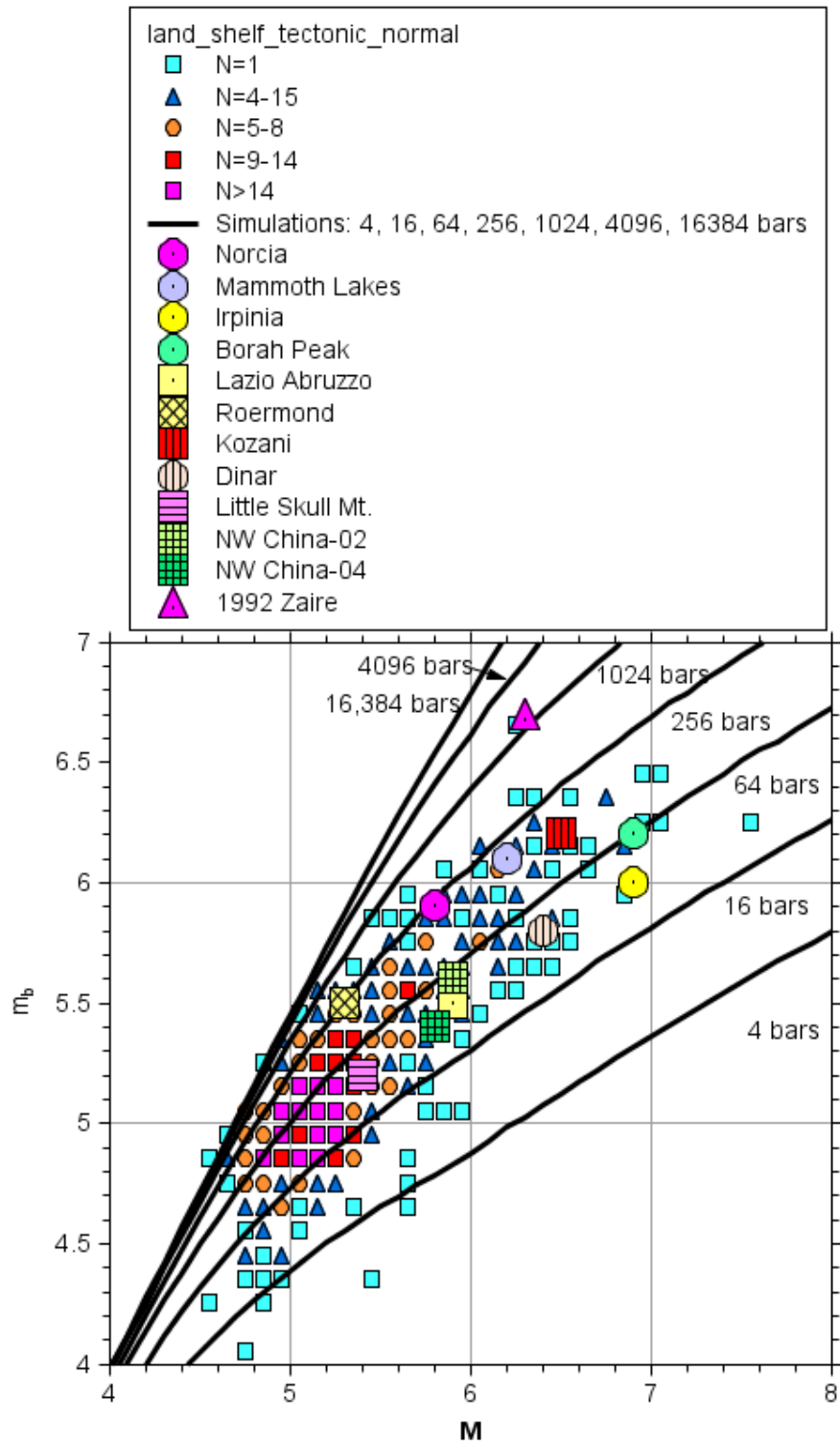
Figure 28. Plot showing pairs of body-wave magnitude (m_b) and moment magnitude (**M**) for 774 normal-faulting events with a_{rms} stress-drop contours, from Boore (2005). Twelve specific earthquakes are identified in this data-density plot.

In the meantime, we simply sidestep this matter by examining the a_{rms} stress drop distribution for $m_b=\mathbf{M}\geq 6$ (fig. 29). This figure shows 441 a_{rms} stress drops divided by the mean value of 65 bars; one sigma corresponds to a factor close to 2. This mean value and one sigma are in accord with the early findings of Hanks and McGuire (1981) and Boore (1983). Figure 29 also shows (again) that there is no basis for truncating this a_{rms} stress drop distribution at its high end, 2<sigma< 3.

In a study not part of the ExGM research program, Allman and Shearer (2009) determined spectral estimates of stress drops for 1,759 crustal earthquakes with moment magnitudes between 5.3 and 8.3 from teleseismic P-waves. With the exception of some very high stress drops likely due to analytical instabilities at the smaller magnitudes (5.3≤$\mathbf{M}$≤ 6.0), these earthquake stress drops occupy the same range of spectrally determined stress drops found by many other investigators (fig. 8 of Allman and Shearer, 2009) dating back to Thatcher and Hanks (1973) and Hanks (1977).

For each fault type the log stress values were adjusted so that they have a mean of log 65 bars when averaged over all events (not just $\mathbf{M} \geq 6.0$). The mean-adjusted log stress values for the three fault types were then combined for this plot, giving 441 events.
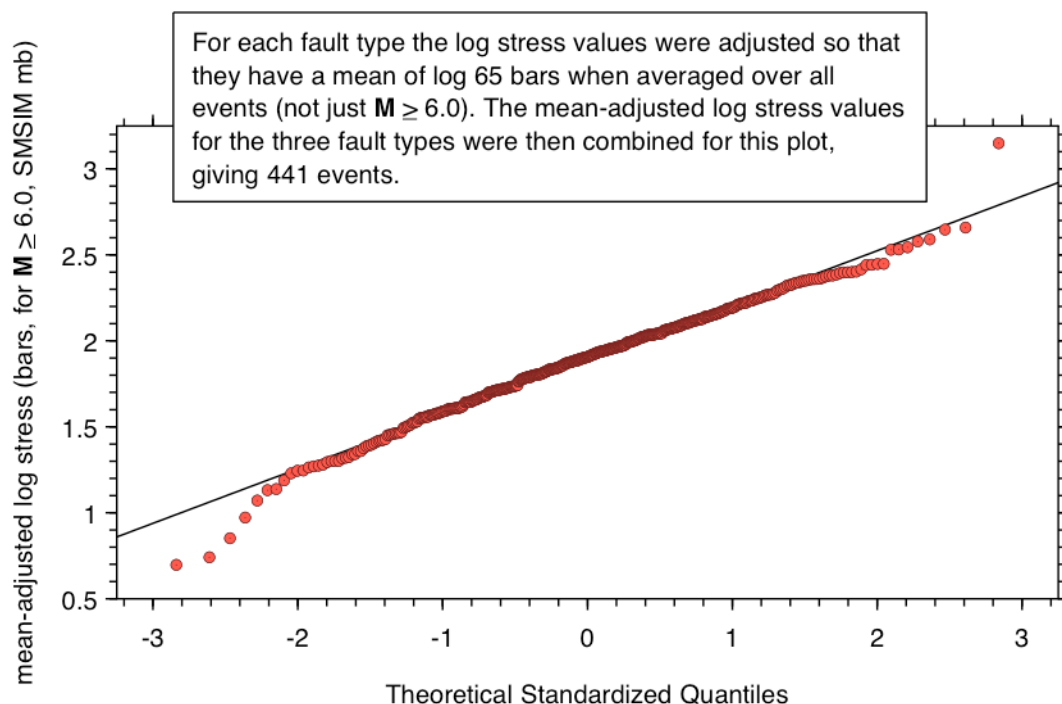
Figure 29. Plot of cumulative distribution function of mean-adjusted (to 65 bars) $\log a_{rms}$ stress drops. The event in the upper right is the $\mathbf{M}$=6.3, m_b=6.7 Zaire earthquake (Sept. 11, 1992) with an a_{rms} stress drop in excess of 1000 bars (fig. 28).

Magnitude-Dependent Apparent Stress?

The excitation of high-frequency (f≥1–2 Hz) strong ground motion by moderate-to-large ($\mathbf{M}$≥6) crustal earthquakes depends mostly on the stress differences accompanying faulting displacements. It has been known since the 1970s that crustal earthquake stress drops ($\Delta\sigma$) do not depend on the size or seismic moment of the earthquake, from the smallest earthquakes we can observe to the largest we know of. It is this feature of crustal earthquakes that allows ground-motion prediction (GMP) models, whether theoretical or empirical, to work so well and be so consistent with one another. At any $\mathbf{M}$, however, a considerable variability in $\Delta\sigma$ exists, which contributes to the aleatory variability of the ground-motion data of any GMP model.

The apparent stress is the product of the shear modulus times the ratio of radiated energy divided by seismic moment (the scaled energy), an earthquake source parameter that is closely allied with $\Delta\sigma$, at least for ω^{-2} far-field source models, for example, that of Brune (1970, 1971); for these source models, the apparent stress differs from $\Delta\sigma$ by only a constant. It was a surprising result, then, when Mayeda and Walter (1996) reported that the apparent stress of earthquakes in the western U.S. increased by a factor of ten from **M**~4 to **M**~7, but one that was mostly ignored by scientists and engineers interested in GMP. When Mayeda and Walter (1996) combined their data with smaller events recorded at depth in the Cajon Pass borehole (Abercrombie, 1993), they found that the apparent stress increased from 0.3 MPa at **M**~1 to 30 MPa at **M**~7. Such an increase in apparent stress for constant stress drop earthquakes can only come from $\omega^{-\gamma}$ source models with $\gamma<2$. For $\gamma\leq1.5$, the energy integral is unbounded.

Because the significance of these results for GMP is huge, because independent, teleseismic estimates of radiated energy for the eight largest earthquakes were ten times less than those reported by Mayeda and Walter (1996), and because the Mayeda and Walter (1996) analysis was based on a novel approach of coda envelopes, the Mayeda and Walter (1996) methodology and results were revisited by Baltay and others (2010). The latter study found no dependence of apparent stress on earthquake size, from magnitude 3.0 to 7.1, for more than 200 events in four earthquake sequences in western North America (fig. 30*A*). Combining these results with the earlier findings of Ide and Beroza (2001) reveals that apparent stress does not depend on M_0 over 9+ orders of magnitude (fig.30*B*), although the variability at any M_0 can be considerable.

Baltay and others (2010) employ empirical Green's functions in a more direct and transparent manner than do Mayeda and Walter (1996), without the intermediate step of constructing coda envelopes, and consistently find that their corrected, high-frequency source spectra are close to the ω^{-2} model. For reasons not yet understood, Mayeda and Walter (1996) apparently have progressively overcorrected the high-frequency source spectra (to $\gamma<2$) of the earthquakes they analyzed such that their eight largest earthquakes have radiated energies ten times greater than the teleseismic estimates. This does not constitute proof of right or wrong, and probably points more directly to the intrinsic difficulties in reliably estimating the radiated energies of earthquakes. In the meantime, however, we concur with Baltay and others (2010) that there is no reason to abandon constant stress-drop scaling for the estimation of high-frequency strong ground motion.
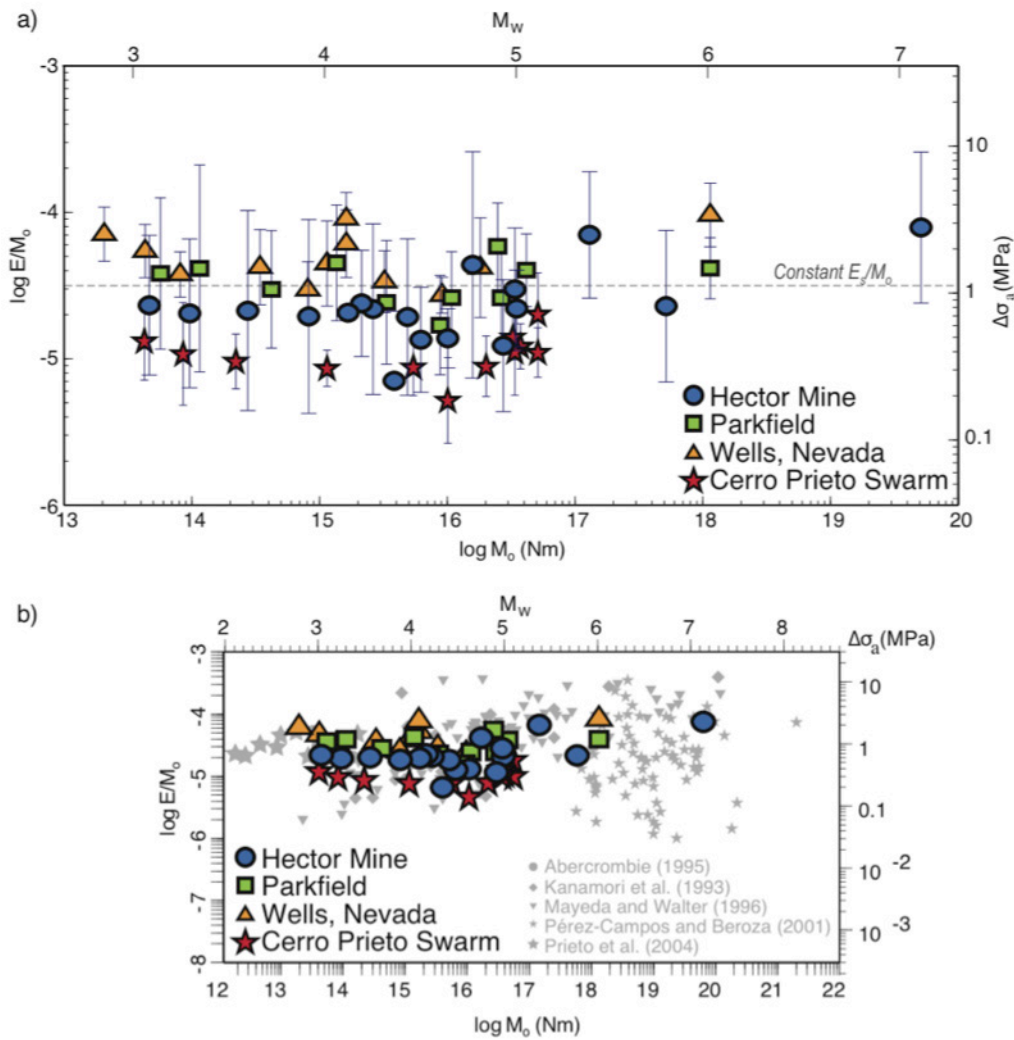
Figure 30. *A*, Plot of scaled energy E_S/M_0, which is proportional to apparent stress, as a function of M_0 for the Hector Mine, Parkfield, Cerro Prieto Swarm, and Wells, Nevada earthquake sequences analyzed by Baltay and others (2010). Grey bars indicate the 95 percent intraevent, interstation scatter of the scaled energy estimates. *B,*The data in (*A*) superimposed on the earlier results of Ide and Beroza (2001).

Points in Hazard Space

In this section, we revisit the points in hazard space (PiHS) graphic presented in figure 14, which summarizes some but certainly not all of the ExGM research along its three basic themes: physical limits to earthquake ground motions, unexceeded ground motions (UGM), and frequency of occurrence of ground motion amplitudes or the things that cause them. We include in this section more descriptive explanation of how the observations and results developed in ExGM appear in the PiHS graphic; we also develop some simplified hazard calculations to illustrate some basic points, and improved estimates of failure probabilities of fragile geologic structures, specifically the lithophysal units and PBRs. All hazard estimates are calculated for PGV at Point B (Stepp and others, 2001), the reference rock site at the repository horizon. When necessary, PGV at Point A is corrected to Point B by a factor of 1/1.2.

The framework for PiHS is the 1998 Yucca Mountain PSHA for PGV. This is shown for Point A in figure 4 and for Point B in figure 14. Point A is the hypothetical, reference rock outcrop (shear-wave velocity of 1,900 m/s) chosen at an early time in the PSHA study when the near-surface site-response studies were not complete. Point B is at the repository horizon, at depth in the mountain, where the lithophysal units are. Point C is on the surface of Yucca Mountain, above the repository. The locations of these points are shown diagrammatically in figure 2 of Stepp and others (2001).

The shear-wave velocity on the surface for hard rock (Point A) is 20 percent larger than at the repository depth (Point B). The shear-wave velocity at the surface on the tuffs where the rocks are located (Point C) is less than the hard-rock velocity. Using the V_{S30} scaling in the NGA models, the Point A PGV is will be 0.7 times the point C PGV. Combining these two factors, the total scaling for PGV from Point C to Point B is a factor of 0.6; $PGV_B = 0.6 \ PGV_C$.

Simplified Hazard Models

Hazard models illustrate the significant effect the NGA PGV database and the new NGA relations (Power and others, 2008) have on the seismic hazard at Yucca Mountain—or any other rock site close to faults that generate significant earthquakes relative to the ~1995-vintage ground-motion prediction equations (GMPE) employed in the 1998 Yucca Mountain PSHA. Instrumental recording networks have expanded significantly in the past 15 years, especially in Japan, and the 1999 earthquakes in Turkey, California, and Taiwan, and the 2002 Denali, Alaska, earthquake have added much new data for large ($\mathbf{M}$>7) earthquakes at close distances.

The 1998 Yucca Mountain PSHA involved a very complicated SSC, which makes it hard to use and also obscures the essential fact that the rate of seismicity near Yucca Mountain is very low, as we have already seen. Our first simplified model, then, is very simple, including only the larger events ($\mathbf{M}{\geq}6.3$) that occur on the nearby, block-bounding faults of Yucca Mountain—the Paintbrush Canyon-Stagecoach Road and the Solitario Canyon Faults. We also assume from the paleoseismic studies that these $\mathbf{M}{\geq}6.3$ events occur on average, on one fault or the other, once every 30,000 years. Then we order the PGV values from the NGA dataset for earthquakes with $6.3{\leq}\mathbf{M}{\leq}7.3$ and distances less than 15 km (N=125) from smallest to largest to characterize the ground motion associated with our chosen earthquakes. Only a few of these PGV values are from rock sites, and most of these strong motion data are from soil sites. As such, we first adjust them to a Point C V_{S30}=800 m/s and then from Point C (Yucca Mountain free-surface) to point B (repository depth) using the Point C-to-Point B scale factor of 0.6. The resulting complementary cumulative distribution of PGV values is shown in figure 31. Using the median (0.125 m/s) and (logarithmic) standard deviation (0.70) of this distribution allows us to construct the smooth blue curve in figure 31 and multiplying that by the rate of one $\mathbf{M}{\geq}6.3$ earthquake every 30,000 years yields the orange dashed-line hazard curve in figure 32. We call this hazard model the S1 Model, and it represents only a small fraction of the seismic hazard that was calculated for Yucca Mountain in the 1998 report.

The second simplified hazard model is based on just one of the six SSC models used in the 1998 Yucca Mountain PSHA, the Doser/Fridrich/Swan (DFS) model. We chose this model because it is nearly identical to the median values of the six SSC models. For the GMC we used the median values of the four newer 2008 NGA PGV models based on much larger data sets than were available in the mid-1990s.
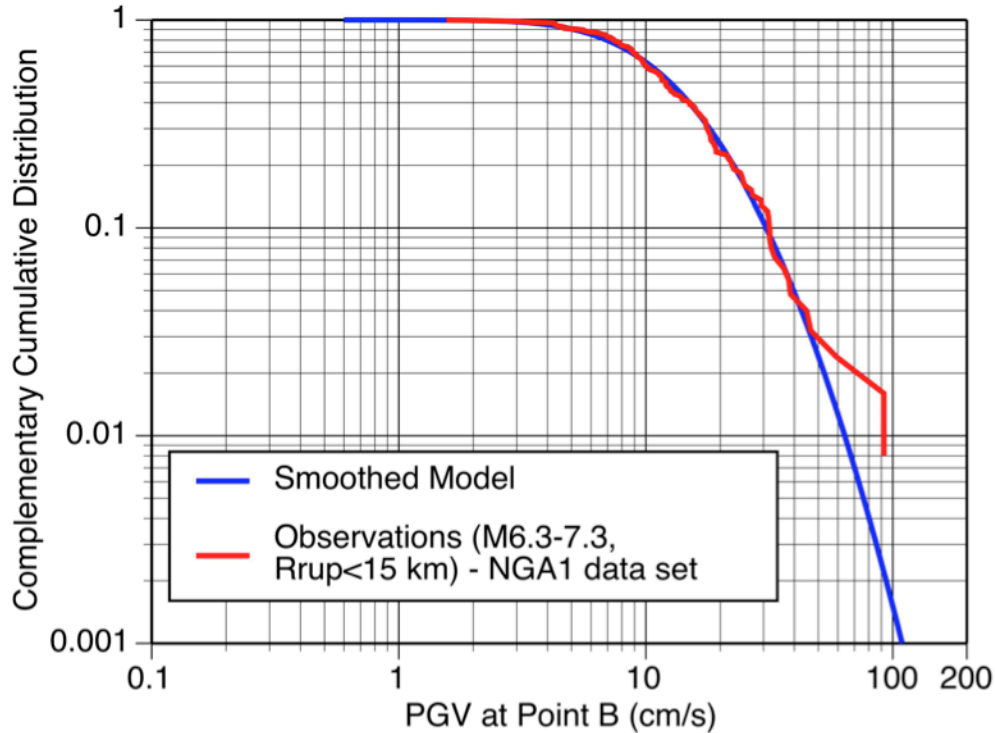
Figure 31. Plot showing complementary cumulative distribution of 125 peak ground velocity values 6.3≤**M**≤7.3 and R≤15 km from data developed as part of the first Next Generation of Attenuation project, corrected to point B. Data are shown in red; the smoothed model (blue) is used in the simplified hazard calculation (orange dashed line) shown in figure 32.

This hazard model (the S2 Model) is shown as the red dashed curve in figure 32. Anderson and others (2007), using the same NGA GMC but with a completely independent, simplified SSC model, arrived at a similar hazard curve.

      Also shown in figure 32 are the mean (blue) and various fractile (black) hazard curves for the 1998 Yucca Mountain PSHA. The S2 Model, using the median NGA PGV values, should only be compared to the 50 percentile 1998 curve, because no epistemic uncertainty has been figured into the S2 Model. The S2 Model (red-dashed curve in figure 32) here has more **M**~6 earthquakes than does the S1 Model, providing for more PGVs of 10–20 cm/s, which is why the red dashed curve sits above the orange-dashed curve at small PGV (less than approximately 20 cm/s). Both of these simplified hazard models sit well below the median hazard curve from the 1998 PSHA, suggesting that GMC uncertainties played an important role in the 1998 Yucca Mountain PSHA.
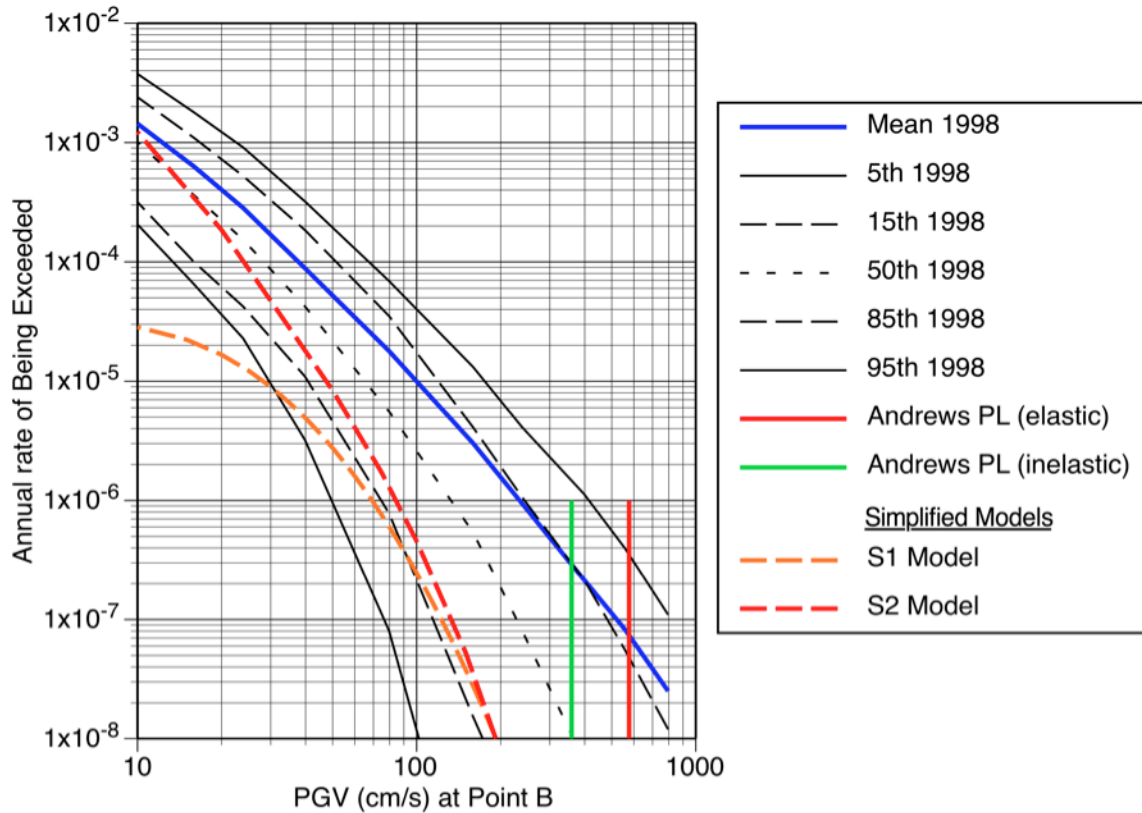
Figure 32. Plot showing the mean and fractile hazard curves from the 1998 Probabilistic Seismic Hazard Analysis for Yucca Mountain compared to the two simplified model hazard curves and the physical limits.

Physical Limits

Physical limits to earthquake ground motion are the largest ground motions that can possibly occur. Physical limits appear as vertical lines in PiHS because there is zero probability that larger ground motions can occur at the site of interest. Physical limits permit rejection of combinations of the ground motion median, standard deviation, and form of the upper tail of the distribution of the ground motion models that lead to ground-motions above the limits (fig. 33). Figure 32 shows the physical limits of PGV at Point B from Andrews and others (2007) for the elastic and inelastic cases.

The PGVs for the mean hazard curve and 85th fractile hazard curve at hazard levels smaller than 3×10^{-7}/yr are beyond the PGV corresponding to the inelastic physical limit, meaning that the these hazard curves are inconsistent with the inelastic physical limit. The PGVs for the 50th fractile curve are below the physical limit of PGV for hazard levels down to 10^{-8}/yr, indicating that half of the ground motion models considered are consistent with the physical limit.

Uncertainties in these physical limits are difficult to estimate, although it is safe to assume that the elastic limit is a true upper bound to the inelastic limit. These limits are subject to uncertainties in the initial stress state, the dynamic friction once slip begins, geologic structure, and the nature and strength of inelastic yielding/energy dissipation.
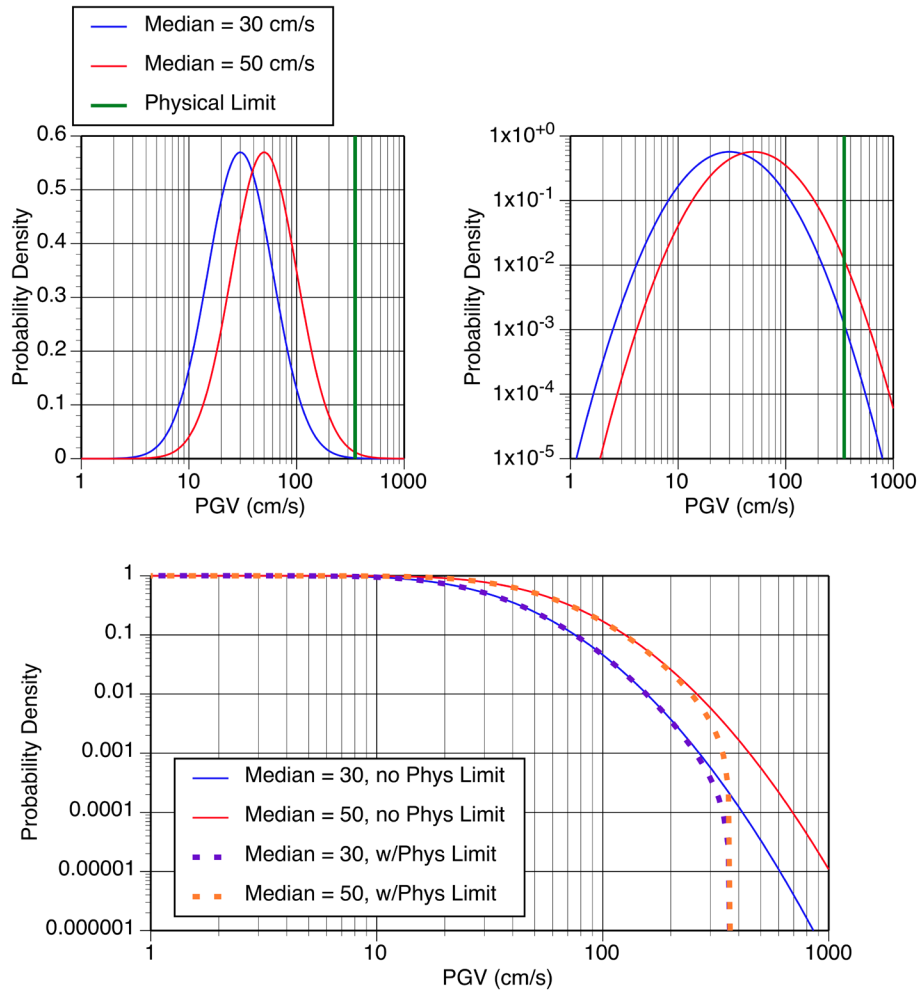
Figure 33. The top panel shows plots of probability distribution functions for peak ground velocity (PGV) using two different models with median values of 30 and 50 cm/s and arithmetic (left) and logarithmic (right) ordinates. The green line in both graphs is a physical limit of PGV=3.5 m/s, which leads to truncation of the hazard curves shown in the bottom panel. Physical limits typically impact only the lowest probability ground motions.

Unexceeded Ground Motions

Unexceeded ground motions (UGM) are ground motions strong enough to drive a fragile geologic structure (FGS) to failure but which have not occurred during the time period for which the FGS has indeed been fragile (the fragility age). Representation of a UGM in hazard space requires a ground-motion value for the abscissa and the appropriate hazard level for the ordinate. Two classes of UGM are of interest to us with respect to Yucca Mountain: the undamaged lithophysal units at the repository level and the PBRs on the west face of Yucca Mountain.

Early versions of the PiHS graphic (for example, in Abrahamson and Hanks, 2008) used simple methods to plot UGM: the ground-motion value (x-axis) was the PGV with a 95 percent chance of causing failure of the FGS. For the rate of exceedance (y-axis), we used the inverse of the age of the FGS. This simplified approach was used as a rough check of the consistency of the UGMs and the hazard curves; here, we develop a more rigorous, probabilistic approach.

Specifically, we calculate below the probability that some FGS has not failed in T years. The analysis below assumes that fragility depends on a scalar ground motion (PGV), but the approach can be generalized to fragilities that depend on vector ground motions. The probability that a geologic structure, G, did not fail in T years is given by:

$$P(G_{not\,failed}) = [1 - P_{annual}(G_{fails})]^T \tag{1}$$

where T is the FGS fragility age, and $P_{annual}(G_{fails})$ is the annual probability that G does fail. $P_{annual}(G_{fails})$ is the sum of the products of the rate of occurrence of ground motion and the conditional probability of failure, given the ground motion. The annual hazard curve $v(z)$ gives the rate of exceedance of scalar ground motion z, and its derivative with respect to z gives the rate of occurrence of z. The annual probability of failure is then given by:

$$P_{annual}(G_{fails}) = \int \frac{dv(z)}{dz} P(G_{fails}\,|\,z)dz = \sum_{i=2}^{N_Z} [v(z_{i-1}) - v(z_i)] P(G_{fails}\,|\,z = \frac{z_{i-1} + z_i}{2}) \tag{2}$$

where $P(G_{fails}\,|\,z)$ describes the FGS "fragility."

Figure 34 illustrates graphically what was said above. In figure 34, the uppermost plot (a) is an annual hazard curve with respect to PGV, with its (numerical) derivative beneath it showing the annual rate of occurrence of PGV (b). The fragility $P(G_{fails}\,|\,z)$ is shown in (c). As shown by the converging arrows, the product of the rate of occurrence and the fragility (d) provides the integrand of equation (2), the incremental contribution of each PGV to the total failure probability of our fragile geologic structure. Performing the indicated numerical integrations yields the annual probability of failure, 4.5 x 10^{-6}/yr in this case, and also the cumulative contribution of all PGVs to failure, the graph in the lower left (e). The median PGV contributing to failure, Z_1, is taken as the UGM for this particular fragile geologic structure.

The relation between Z_1 and the fragility curve depends on the slope of the hazard curve and the slope of the fragility curve. Typically, Z_1 is lower than the ground motion at the 50 percent failure probability because there are so many more small earthquakes with smaller ground motions; even though the fragility is low, the rate of the smaller PGVs is much higher than the rate of ground motion corresponding to the 50 percent failure probability level. If the fragility curve is steep (for example, if the fragile geologic structure is brittle), then the Z_1 value will be close to the value that leads to a 50 percent chance of failure, because the fragility for the lower ground-motion values will be very small, offsetting the higher rate of occurrence of the smaller ground motion values.
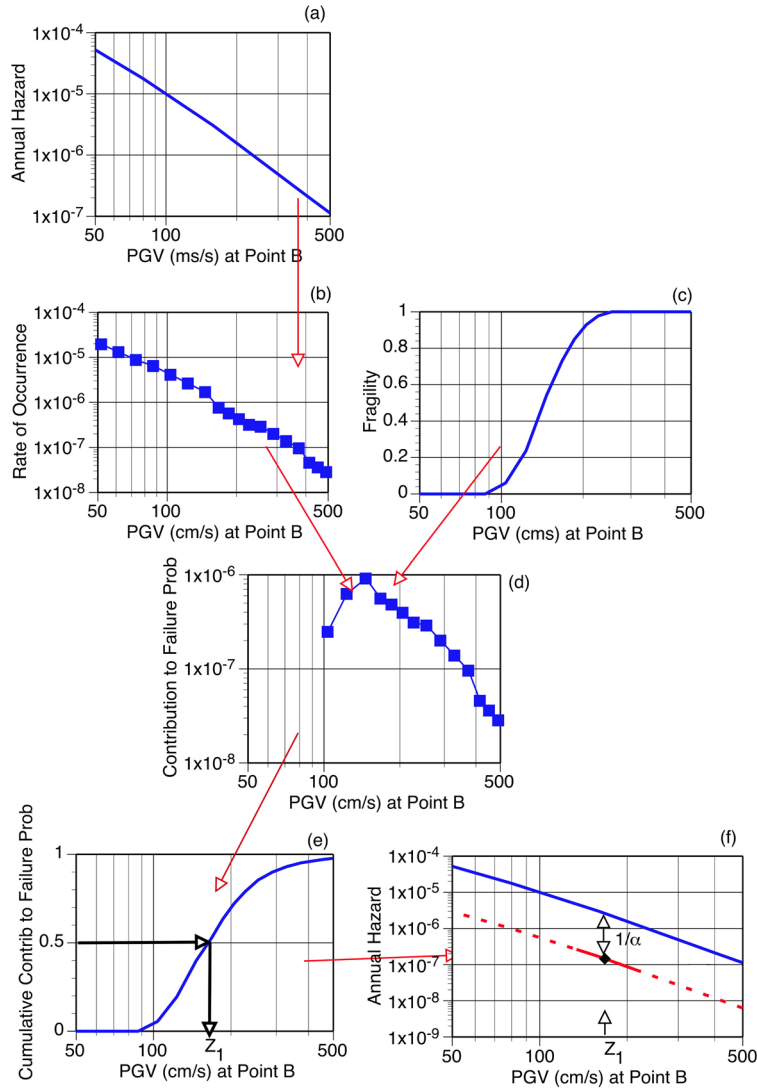
Figure 34. Illustration of the steps to determine the point in hazard space for the unexceeded ground motion of a fragile geologic structure.

What is the appropriate hazard level for Z_1? The approach we use here is to determine the scale factor, α, to be applied to the hazard curve that would lead to a specified probability, P_1, for which our structure does not fail during the time it has been fragile. For a structure that has been fragile for T years, P_1 is

$$P_1 = [1 - \alpha_{P_1} P_{annual}(G_{fails})]^T \tag{3}$$

and α is

$$\alpha_{P_1} = \frac{1 - P_1^{1/T}}{P_{annual}(G_{fails})} \tag{4}$$

If we are interested in the hazard curve that would lead to a 5 percent probability of the FGS not failing, for example, α is

$$\alpha_{0.05} = \frac{1 - 0.05^{1/T}}{P_{annual}(G_{fails})}$$
(5)

For the hazard and fragility curves shown in figure 34, $P_{annual}(G_{fails})$=4.5 x 10^{-6}/yr. For an age of 12 million years for the lithophysal units, then, $\alpha_{0.05}$=1/18, with which we scale the hazard curve. The lower right frame (*F*) of figure 34 shows the scaled hazard curve as a dashed line; for the range of ground motions that contribute to the probability of failure, this scaled hazard curve is the hazard curve that has a 5 percent chance of not failing the fragile geologic feature. That is, if the computed hazard is above this scaled hazard, then there is less than 5 percent chance that the geologic structure would have survived in its existing state of fragility for *T* years.

The 50th percentile cumulative failure probability point on the scaled hazard curve fixed by Z_1 (fig.34*E*) is the PGV most strongly constrained by the fragile geologic structure. The solid red segment of the scaled hazard curve shows the range of PGV that covers the 25–75 percent range of the failure probability of the geologic structure (fig. 34*F*), revealing that the fragile geologic structure constrains only part of the hazard curve—hence the expression "points in hazard space."

Any point in hazard space (PiHS) for an FGS depends on the slope of the hazard curve as well as the fragility. The absolute level of the hazard curve does not affect the PiHS. If two hazard curves have the same shape other than a multiplicative factor, Z_1 is unchanged (as it is based on the normalized contribution to failure) and α simply adjusts for the new hazard curve level.
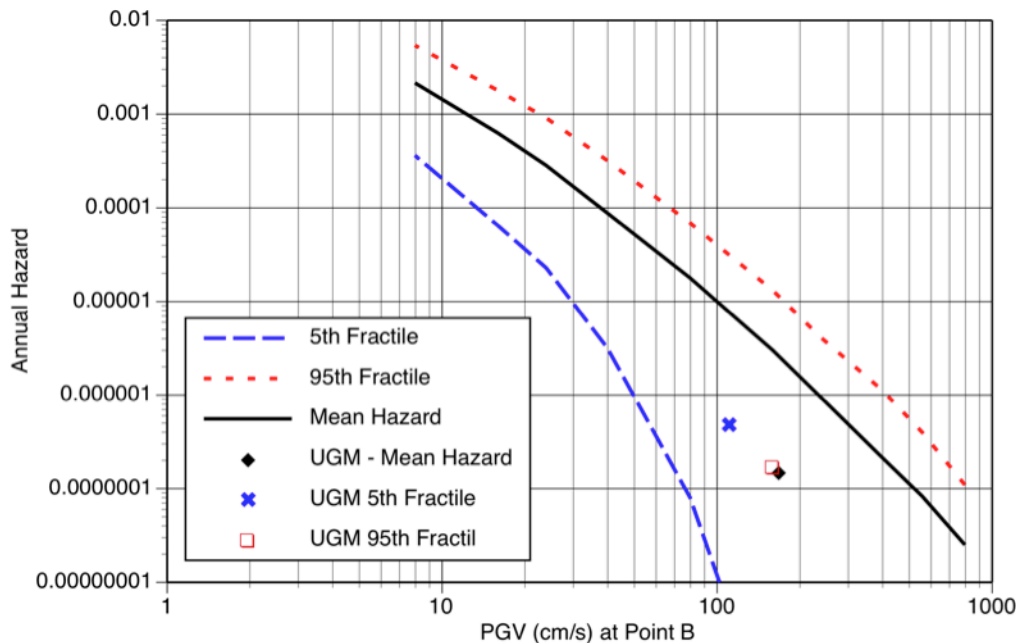
Figure 35. Graph showing the effect of different slopes of the hazard curves on the unexceeded ground motions.

As an example of the dependence of the UGM point on the hazard curve, the PiHS is shown for three different PGV hazard curves in figure 35: mean, 95th fractile, and 5th fractile. For the mean and

95th fractile hazard curves, the shapes are similar, and there is almost no change in the location of the PiHS. For the 5th fractile, the slope becomes much steeper, and Z_1 becomes smaller because there are relatively fewer large PGVs. The PiHS based on the 5th fractile hazard is shifted up and to the left. It falls along the trend of the hazard curves so it still provides a consistent evaluation of the hazard curve. Note the 5th fractile hazard curve lies below the UGM points, meaning that with respect to it, there is more than a 5 percent chance of the FGS surviving.

Lithophysal Fragilities

The undamaged lithophysal units were recognized by the Yucca Mountain Project (YMP) as an important constraint on the 1998 PSHA, especially for constraining the probabilities of exceedance for PGV. To recapitulate briefly, lithophysae are cavities that form in volcanic rocks as the result of exsolving gases as the volcanic rocks cool. In the case of the lithophysal units in the repository block of Yucca Mountain, these cavities can occupy ~20 percent of the rock volume and thus weaken the rock considerably. The great antiquity of the undamaged lithophysae thus speaks to ground motions that have not occurred since these lithophysae cooled ~12.8 Ma.

As described in some detail in appendix III, itself a synopsis of BSC (2005), elastic properties, compressive strength, and failure strains were determined by laboratory testing for large samples (up to 288 mm in diameter) of the lithophysal units. Failure strains are plotted as a function of porosity in figure 5 of appendix III. These data were used to estimate the "threshold shear strain" that would result in geologically observable damage to the lithophysal units; a pdf of these threshold shear strains is shown in figure 6 of appendix III. Geologically observable damage would begin to appear at 0.1 percent strain; massive damage to the lithophysal units would occur at 0.25 percent strain.

Two alternative models relating strain and PGV were then estimated from the site response studies, one (UMT) being based on more linear material response to incoming ground motion and the other (LMT) based on more non-linear behavior. With these intermediate steps, the fragilities based on the threshold shear strain were converted to fragilities based on PGV for both the UMT and LMT properties, and they are shown in figure 36.
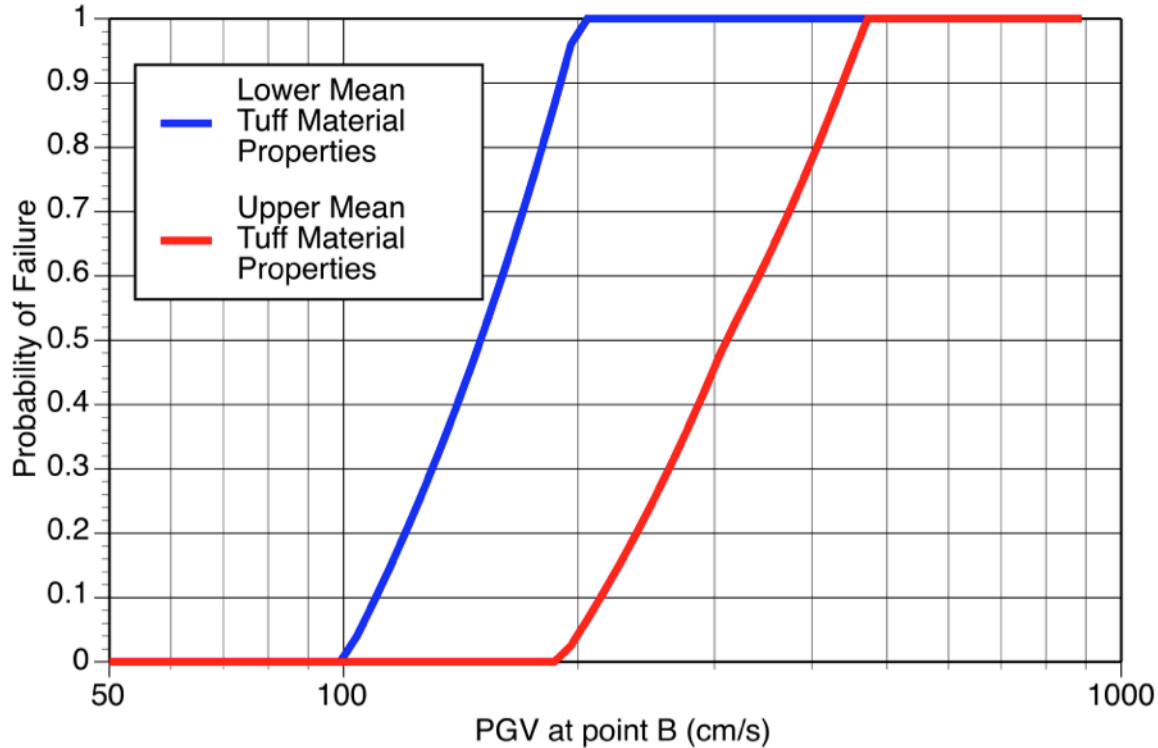
Figure 36. Plot of peak ground velocity fragilities for the lithophysal units as expressed by the properties of the Upper Mean Tuff and Lower Mean Tuff.

PBR Fragilities

Earlier in this report, we recounted how Purvance and others (2009) determined toppling probabilities for five precarious rocks and four stacks, as a function of *both* PGA *and* PGV (or more precisely, PGA and PGV/PGA). Results were shown in figure 21 and indicated that smaller PGAs require larger PGVs to maintain a fixed probability of failure. This causes a difficulty for the PiHS computation, however, as we have hazard curves that tell us the rates of occurrence of a given PGA or PGV individually, but do not provide information about the rate of jointly observing a given PGA *and* a given PGV in a single ground motion. In the end, we need to express these toppling probabilities in our PiHS format that is a function of PGV alone.

To begin, we first convert the pairs of PGA and PGV/PGA values calculated by Purvance and others (2009) into pairs of PGV and PGA/PGV values, with PGV as the abscissa as in PiHS; this conversion is illustrated in the top two plots of figure 37. The top left figure shows the original toppling probabilities in terms of PGA and PGV/PGA. The top right figure shows the same information in terms of PGV and PGA/PGV. Each coordinate in the top left figure has some corresponding coordinate in the top right figure, and the two corresponding coordinates have identical toppling probabilities. For a given PGV value, the top right figure now provides failure probabilities as a function of PGA/PGV; an example of this is shown in the lower left figure, for PGV=30 cm/s.

Earthquake seismologists will know that PGV has a strong magnitude-dependence (for example, McGarr and Fletcher, 2007) and so does PGA/PGV, although less strong as we shall see shortly, and both have distribution functions about the median magnitude dependence. The lower right panel of figure 37 shows the pdf for PGA/PGV at **M**=6, described in more detail below. All of this complicates the analysis here.
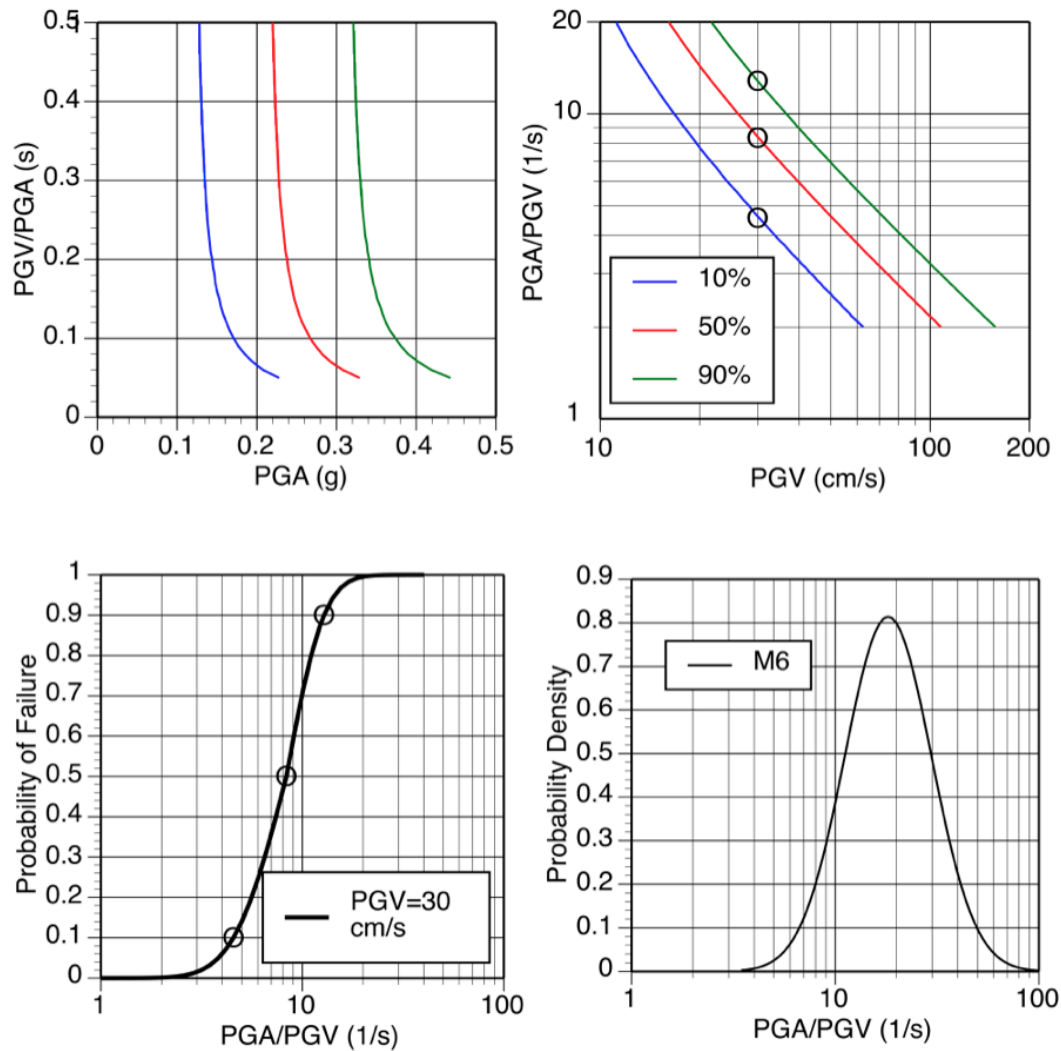
Figure 37. Top left, The reported failure probabilities for precariously balanced rock Matt Cubed as a function of peak ground acceleration and peak ground velocity (PGA; PGV). Top right, The same failure probabilities expressed as PGA/PGV versus PGV. Bottom left, The probability of failure as a function of PGA/PGV, given PGV=30 cm/s. Bottom right, The distribution of PGA/PGV values expected from a **M**=6 earthquake.

So how does PGA/PGV depend on **M**? This is shown empirically in figure 38. These data pairs have been developed for rock sites (V_{S30} >500 m/s) at short distances (R<20 km) from the NGA data set (Chiou and others, 2008) and have a significant dependence on magnitude:

$$E[\ln(PGA/PGV)] = 6.08 - 0.534M - 0.074(M - 6.07)^2 \qquad (6)$$

This relation is shown with the data from which it was derived in figure 38 and has a standard deviation of 0.49. Fortunately, there is not a significant site dependence of PGV/PGA so long as V_{S30} ≥500 m/s (although there is a site dependence for V_{S30} less than this). The variability around equation 6 is estimated by assuming ln(*PGV/PGA*) is a random variable *y* with a median value given by equation 6 and a standard deviation of 0.49. The pdf for PGA/PGV is then

$$f_{PGA/PGV}(y \mid M) = \frac{1}{0.49y\sqrt{2\pi}} \exp{-0.5}\left[\frac{\ln y - [6.08 - 0.534M - 0.074(M-6.07)^2]}{0.49}\right]^2 \qquad (7)$$

The lower right panel of figure 37 shows this pdf for **M**=6.
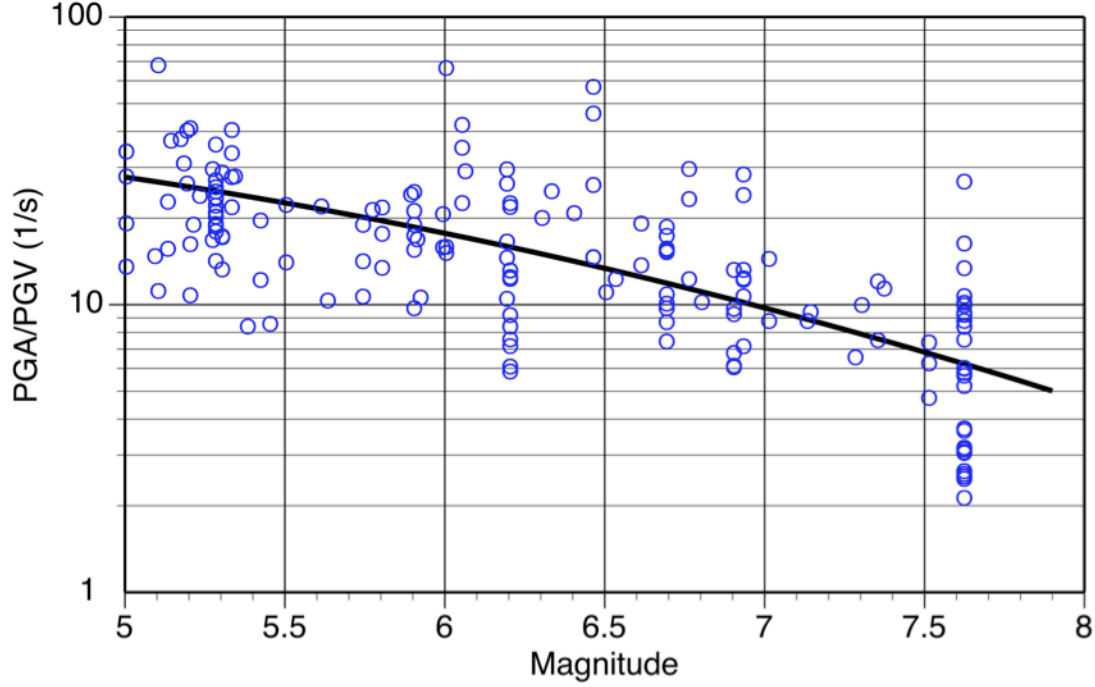
Figure 38. Plot showing scaling of PGA/PGV (peak ground acceleration/peak ground velocity) with magnitude for rock sites (V_{S30} > 500 m/s) at close distances.

Knowing the probability of failure of the PBR given a PGV and PGA/PGV pair and the distribution of PGA/PGV values for every earthquake magnitude, we can integrate over all possible PGA/PGV values to obtain the probability of failure for every PGV and **M** (at the close distances implicit in fig. 38):

$$P(G_{fails} \mid PGV = z, \mathbf{M} = m) = \int P(G_{fails} \mid PGV = z, PGA/PGV = y) * f_{PGA/PGV}(y \mid m)dy \qquad (8)$$

where $P(G_{fails} \mid PGV, \mathbf{M})$ for each **M** is a generalized form (to PGV *and* **M**) of the FGS fragility obtained in equation 2. Here, it is obtained in the same manner as the lower left frame of figure 37; $f_{PGA/PGV}$ is obtained from equation 7. PGV-based fragilities for a range of magnitudes are shown in figure 39 for the precariously balanced rock Matt Cubed at Point C.
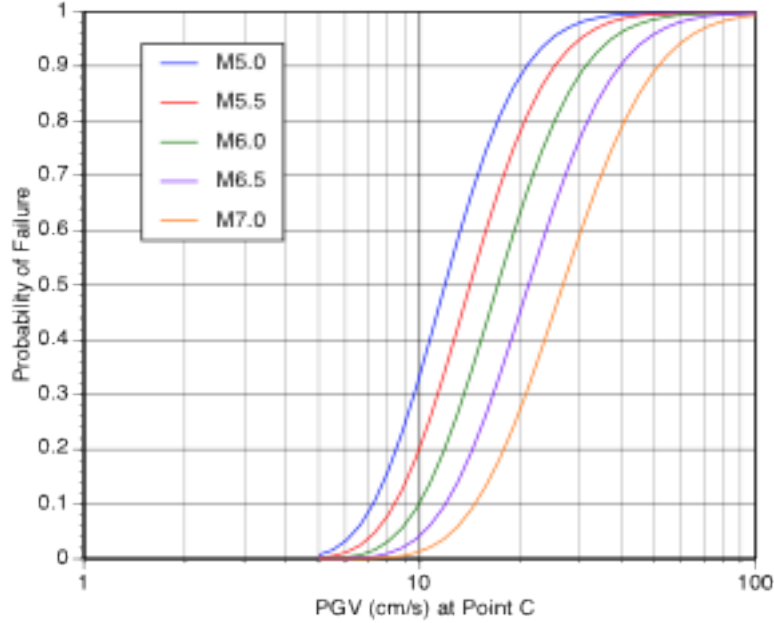
Figure 39. Plot showing magnitude dependence of the peak ground velocity-based fragilities for Matt Cubed at Point C.

Why does it take larger PGVs to drive Matt Cubed to failure at larger magnitude, as shown in figure 39? Because the PGV/PGA ratio depends on magnitude, therefore, the resulting fragility, converted to a single ground motion parameter, will be magnitude-dependent. For larger earthquake magnitudes, the fragility is shifted to higher ground motions. This may seem counter-intuitive as it indicates that large magnitude earthquakes require higher PGV values to topple the rock than do small magnitude earthquakes. The reason for this is that the fragility of the rock is more sensitive to PGA than the PGV. For the same PGA level, the larger magnitude earthquakes have, on average, a larger PGV, as indicated in figure 38. So to reach the same PGA level, a larger magnitude earthquake will have a larger PGV than a smaller magnitude earthquake.

Figure 40 shows the **M**=6 fragilities at Point B, the repository horizon, for the several PBRs and rock stacks for which we have both dynamic-fragility data and fragility ages. The rock stack Len (fig. 23) is the most stable, and PBRs Matt Cubed and Tripod (fig. 20) are the most fragile. All of the calculations for the PBRs are made at the surface, of course, where they reside, but we are interested in the seismic hazard at the repository horizon and so make the Point C-to-Point B adjustment.

Finally, we compute the annual failure probabilities as before, now incorporating the magnitude dependence of the fragility (equation 8) and the magnitude deaggregation probabilities from the hazard equation $\nu(z)$, $P(\mathbf{M}=m|\ PGV=z)$, and then integrating over all magnitudes:

$$P_{annual}[G_{fails}(t)] = \sum_i \sum_j P(G_{fails}|PGV = z_i, M = \frac{m_j + m_{j+1}}{2}) \times$$

$$\left[\nu(z_i)Deagg(z_i, m_j < M < m_{j+1}) - \nu(z_{i+1})Deagg(z_{i+1}, m_j < M < m_{j+1})\right]$$

(9)

This result can then be used to compute survival probabilities as before.
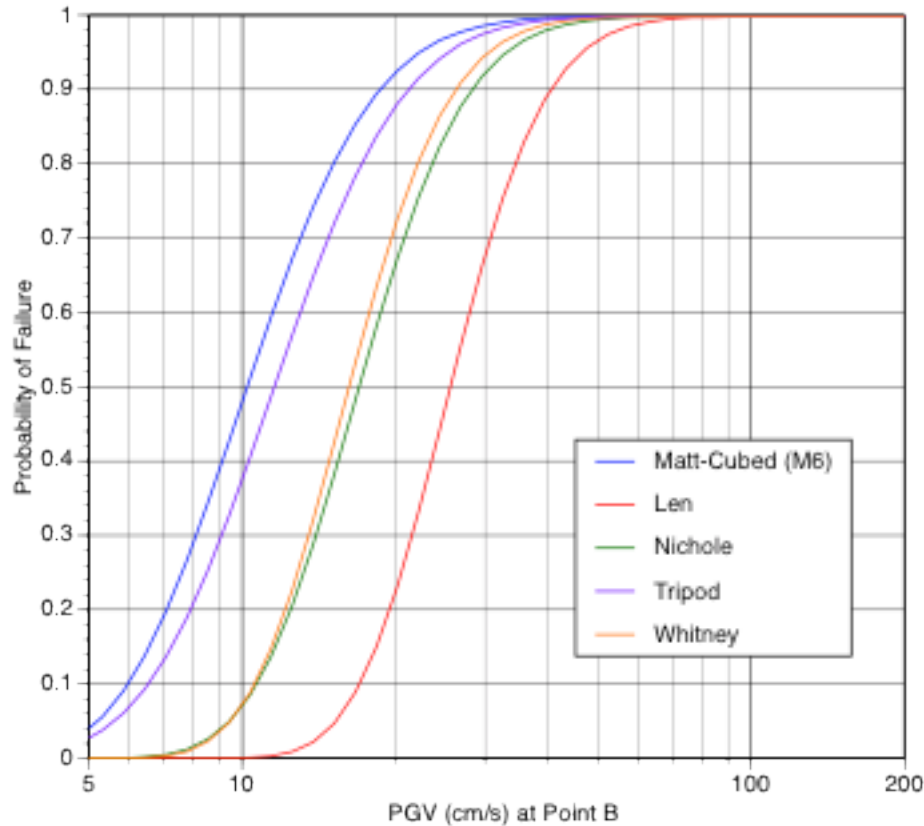
Figure 40. Plot showing the **M**=6 peak ground velocity-based fragilities at Point B for precariously balanced rocks and rock stacks on the west face of Yucca Mountain.

Fragile Geologic Structures that Evolve with Time

In the previous section, we considered the unexceeded ground motions (UGM) expressed by fragile geologic structures (FGS) in terms of constant fragilities for some fixed period of time. For the lithophysal units, it is a safe assumption that the lithophysae have not changed their shapes since the volcanic tuffs in which they formed solidified at ~12 Ma. FGS that owe their existence to one form of erosion/exhumation or another, however, will experience a time-dependent fragility as it evolves from a more stable configuration to an increasingly more fragile one—until it fails. Hoodoos, natural bridges and arches, and PBRs will all evolve to progressively more fragile states: they have time-dependent fragilities.

This evolution is sketched schematically in figure 41, parameterized in terms of PGV_{50}, the PGV that has a 50 percent chance of causing some PBR or precarious rock stack to fail. At 200 ka, we suppose that the PBR has just been exposed by the fall-down of the rocks in front of it and that a PGV_{50}=5 m/s is needed to topple it with 50 percent probability (this is hardly a precarious rock!). As erosion works away at the cooling joints and other fractures, PGV_{50} progressively decreases, such at the present time PGV_{50} is only 0.2 m/s.

With respect to the PBRs on the west face of Yucca Mountain, we know that PGVs of ~5 m/s from UNEs on Pahute Mesa caused massive cliff fracturing and failure, so we chose this value for the PGV_{50} of a freshly formed cliff face or newly exposed rock. We also know the present-day fragilities of

the various PBRs discussed earlier, and PGV_{50}=0.2 m/sec is very close to that for Tripod for **M**≥6 earthquakes.
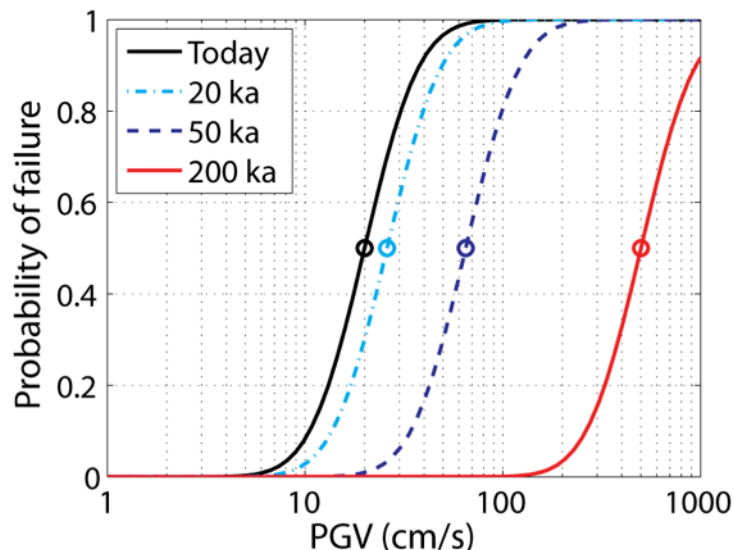
Figure 41. Schematic plot of time-dependent fragility for a precariously balanced rock.

Figure 42 shows two conceptual models of fragility evolution, each of which evolves from the intact cliff face at 200 ka to the current fragile feature today. Model 1 shows a linear decrease of log PGV_{50} with time, and Model 2 shows a quadratic decrease of log PGV_{50} with time. Both models slow their decrease at 15 ka, incorporating the idea that the warmer, drier Holocene climate slowed the erosion rate over the last fifteen thousand years.

We shall compute annual probabilities of failure for the four alternative models for the time dependence of the fragility sketched in figure 43 and listed in table 3. As above, Model 1 is for a linear decrease of log PGV_{50} from 200 ka to 15 ka, with a flattening thereafter due to climate change at the Pleistocene-Holocene boundary. Model 2 is for the quadratic decrease of log PGV_{50} from 200 ka to 15 ka, with the same flattening thereafter as in Model 1. Model 3 (which is what we used earlier in this report) uses a constant fragility age for each PBR, taken here to be 70 ka (the approximate age of Tripod), with the PBR immovable before then. Model 4 is functionally the same as Model 3, but here the fragility age is taken to be 15 ka, the nominal varnish microlamination (VML) age; this is a minimum fragility age for the Yucca Mountain PBRs.
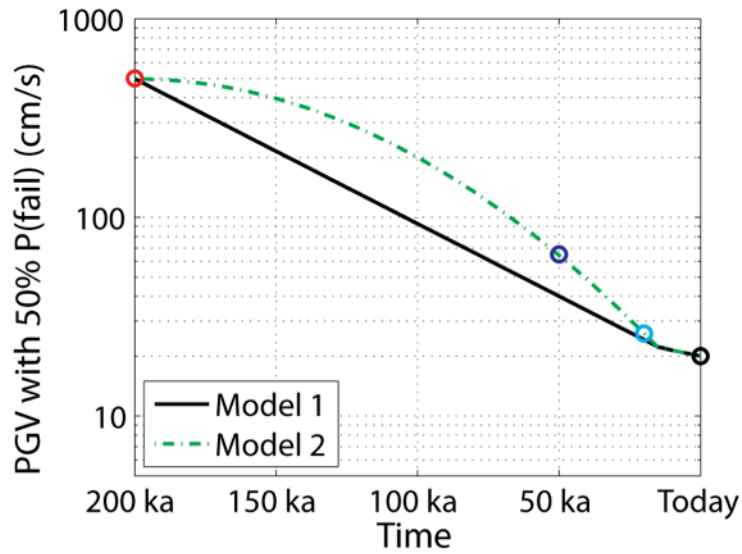
Figure 42. Plot of the linear and quadratic models for evolution of median fragility values in time.

Table 3. Alternative models for the time dependence of the fragility.

Model	Approach	Age
1	Linear evolution of median log PGV from free face fragility to current fragility, with climate change	Free-face formed at 200 ka
2	Quadratic evolution of median log PGV from free face fragility to current fragility, with climate change	Free-face formed at 200 ka
3	Constant fragility	70 ka
4	Constant fragility	15 ka
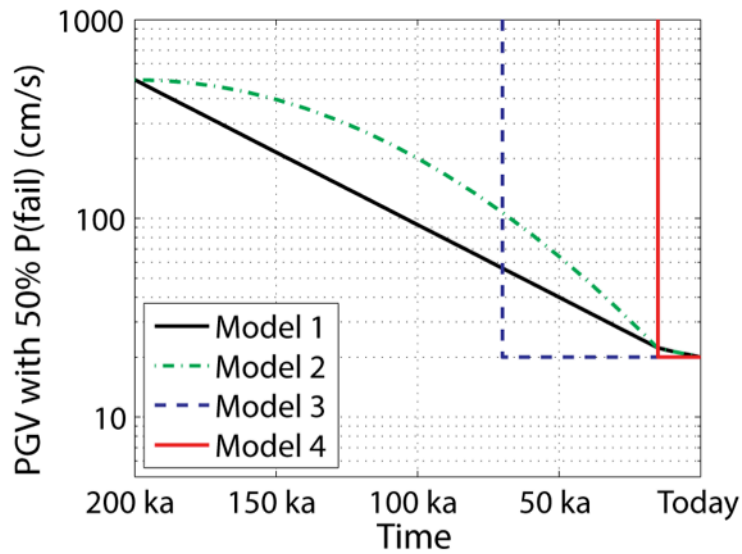
Figure 43. Plot showing the four models for the time-dependent peak ground velocity value associated with 50 percent probability of failure.
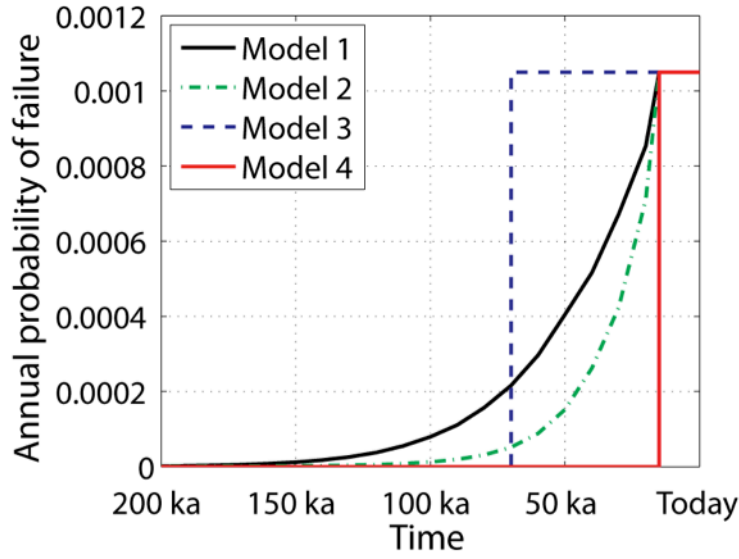
Figure 44. Plot showing annual probabilities of failure as a function of time for each of the four models, given the time-varying fragilities shown in figure 43.

Figure 44 shows the annual probabilities of failure for these four fragility models as a function of time before present, given the mean hazard curve from the 1998 Yucca Mountain PSHA. These annual failure probabilities are computed using the same approach as equation (2) earlier, but the fragility function and $P(G_{fails})$ now depend on time t:

$$P_{annual}[G_{fails}(t)] = \int \frac{d\nu(z)}{dz} P[G_{fails} \mid z,t] dz = \sum_{i=2}^{N_z} [\nu(z_{i-1}) - \nu(z_i)] P[G_{fails} \mid z = \frac{z_{i-1} + z_i}{2}, t] \tag{10}$$

We see in figure 44 that Model-3 failure probabilities are constant for the past 70 ky and drop to zero before then (in its "immovable" state). Model 4 shows the same form, but drops to zero before 15 ka. Models 1 (linear) and 2 (quadratic) have very low probabilities of failure until ~100 ka, when they begin to increase noticeably. Failure probabilities for Model 1 are always higher than for Model 2 because its log PGV_{50}s are always lower until both models become the same at 15 ka.

Given these annual failure probabilities, we can compute the probability of the feature surviving to the present day. The annual probability of surviving is one minus the probability of failure, and the probability of surviving over all years is the product of these survival probabilities:

$$P(G_{not\ failed}) = \prod_{t=1}^{T} \{1 - P_{annual}[G_{fails}(t)]\}. \tag{11}$$

Note that in the case where the annual probability of failure is constant over T years, equation 11 simplifies to the time-independent equation 3.

To find a corresponding unexceeded ground motion, we again move the hazard curve down by a factor α, which will reduce the annual failure probabilities by the same factor alpha, until the probability of survival in equation 3 is 5 percent:

$$0.05 = P_1 = \prod_{t=1}^{T} [1 - \alpha P_{annual}(G_{fails}(t))] \qquad \text{(12)}$$

Additionally, we need to find the median of the PGVs associated with failure of the feature over its lifetime as indicated in figure 34, again denoting this Z_1. We then plot the unexceeded ground motion at Z_1 and the height of the hazard curve shifted down by the factor α determined from equation 12. Figure 45 shows plots of the UGMs obtained using this approach for each of the four time dependent models in figure 44.
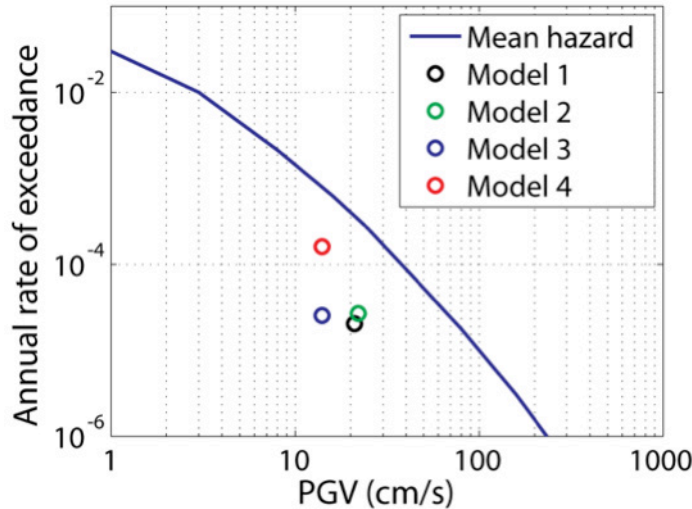
Figure 45. Plot showing comparison of the unexceeded ground motions for the four time-dependent fragility models.

Several observations can be made regarding the results shown in figure 45. Model 4 results in a higher rate for the UGM than the other models, because the short lifetime assumed in this model means that the hazard would not need to be reduced as significantly (alpha would not need to be so small) for the feature to have a 5 percent probability of surviving. This matches our intuition, as the short lifetime should provide a weaker constraint on ground motion hazard. Models 1 and 2 have z_1 values for PGV that are larger than for Models 3 and 4; this is because the feature is much less precarious for most of its lifetime, and so failures of the feature in that state are associated with larger PGV values on average. Models 1 and 2 produce nearly identical locations for the resulting UGM, indicating that the choice of the linear decrease versus a quadratic decrease in fragility for these models shown in figures 42 and 43 matters hardly at all.

Discussion and Implications

Figure 46 summarizes, in the points in hazard space graphical format, what we have discussed and quantified earlier in this report. Shown here are the physical limits for earthquake ground motion at Yucca Mountain, the unexceeded ground motions represented by the lithophysal units and the PBRs, and the results of the simplified hazard models using the more recent NGA relations for the ground motion characterization (GMC). All results are reckoned in terms of PGV at Point B, and PBR parameters necessary to calculate their unexceeded PGVs are listed in table 4. Also shown are the mean, median, and the other fractile PGV hazard curves arising from the 1998 Yucca Mountain PSHA.
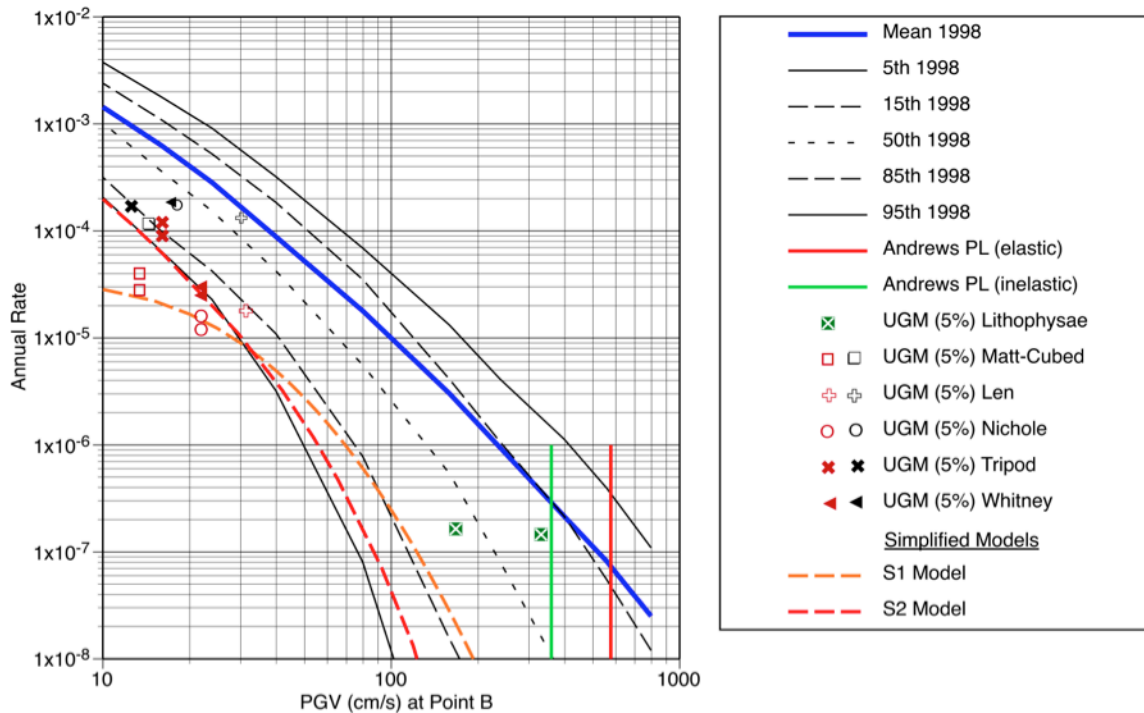
Figure 46. Graph of physical limits, unexceeded ground motions (UGM) for the lithosphysal units, precariously balanced rocks as points in hazard space, and the simplified hazard models are plotted here with the 1998 Yucca Mountain fractile hazard curves. Red symbols represent PBR ages based on the abundances of ^{36}Cl and black symbols represent the varnish microlamination ages, all taken to be 15 ka.

The physical limits for ground motion at Yucca Mountain, developed by Andrews and others (2007), 3.6 m/s for the inelastic case and 5.8 m/s for the elastic case, provide the basis for truncating the PGV hazard curves at these values. The elastic limit is comparable to PGVs from the UNEs that shattered Boxcar Bluff and many other free-standing cliffs on Pahute Mesa. We conclude that such PGVs have not occurred at Yucca Mountain over the residence times of the far fewer boulders that now reside on the west face of Yucca Mountain, for at least 250,000 years and perhaps as much as 500,000 years.

Table 4. Fragility ages used for calculating Z1 and 1/α to determine the points in hazard space at Point B for the precarious rocks and undamaged lithophysae.

Feature	Age (ka)	Z_1 (cm/s)	$1/\alpha$ (factor below mean hazard)
Matt-Cubed	50–70	13.4	21–30
Nichole	180–200+	31	35–39
Tripod	60–75	22	22–27
Len	63-77	16	5.4-6.6
Whitney	> 60-75	21.5	15-Dec
Lithophysal, LMT	12,000	167	18
Lithophysal, UMT	12,000	275	2.7

Such ground motions would also have done considerable damage to the lithophysal units. The 5 percent survival probabilities shown in figure 46 for the UMT (right point) and LMT (left point) representation of the lithophysal properties probably overstate the PGVs expected, at least in terms of what has *not* happened in the past. Because there is no observable indication of even minor damage to the lithophysal units, it is unlikely that they have experienced PGVs≥1–2 m/s since they were formed at ~12 Ma.

All of the PBRs suggest that the 1998 mean hazard curve for Yucca Mountain is too high, but at much greater probabilities of exceedance, 10^{-5}/yr to $2x10^{-4}$/ yr. While there is some uncertainty in their fragility ages, the 5 percent survival probabilities of these fragile geologic structures all sit well below the 1998 mean hazard—unless the VML ages of 15 ka represent the true fragility ages; we have taken them here to be absolute minimum fragility ages for the PBRs. The model calculations exploring the sensitivity to time-dependent fragilities reveal much the same tendency.

Likewise, both of the simplified hazard models we developed earlier sit significantly below the 1998 mean hazard curve. The simplified hazard models use only the median NGA ground-motion models for the Yucca Mountain V_{S30} and should only be compared to the 1998 median seismic hazard curve. The two simplified hazard models are consistent with most of the UGM, except when calculated for the VML ages, and both admit only the 15 percent fractile of the 1998 Yucca Mountain PSHA.

Thus, all of the ExGM research that we have been able to quantify in hazard space suggests that the 1998 mean hazard curve significantly overstates the seismic hazard at Yucca Mountain. This is true not only at very low probabilities of exceedance, 10^{-6}/yr to 10^{-8}/yr, but also at much higher probabilities of exceedance, 10^{-3} to 10^{-5}/yr. What has caused this? For the larger probabilities of exceedance, the separation of the hazard curves is primarily due to the separation of the median NGA ground-motion estimation models from those used in the 1998 Yucca Mountain PSHA: the NGA relations yield lower median ground motions than do the 1998 Yucca Mountain models. At the lower probabilities of exceedance, the separation of the 1998 Yucca Mountain fractiles is the result of the different medians of the models contributing to the 1998 Yucca Mountain GMC as well as the larger ground-motion sigmas associated with the larger fractiles. This is epistemic uncertainty in the ground-motion aleatory variability (sigma): larger sigmas flatten the slope of the hazard curves, while smaller sigmas increase the slope.

What we cannot do, to finesse extreme ground motions or any other ground motions arising from PSHA, is truncate the ground-motion distribution functions at two or three or any other sigma. There is no analysis known to us that justifies this approach, and neither does ExGM research on the NGA dataset of PGVs with respect to the Abrahamson and Silva (2008) model (fig.24), or earthquake stress-drop distributions (fig. 29).

The End…of the Beginning

When ExGMCom was formed in the fall of 2003, the unique character and many dimensions of extreme ground motions, the extremely large amplitudes of earthquake ground motions that arise at extremely low hazard levels, presented new and unique challenges to many different interests. There was no simple highway to follow, nor much of anything in the way of guidance. For lack of any clear direction, ExGMCom sampled the entire breadth of the earth sciences, to the extent that the knowledge and expertise of its members permitted, to see what we could put to work on this matter. These ideas were assembled at the August 2004 Workshop and compiled in the Workshop Report (Hanks and others, 2006), from which the ExGM research plan was fashioned with its three basic elements of physical limits to earthquake ground motions, unexceeded ground motions, and the frequency-of-occurrence of ground-motion amplitudes and (or) earthquake source parameters that cause them.

On the basis of that report, the Science and Technology Program (S&T) in the Office of Civilian Radioactive Waste Management (OCRWM) of the United States Department of Energy (DOE) funded the ExGM project as a 5-year, $5 million research program to develop methodologies to understand extreme ground motions in general, not as a real or potential fix for Yucca Mountain. The S&T Program Office also required broad community participation in the ExGM research program, which was accomplished through SCEC institutionally and its scientists individually. To execute its research plan, ExGM supported university scientists with grants awarded through SCEC and provided USGS scientists with funds flowing through the Pacific Gas & Electric Company (PG&E)/USGS Cooperative Research and Development Agreement; PBR research efforts at the University of Nevada Reno (UNR) and exposure-age determinations at Lawrence Livermore National Laboratory (LLNL) were supported directly from PG&E. No matter what their institutional affiliation, every one of these scientists has been an active participant in SCEC activities, especially the SCEC Annual Meeting held each September.

Those who have read this far will know that the ExGM research program has a very broad reach and appealed to an equally broad range of earth sciences interests. The talented scientists of SCEC, UNR, and USGS responded to all of these interests and challenges. But for reasons we still don't understand, this research program had an enormous reach beyond the two dozen or so ExGM-funded scientists. From 2005 to 2010, more than 100 scientists sacrificed their weekends to come to a place with daytime temperatures of an even greater number (°F) to attend ExGM/SCEC workshops, which reviewed the accomplishments of the previous year.

Two obvious appeals of ExGM were the novelty of extreme ground motions and the importance of the facility for which they first arose, Yucca Mountain; as a practical matter, there was also concern about just what, if anything, could be done with PGVs in excess of anything ever observed, 2–3 m/sec. Another attraction was the very broad reach of the ExGM research program, from computationally intensive nonlinear stress-wave excitation and propagation on one end of the spectrum to classical Quaternary geology and geomorphology on the other. Of particular interest here are the implicit time intervals involved—tens of thousands of years to tens of million years—for hazard levels of 10^{-4}/yr to 10^{-8}/yr and thus the potential application of the methods and models of Quaternary geology and geomorphology to extreme ground motions. Finally, the growing recognition and understanding of the antiquity of the Yucca Mountain landscape, while providing new vistas on the problem at hand, are

of considerable geomorphological and climatological interest in their own right, apart from any hazard analysis.

ExGM scientists have fulfilled all of these interests and concerns by driving major advances in:

- Delineating the ground motions and faulting displacements that accompany spontaneous, dynamically propagating, "complete" stress-drop earthquake models
- Understanding the causes and effects of nonlinear stress-wave propagation in rock and how this leads to physical limits of ground motion
- Refining the toppling probabilities and fragility ages of precariously balanced rocks (PBRs), thus allowing better probabilistic portrayals of unexceeded ground motions. These methods are general; the ExGM applications are for PBRs on the west face of Yucca Mountain
- Quantifying the spectacular morphological differences of the UNE-shattered cliffs (extreme geomorphology) on Pahute Mesa and the comparatively "clean" west face of Yucca Mountain.
- Determining the surprising antiquity of the Yucca Mountain landscape (the "million-year-old landscape") through many new surface-exposure ages
- Developing the points-in-hazard-space methodology, allowing a wide range of geologic, geomorphic, and geophysical hazard data and constraints to be placed in a single figure
- Developing a_{rms} stress drops from the global m_b-M database and determining that the distribution of these stress drops for 441 crustal earthquakes is log-normal to 2+ sigma at its upper end
- Compiling a global database of the largest surface-faulting displacements for normal-faulting earthquakes, for both historic and late Quaternary (paleoseismic) events
- Documenting the magnitude-independence of apparent stresses in the western United States

Nonlinear stress wave propagation in rock is a new research area for most earthquake scientists. Large stress differences associated with faulting events; fault splays, kinks, and other geometric irregularities; pulverization of fault zone rocks; the material response of weakly consolidated sedimentary and volcanic rocks; and pore collapse can all lead to irreversible, dissipative energy losses that will limit the amplitudes of earthquake ground motion. These limits are, or will be, true physical limits to earthquake ground motion. Their PSHA applications will, in general, make a difference only at low hazard levels, as they have here for Yucca Mountain. There can be little doubt, however, that what was begun here in the way of nonlinear stress-wave propagation in rock will continue for the indefinite future.

Considerable progress on understanding PBRs—and more generally the whole class of fragile geologic structures—as quantitative measures of unexceeded ground motions has been made in the course of the ExGM research program. Determining the dynamic fragilities of PBRs is a sophisticated and time-consuming business and estimating the age of fragility for any PBR is subject to uncertainty of poorly known magnitude, even with abundant exposure-age data. But we now know much better how to do these things. The time-dependent fragility model we have developed here illustrates the basics of evolving (and increasing) fragility with continuing erosion between the exposure ages and the VML ages for the Yucca Mountain PBRs. We are confident that continuing research into the origin and evolution of fragile geologic structures, whether it be by exhumation or by subaerial erosion, will make for continuing improvement of fragility ages. Recent examples of such research include Haddad (2010) and Balco and others (2010). The unexceeded ground motions represented by fragile geologic structures are the only way to validate seismic hazard curves over long periods of time.

The geomorphic features displayed on Pahute Mesa and the west face of Yucca Mountain, and the great antiquity of the Yucca Mountain landscape are specific to these sites, of course, but the general application of the methods of Quaternary geology and geomorphology to PSHA at hazard levels of 10^{-4}/yr and smaller are quite general. The exposure-age dating determined by the abundances of ^{10}Be and

[36]Cl used here to determine fragility ages of PBRs and the residence times of boulders on the landscape are widely applicable in most terrestrial environments.

The points-in-hazard-space graphic developed early in the course of the ExGM research program is also general in its application to PSHA for any site, although we have developed it here with respect to the 1998 Yucca Mountain PSHA. It is especially valuable in representing geologic and geomorphic data and constraints of Pleistocene ages, including PBRs.

Research on ground-motion and earthquake-source-parameter distribution functions has been ongoing for decades, and datasets are finally becoming large enough to examine 2+ sigma ground-motion amplitudes and earthquake stress drops. The compilation of 441 a_{rms} stress drops for global crustal earthquake is an impressive development. So too is the compilation of the largest normal-faulting displacements, which motivates further analysis of faulting displacements for the paleoseismic events. The stress differences that drive and accompany crustal earthquakes, no matter how they are calculated, remain independent of the size of the earthquake.

These many accomplishments notwithstanding, ExGMCom believes the success of the ExGM research program lies not so much in what has been achieved in the past five years, but in what it offers for the future, both as a continuing research agenda for what ExGM project scientists began—but hardly finished—and also as a set of methods, models, and databases that can be applied to seismic hazard analysis for critical facilities *anywhere* in the world. What has not happened as a result of ExGM is the execution of—or even the planning for—a new PSHA for Yucca Mountain. As this report nears completion in the summer of 2013, the future of Yucca Mountain as a radioactive-waste repository seems bleak, and this obvious application of ExGM research may never happen. Whether it does or not, however, will not matter much to the continuing legacy of ExGM research.

Acknowledgments

Survey), J.W. Dewey, R.A. Harris, S. Hecker, D.A. Lockner, C.A. Morrow, J.B. Paces, and D.P. Schwartz. At the SCEC, they include J.R. Arrowsmith, I.W. Bailey, A. Baltay, Y. Ben-Zion, G.C. Beroza, H. Bhat, B. Duan, S.M. Day, R. Dmowska, D.E. Haddad, S. Ma, J.R. Rice, E.L. Templeton and numerous members of the dynamic-rupture code validation project led by R.A. Harris. At the University of Nevada, Reno, they include J.G. Anderson, R. Anooshehpoor, and M.D. Purvance. The isotopic abundance determinations for exposure ages reported here were performed by D.H. Rood and R.C. Finkel at the Center for Accelerator Mass Spectrometry (CAMS) of the LLNL.

A review team of SCEC scientists, G.C. Beroza (chair), S.M. Day, L. Grant-Ludwig, R.B. Smith, and R.J. Weldon, reviewed this manuscript in preliminary form in preparation for a three-day field trip to NTS and Yucca Mountain. They reviewed it again as a first-draft manuscript in the spring and summer of 2011, as did D.J. Andrews and R.A. Harris in preparation for its release as a U.S. Geological Survey Open-File Report. P. McCrory's sharp eyes caught a number of typos in the penultimate version.

The ExGM research program performed on a platform of the huge amount of earth science information already compiled in the Yucca Mountain Site Characterization Plan, itself a 1500-page document; the 1998 Yucca Mountain PSHA; and the License Application documentation. Portions of this material have been briefly summarized earlier, but we will emphasize once more the significance of the paleoseismic record to ExGM research. In both its completeness for so many faults for so long a time (~100 ka) and that it extends back ~800 ka, however incompletely, this paleoseismic history is without precedent in the earth sciences. At the same time, this long record would not be discernible but for the very low rates of earthquake faulting and the very low rates of erosion that might otherwise destroy this record of faulting. More is known about the Pleistocene geology of the Yucca Mountain area than for any other nonglaciated region in the world. All ExGM research program scientists are grateful to the hundreds of earth scientists who compiled this information over the decades preceding OCRWM ExGM research program.

References

Abercrombie, R., 1995, Earthquake source scaling relationships from -1 to 5 M$_L$ using seismograms recorded at 2.5-km depth: Journal of Geophysical Research, 100, p. 24015–24036.

Abrahamson, N., Atkinson, G., Boore, D., Bozorgnia, Y., Campbell, K., Chiou, B., Idriss, I.M., Silva, W., and Youngs, R., 2008, Comparisons of the NGA ground-motion relations: Earthquake Spectra, v. 24, p. 5–66.

Abrahamson, N.A., and Hanks, T.C., 2008, Points in hazard space—a new view of PSHA [abs.]: Seismological Research Letters v. 79, p. 285.

Abrahamson, N., and Silva, W., 2008, Summary of the Abrahamson & Silva ground-motion relations: Earthquake Spectra v. 24, p. 67–97.

Anderson, J.G., 2010, Source and site characteristics of earthquakes that have caused exceptional ground accelerations and velocities: Bulletin of the Seismological Society of America, v. 100, p. 1–36.

Anderson, J.G. and Brune, J.N., 1999, Probabilistic hazard analysis without the ergodic assumption: Seismological Research Letters, v. 70, p. 19–23.

Anderson, L.W., and Klinger, R.E., 2004, Quaternary faulting on the Bare Mountain fault, chap. 12 *of* Keefer, W.R., Whitney, J.W., and Taylor, E.M., Quaternary paleoseismology stratigraphy of the Yucca Mountain area, Nevada: U.S. Geological Survey Professional Paper 1689, 212 p., 26 pls (available at: http://pubs.er.usgs.gov/publication/pp1689, accessed Jan, 31, 2013).

Anderson, J.G., Purvance, M., Anooshehpoor, R., and Brune, J.N., 2007, Simplifed probabilistic seismic hazard analysis for precarious rocks on Yucca Mountain, Nevada [abs.]: Seismological Research Letters, v.78, p. 281.

Andrews, D. J., 2006, Deterministic modeling of physically-limited ground motion, *in* Hanks, T.C., Abrahamson, N.A., Board, M., Boore, D.M., Brune, J.N., and Cornell, C.A., Report of the workshop on extreme ground motions at Yucca Mountain, August 23–25, 2004:U.S. Geological Survey Open-File Report 2006-1277, 234 p. plus appendixes (available at http://pubs.usgs.gov/of/2006/1277/, accessed Jan. 31, 2013).

Andrews, D.J., Hanks, T.C., and Whitney, J.W., 2007, Physical limits on ground motion at Yucca Mountain: Bulletin of the Seismological Society of America, v. 97, p. 1771–1792.

Axen, G.J., 2004, Mechanics of low-angle normal faults, *in* Karner, G., Taylor, B., Driscoll, N., and Kohlstedt, D.L., Rheology and Deformation in the Lithosphere at Continental Margins: New York, Columbia University Press, p. 46–91.

Balco, G., Purvance, M.D., and Rood, D., 2010, Exposure dating of precariously balanced rocks: Quaternary Geochronology, v. 6, p. 295–303.

Baltay, A., Prieto, G., and Beroza, G.C., 2010, Radiated seismic energy from coda measurements indicates no scaling in apparent stress with seismic moment: Journal of Geophysical Research, v. 115, B08314, doi:10.1029/2009JB006736.

Boore, D.M., 1983, Stochastic simulation of high-frequency ground motions based on seismological models of the radiated spectra: Bulletin of the Seismological Society of America v. 73, p. 1865–1894.

Boore, D.M., 1986, Short-period *P*- and *S*-wave radiation from large earthquakes— implications for spectral scaling relations: Bulletin of the Seismological Society of America, v.76, p. 43–64.

Boore, D.M., 2003, Prediction of ground motion using the stochastic method: Pure and Applied Geophysics, v. 160, p. 635–676. (Available from the online publications link on http://www.daveboore.com.)

Boore, D.M., 2005, SMSIM—Fortran programs for simulating ground motions from earthquakes— version 2.3—a revision of OFR 96–80-A: U.S. Geological Survey Open-File Report00-509, version 2.18, Aug. 15, 2005, 55 p. (Available at http://geopubs.wr.usgs.gov/open-file/of00-509/, accessed Jan. 31, 2013.)

Boore, D.M., and Atkinson, G.M., 2008, Ground-motion prediction equations for the average horizontal component of PGA, PGV, and 5%-damped PSA at spectral periods between 0.01 s and 10.0 s: Earthquake Spectra v. 24, p. 99–138.

Boore, D.M., Watson-Lamprey, J., and Abrahamson, N.A., 2006, Orientation-independent measures of ground motion, Bulletin of the. Seismological Society of America, v. 96, p. 1502–1511.

Brocher, T.M., Hunter, W.C., and Langenheim, V.E., 1998, Implications of seismic reflection and potential field geophysical data on the structural framework of the Yucca Mountain–Crater Flat region, Nevada: Geological Society of America Bulletin, v. 100, p. 947–971.

Brune, J.N., 1970, Tectonic stress and the spectra of seismic shear waves: Journal of Geophysical Research v. 75, p. 4393–4405.

Brune, J.N., 1971, Correction [to "Tectonic stress and the spectra of seismic shear waves"]: Journal of Geophysical Research, v. 76, p. 5002.

Brune, J.N., 1996, Precariously balanced rocks and ground-motion maps for southern California, Bulletin of the Seismological Society of America, v. 86, p. 43–54.

Brune, J.N., von Seggern, D., and Anooshehpoor, R., 2003, Distribution of precarious rocks at the Nevada Test Site—comparison with ground motion predictions from nuclear tests, Journal of Geophysical Research, v. 108, no. B6, doi:10.1029/2002JB002000.

Brune, J.N., and Whitney, J.W., 1992, Precariously balanced rocks with rock varnish—paleoindicators of maximum ground acceleration? [abs.]: Seismological Research Letters, v. 63, p. 21.

BSC (Bechtel SAIC Company), 2004, Development of earthquake ground motion input for preclosure seismic design and postclosure performance assessment of a geologic repository at Yucca Mountain, NV: Las Vegas, Nevada: Bechtel SAIC Company, document number MDL-MGR-GS-000003 REV 01, ACC: DOC.20041111.0006; DOC.20051130.0003; DOC.20090430.0003.

BSC (Bechtel SAIC Company), 2005, Peak ground velocities for seismic events at Yucca Mountain, Nevada: Las Vegas, Nevada, document number ANL-MGR-GS-000004 REV 00.

Chiou, B., Darragh, R., Gregor, N., and Silva, W., 2008, The NGA project strong-motion database: Earthquake Spectra, v. 24, p. 23–44.

CRWMS M&O, 1996, Probabilistic volcanic hazard analysis for Yucca Mountain, Nevada: Las Vegas, Nev., report BA0000000-01717-2200-00082 Rev. 0.

CRWMS M&O, 1998, Probabilistic Seismic Hazard Analyses for Fault Displacement and Vibratory Ground Motion at Yucca Mountain, Nevada: Las Vegas, Nev., vols. 1–3, milestone SP32IM3.

Day, W.C., Dickerson, R.P., Potter, C.J., Sweetkind, D.S., San Juan, C.A., Drake II, R.M., and Fridrich, C.J., 1998, Bedrock geologic map of the Yucca Mountain area, Nye County, Nevada: U.S. Geological Survey Geologic Investigations Series Map I–2627, scale 1:24,000.

Dewey, J.W. and Boore, D.M., 2008, Use of mb vs. Mw in the search for high stress-parameter earthquakes in regions of tectonic extension [abs.], Seismological Research Letters, v. 79, p. 284.

Duan, B., and Day, S.M., 2008, Inelastic strain distribution and seismic radiation from rupture of a fault kink: Journal of Geophysical Research, v. 113, B12311, doi:10.1029/2008JB005847.

Duan, B., and Day, S.M., 2010, Sensitivity study of physical limits on ground motion at Yucca Mountain: Bulletin of the Seismological Society of America, v. 100, p. 2996–3019.

Fridrich, C.J., Whitney, J.W., Hudson, M.R., and Crowe, B., 1999, Space-time patterns of Late Cenozoic extension, vertical axis rotation, and volcanism in the Crater Flat basin, southwest Nevada: in Wright, L.A. and Troxel, B.W., eds., Cenozoic Basins of the Death Valley Region: Geological Society of America Special Paper 333, p. 197–212.

Gosse, J., Harrington, C.D., and Whitney, J.W., 1996, Applications of in situ cosmogenic nuclides in the geologic site characterization of Yucca Mountain, Nevada: Material Research Society Symposium Proceedings, v. 412, p. 799–806.

Hammond. W.C., Kreemer, C., Blewitt, G., and Plag, H.-P., 2010, Effect of viscoelastic postseismic relaxation on estimates of interseismic crustal strain accumulation at Yucca Mountain, Nevada: Geophysical Research Letters, v. 37, L06307, doi:10.1029/2010GL042795.

Hanks, T.C., 1977, Earthquake stress drops, ambient tectonic stresses, and stresses that drive plate motions: Pure and Applied Geophysics (Special Issue: Stress in the Earth, M. Wyss, ed.), v. 115, p. 441–458.

Hanks, T.C., 1979, b-values and $\omega^{-\gamma}$ seismic source models—implications for tectonic stress variations along active crustal fault zones and the estimation of strong ground motion: Journal of Geophysical Research, v. 84, p. 2235–2242.

Hanks, T.C., Abrahamson, N.A., Board, M., Boore, D.M., Brune, J.N., and Cornell, C.A, 2006, Report of the workshop on extreme ground motions at Yucca Mountain, August 23–25, 2004: U.S. Geological Survey Open-File Report 2006–1277, 234 p. (available at http://pubs.usgs.gov/of/2006/1277/).

Hanks, T.C., Abrahamson, N.A., Boore, D.M., Coppersmith, K.J., and Knepprath, N.E., 2006, Implementation of the SSHAC Guidelines for Level 3 and 4 PSHAs—experience gained from actual applications: U.S. Geological Survey Open-File Report 2009–1093, 66 p. (available at http://pubs.usgs.gov/of/2009/1093/).

Hanks, T.C., and McGuire, R.K., 1981, The character of high-frequency strong ground motion: Bulletin of the Seismological Society of America, v. 71, p. 2071–2095.

Hanks, T.C., Winograd, I.J., Anderson, R.E., Reilly, T.E., and Weeks, E.D., 1999, Yucca Mountain as a radioactive-waste repository—a report to the Director, U.S. Geological Survey: U.S. Geological Survey Circular 1184, 19 p.

Haddad, D.E., 2010, Geologic and geomorphic characterization of precariously balanced rocks: Tempe, Arizona, Arizona State University, M.S. thesis.

Harris, R.A., Barall, M., Andrews, D.J., Duan, B., Ma,S., Dunham, E.M., Gabriel,A.-A., Kaneko, Y., Kase, Y., Aagard, B.T., Oglesby, D.D., Ampuero, J.-P., Hanks, T.C., and Abrahamson, N., 2011,Verifying a computational method for predicting extreme ground motion: Seismological Research Letters, v. 82, p. 638–644.

Harris, R.A., Barall, M., Archuleta, R., Dunham, E., Aagard, B., Ampuero, J.P., Bhat, H., Cruz-Atienza, V., Dalguer, L., Dawson, P., Day, S., Duan,B., Ely, G., Kaneko, Y., Kase, Y., Lapusta, N., Liu, Y., Ma, S., Oglesby, D., Olsen, K., Pitarka, A., Song, S., and Templeton, E., 2009, The SCEC/USGS dynamic earthquake rupture code verification exercise: Seismological Research Letters, v. 80, p. 119–126.

Hecker, S., Dawson, T.E., and Schartz, D.P., 2010, Normal-faulting slip maxima and stress-drop variability—a geological perspective: Bulletin of the Seismological Society of America, v. 100, p. 3130–3147.

Ide, S., and Beroza, G. C., 2001, Does apparent stress vary with earthquake size?: Geophysical Research Letters, v. 28, p. 3349–3352.

Itasca, 2002, Itasca software—cutting edge tools for computational mechanics: Minneapolis, Minn., Itasca Consulting Group.

Joyner, W.B., and Boore, D.M., 1981, Peak horizontal accelerations and velocity from strong-motion records including records from the 1979 Imperial Valley, California, Earthquake: Bulletin of the Seismological Society of America, v. 71, p. 2011–2038.

Kagan, E.J., Agnon, A., Bar-Matthews, M., and Ayalon, A., 2005, Dating large infrequent earthquakes by damaged cave deposits: Geology, v. 33, p. 261–264; doi:10.1130/G21193.1.

Keefer, W.R., and Menges, C.M., 2004, Summary of the temporal and spatial relations of Quaternary faulting during the past 100 ky at Yucca Mountain—evidence for distributive surface ruptures on multiple faults, chap. 14 *in* Keefer, W.R., Whitney, J.W., and Taylor, E.M., eds., Quaternary paleoseismology and stratigraphy of the Yucca Mountain Area, Nevada: U.S. Geological Survey Professional Paper 1689, p. 197–200. (available at http://pubs.usgs.gov/pp/pp1689/).

Keefer, W.R., Whitney, J.W., and Buesch, D.C., 2007,Geology of the Yucca Mountain site area, southwestern Nevada, *in* Stuckless, J.S., and Levich, R.A., eds., The geology and climatology of Yucca Mountain and vicinity, southern Nevada and California: Geological Society of America Memoirs, v. 199, p. 53–103.

Keefer, W.R., Whitney, J.W., and Taylor, E.M., eds., 2004, Quaternary paleoseismology and stratigraphy of the Yucca Mountain area, U.S. Geological Survey Professional Paper 1689, 206 p. (available at http://pubs.usgs.gov/pp/pp1689/).

Liu, T., 2003, Blind testing of rock varnish microstratigraphy as a chronometric indicator—results on late Quaternary lava flows in the Mojave Desert, California: Geomorphology, v. 53, p. 209–234.

Lockner, D.A., and Morrow, C., 2008, Energy dissipation in Calico Hills Tuff due to pore collapse [abs.]: Eos (American Geophysical Union Transactions) v. 89, Fall Meeting Supplement, abs. T51A–1856.

Mayeda, K., and Walter, W.R., 1996, Moment, energy, stress drop, and source spectra of western United States earthquakes from regional coda envelopes: Journal of Geophysical Research, v. 101, no. B5, p. 11195–11208.

McGarr, A., and Fletcher, J.B., 2007, Near-fault peak ground velocity from earthquake and laboratory data: Bulletin of the Seismological Society of America, v. 97, p. 1502–1510.

O'Leary, D.W., 2007, Tectonic models for Yucca Mountain, Nevada *in* Stuckless, J.S., and Levich, R.A., eds., The geology and climatology of Yucca Mountain and vicinity, southern Nevada and California: Geological Society of America Memoir, v. 199, p. 105–153.

Power, M., Chiou, B., Abrahamson, N., Bozorgnia, Y., Shantz, T., and Roblee, C., 2008, An overview of the NGA project: Earthquake Spectra, v. 24, p. 3–21.

Purvance, M.D., Anooshehpoor, R., and Brune, J.N., 2009, Fragilities of sensitive geological features on Yucca Mountain, Nevada: Berkeley, California, Pacific Earthquake Engineering Research Center Report.

Ramelli, A.R., Oswald, J.A., Vadurro, G., Menges, C.M., and Paces, J.B., 2004, Quaternary faulting on the Solitario Canyon Fault, chap. 7 *in* Keefer, W.R., Whitney, J.W. and Taylor E.M, eds., Quaternary paleoseismology and stratigraphy of the Yucca Mountain Area, Nevada: U.S. Geological Survey Professional Paper 1689, p. 89–110, available at http://pubs.er.usgs.gov/publication/pp1689.

Reiter, L., 2004, When are ground motion estimates too high? [abs.]: Seismological Research Letters, v. 74, p. 282.

Simonds, F.W., Whitney, J.W., Fox, K.F., Ramelli, A.R., Yount, J.C., Carr, M.D., Menges, C.M., Dickerson, R.P., and Scott, W., 1995, Fault map of the Yucca Mountain area, Nye County, Nevada: U.S. Geological Survey Miscellaneous Investigations Series Map I-2520, scale 1:24,000.

SNL [Sandia National Laboratories], 2008, Probabilistic volcanic hazard analysis update (PVHA-U) for Yucca Mountain, Nevada: Las Vegas, Nevada, TDR-MGR-PO-000001 REV 01.

SSHAC [Senior Seismic Hazard Analysis Committee, R.J. Budnitz, Chairman, G. Apostolakis, D.M. Boore, L.S. Cluff, K.J. Coppersmith, C.A. Cornell, and P.A. Morris], 1997, Recommendations for probabilistic seismic hazard analysis—Guidance on uncertainty and use of experts: Washington, D.C., U.S. Nuclear Regulatory Commission Report, NUREG/CR-6372.

Slemmons, D.B., and DePolo, C.M., 1986, Evaluation of active faulting and associated hazards, *in* Active Tectonics, Studies in Geophysics: Washington, D.C., National Academy Press, p. 45–62.

Stepp, J.C., Wong, I., Whitney, J., Quittmeyer, R., Abrahamson, N., Toro, G., Youngs, R., Coppersmith, K., Savy, J., and Sullivan, T., 2001, Probabilistic seismic hazard analyses for ground motions and fault displacement at Yucca Mountain, Nevada: Earthquake Spectra, v.17, p. 113–151.

Stock, J.M., Healy, J.H., Hickman, S.H., and Zoback, M.D., 1985, Hydraulic fracturing stress measurements at Yucca Mountain, Nevada: Journal of Geophysical Research, v. 90, no. B10, p. 8691–8706.

Stuwe, K., Robl, J., and Matthai, S., 2009, Erosional decay of the Yucca Mountain crest: Geomorphology, v. 108, p. 200–208, doi:10.1016/j.geomorph.2009.01.008.

Taylor, E.M., Menges,C.M., and Buesch, D.C., 2004, Results of paleoseismic investigations on the Ghost Dance fault, chap. 6, *in* Keefer, W.R.,Whitney, J.W. and Taylor E.M, eds., Quaternary paleoseismology and stratigraphy of the Yucca Mountain Area, Nevada: U.S. Geological Survey Professional Paper 1689, p. 71–88, available at http://pubs.er.usgs.gov/publication/pp1689.

Templeton, E.L., Bhat, H.S., Dmowska, R., and Rice, J.R., 2010, Dynamic rupture through a branched fault configuration at Yucca Mountain and resulting ground motions: Bulletin of the Seismological Society of America, v.100, p. 1484–1497.

Thatcher, W.R., and Hanks, T.C., 1973, Source parameters of southern California earthquakes: Journal of Geophysical Research, v.78, p. 8547–8576.

Whitney, J.W., and Berger, D.L., 2000, A 3.7-million-year offset rate on the Windy Wash Fault at the south end of Yucca Mountain, Nevada, chap. F *in* Whitney, J.W., and Keefer, W.R., eds., Geologic and geophysical studies of Yucca mountain, Nevada, a potential high-level radioactive-waste repository: U.S. Geological Survey Data Series 58, 9 p., available at http://pubs.er.usgs.gov/publication/ds58.

Whitney, J.W., E.M. Taylor, and J.R. Wesling (2004). Quaternary stratigraphy and mapping in the Yucca Mountain area, chap. 2, *of* Keefer, W.R.,Whitney, J.W., and Taylor E.M, eds., Quaternary paleoseismology and stratigraphy of the Yucca Mountain Area, Nevada: U.S. Geological Survey Professional Paper 1689, p. 11–22, available at http://pubs.er.usgs.gov/publication/pp1689.

Winograd, I.J., 1974, Radioactive waste storage in the arid zone: EOS (Transactions of the American Geophysical Union), v. 55, p. 884–894.

Wong, I., 2004, Development of earthquake ground motion input for preclosure seismic design and postclosure performance assessment of a geological repository at Yucca Mountain, Nevada: U.S. Department of Energy Report # MDL-MGR-GS-000003, Rev. 01, doi:10.2172/837491, available at http://www.osti.gov/energycitations/product.biblio.jsp?osti_id=837491.

Zoback, M.D., and Healy, J.H., 1984, Friction, faulting, and "in situ" stress: Annales Geophysicae, v.2, p. 689–698.

Appendix I. Data for Exposure-Age and Erosion-Rate Determinations

This appendix includes three tables of exposure ages and erosion rates, followed by brief descriptions of the analytical procedures for determining the abundances of ^{10}Be in table I-1 and ^{36}Cl in table I-2.

The Ammonia Tanks Tuff outcrops in the Castle Rock, Cholla, and SH95 (State Highway 95) study areas (table I-1) and contains enough free quartz to utilize the well known and widely used ^{10}Be analysis. The Castle Rock and Cholla areas are west of the south end of Rainier Mesa, at the mouth of Stockade Wash. The SH95 area is several kilometers south of "Steve's Pass" (36.758°N, 116.627°W), about 1 km east of the highway.

The study areas in table I-2 are all located on the west face of Yucca Mountain and include precariously balanced rocks (PBR), precipitous cliff faces, and boulders on the pediment surfaces at the base of the steep west face. There is little or no free quartz in the volcanic units of Yucca Mountain, preventing ^{10}Be or ^{26}Al analyses; the abundance of ^{36}Cl in alkali feldspar mineral separates has been determined for each of these samples.

Table I-3 presents results comparing exposure ages determined from both ^{10}Be and ^{36}Cl. We have, however, found good agreement between the ^{10}Be ages of quartz and the ^{36}Cl ages of feldspars in samples of the Ammonia Tanks Tuff at several different localities.

The "preferred exposure ages" are the minimum (zero erosion rate) exposure age corrected for the calculated erosion rates. There is an inherent ambiguity involved in interpreting cosmogenic isotope abundances: one can calculate minimum exposure ages assuming zero erosion or calculate an erosion rate with an indeterminate age. It is also possible to adjust the minimum exposure ages for the erosion rate, but such ages become unstable for large minimum exposure ages. When minimum exposure ages are young, for example for a boulder that only recently released from the cliffs above, erosion rates are large, but generally the rock will be interpreted as young even after correcting for the erosion rate (because the erosion rate will be multiplied by a young age).

Table I-1. ^{10}Be concentrations, erosion rates, and exposure ages for the Castle Rock, Cholla, and SH95 study areas.

[DD, decimal degrees; m, meters; cm, centimeters, 10^3 atoms g^{-1}, million atoms ^{10}Be per gram of sample; ky, thousands of years; m/Myr, meters per million years]

Sample name	Latitude (DD)	Longitude (DD)	Elevation (m)	Thickness (cm)	Shielding correction[a]	[^{10}Be] (10^3 atoms g^{-1})[b]	Minimum exposure age (ky)[c]	Erosion rate (m/Myr)[d]	Preferred exposure age (ky)[e]
Castle Rock hillslope									
QA771	37.1640	-116.2788	1881	5	0.915	117 +/- 9	7.6 +/- 0.6	n/a	7.7 +/- 0.6
QA773	37.1641	-116.2799	1882	4	0.501	140 +/- 17	16 +/- 2	n/a	17 +/- 2
QA770	37.1609	-116.2791	1875	2	0.936	666 +/- 29	42 +/- 2	n/a	44 +/- 2
QA769	37.1649	-116.2793	1844	1	0.958	1016 +/- 36	64 +/- 2	n/a	69 +/- 3
QA772	37.1641	-116.2789	1882	4	0.579	942 +/- 32	97 +/- 3	n/a	110 +/- 4
QA768	37.1654	-116.2794	1817	5	0.979	1972 +/- 48	129 +/- 3	n/a	154 +/- 5
QA105	37.1640	-116.2802	1905	5	1.000	5098 +/- 121	322 +/- 8	2.2 +/- 0.1	n/a
QA767	37.1664	-116.2795	1811	3	0.997	7455 +/- 175	523 +/- 14	1.3 +/- 0.1	n/a
Cholla hillslope									
QA158	37.1503	-116.2647	1784	2	0.951	367 +/- 8	24 +/- 1	n/a	27 +/- 1
QA776	37.1502	-116.2649	1753	3	0.968	507 +/- 13	34 +/- 1	n/a	39 +/- 1
QA777	37.1501	-116.2650	1759	3	0.430	262 +/- 7	38 +/- 1	n/a	45 +/- 1
QA157	37.1501	-116.2648	1750	2	0.986	587 +/- 28	38 +/- 2	n/a	46 +/- 3
QA775	37.1503	-116.2649	1759	3	0.501	448 +/- 11	57 +/- 1	n/a	75 +/- 3
QA123	37.1502	-116.2645	1756	3	0.989	1535 +/- 36	101 +/- 2	n/a	217 +/- 15
QA774	37.1507	-116.2645	1734	4	0.996	1799 +/- 50	122 +/- 3	6.4 +/- 0.2	n/a
QA104	37.1504	-116.2650	1750	4	1.000	2062 +/- 40	138 +/- 3	5.6 +/- 0.1	n/a
SH95 hillslope									
QA798	36.7286	-116.6000	1017	5	0.997	285 +/- 9	32 +/- 1	n/a	34 +/- 1
QA799	36.7281	-116.6010	966	5	0.992	418 +/- 16	49 +/- 2	n/a	55 +/- 2
QA100	36.7309	-116.6018	906	2	0.962	401 +/- 12	50 +/- 1	n/a	56 +/- 2
QA797	36.7292	-116.6000	1021	5	0.998	526 +/- 16	59 +/- 2	n/a	68 +/- 2
071706D**	36.7262	-116.6020	864	5	0.998	997 +/- 24	128 +/- 3	n/a	187 +/- 7
QA101	36.7312	-116.6030	877	3	0.991	1072 +/- 26	135 +/- 3	n/a	204 +/- 8
071706A**	36.7262	-116.6020	864	5	0.998	1356 +/- 33	176 +/- 4	n/a	336 +/- 21
QA795	36.7280	-116.6023	835	5	0.987	1481 +/- 35	200 +/- 5	n/a	472 +/- 44
QA102	36.7309	-116.6029	877	3	0.992	1711 +/- 40	221 +/- 5	n/a	750 +/- 184
QA122	36.7309	-116.6004	959	2	1.000	1722 +/- 29	205 +/- 4	3.8 +/- 0.1	n/a
071706C-1**	36.7262	-116.6020	864	5	0.998	2187 +/- 53	292 +/- 8	2.6 +/- 0.1	n/a

[a]Ratio of the production rate at the shielded site to that for a 2π surface at the same location calculated using the CRONUS-Earth Geometric Shielding Calculator Version 1.1.

[b]Calculated using 07KNSTD ^{10}Be measurement standard and calibration (Nishiizumi et al, 2007).

[c]Model exposure age assuming no inheritance, zero erosion, density 2.2 g/cm^3, and standard atmosphere calculated using the CRONUS-Earth ^{10}Be - ^{26}Al exposure age calculator (Balco et al., 2008) Version 2.2 using a constant production rate model and scaling scheme for spallation of Lal (1991) / Stone (2000). This version of the CRONUS calculator uses a reference spallogenic ^{10}Be production rate of 4.49 ± 0.39 atoms g^{-1} yr^{-1} (± 1σ, SLHL) and muonogenic production after Heisinger et al. (2002a, b). The quoted uncertainty is the 1σ internal error, which reflects measurement uncertainty only.

[d]Erosion rate calculated using the same production parameters and scaling schemes and assuming that samples are near or at secular equalibrium.

[e]Exposure age calculated using the same method, except using the average erosion rate for each site (see text for details).

**Scoping samples (not included in QA data package).

Table I-2. ^{36}Cl concentrations, erosion rates, and exposure ages.

[DD, decimal degrees; m, meters, cm, centimeters, ky, thousands of years; m/Myr, meters per million years]

Sample name	Latitude (DD)	Longitude (DD)	Elevation (m)	Thickness (cm)	Shielding correction[a]	[^{36}Cl] (10^3 atoms g^{-1})[b]	Minimum exposure age (ky)[c]	Erosion rate (m/Myr)[d]	Preferred exposure age (ky)[e]
Southern precipitous cliff profile									
120507A	36.8296	-116.4687	1478	3	0.970	2707 +/- 48	130 +/- 24	n/a	160
120507B	36.8296	-116.4686	1480	4	0.966	2151 +/- 53	95 +/- 17	n/a	109
120507C	36.8294	-116.4686	1482	3	0.992	2261 +/- 44	101 +/- 18	n/a	117
QA778	36.8290	-116.4688	1455	2	0.983	2847 +/- 184	123 +/- 24	n/a	149
QA779	36.8289	-116.4687	1458	3	0.977	2333 +/- 149	102 +/- 19	n/a	119
QA114 UZN62#2	36.8300	-116.4674	1480	3	1.000	5418 +/- 351	286 +/- 68	2.1	n/a
Northern precipitous cliff and PBR "Nichole" site									
052008C	36.8548	-116.4666	1470	3	0.495	452 +/- 27	36 +/- 6	n/a	38
052008D	36.8548	-116.4666	1470	2	0.826	417 +/- 30	20 +/- 4	n/a	20
052008E	36.8548	-116.4666	1470	1.5	0.847	2504 +/- 78	141 +/- 26	n/a	178
052008F	36.8548	-116.4666	1470	2	0.453	2624 +/- 91	276 +/- 61	2.2	n/a
052008G	36.8548	-116.4666	1470	3.5	0.920	3639 +/- 90	186 +/- 37	n/a	262
052008H	36.8548	-116.4666	1470	4.5	0.856	2382 +/- 61	127 +/- 24	n/a	155
052008I	36.8548	-116.4666	1470	4	1.000	5128 +/- 127	274 +/- 58	2.2	n/a
PBR "Len" site									
QA159 120607F	36.8260	-116.4687	1418	3	0.481	752 +/- 47	58 +/- 11	n/a	63
120607C	36.8260	-116.4687	1418	2.5	0.568	952 +/- 36	73 +/- 13	n/a	80
120607D	36.8260	-116.4687	1418	6	0.404	821 +/- 30	70 +/- 12	n/a	77
120607E	36.8260	-116.4687	1418	8	0.497	1199 +/- 39	92 +/- 16	n/a	104
PBR "Matt's Cube" site									
051908A	36.8352	-116.4723	1372	1.5	0.898	1267 +/- 33	54 +/- 9	n/a	58
051908B	36.8352	-116.4723	1372	2.5	0.954	1984 +/- 63	76 +/- 13	n/a	84
051908C	36.8352	-116.4723	1372	1	0.659	1467 +/- 61	105 +/- 19	n/a	122
PBR "Tripod" site									
120607G	36.7802	-116.4709	1367	2.5	0.957	1818 +/- 58	61 +/- 66	n/a	66
120607H	36.7802	-116.4709	1367	3	0.981	1746 +/- 84	78 +/- 86	n/a	86
120607I	36.7802	-116.4709	1367	2	0.570	974 +/- 43	65 +/- 70	n/a	70
120607J	36.7802	-116.4709	1367	2.5	0.376	1243 +/- 35	98 +/- 113	n/a	113
PBR "Doozy" site									
102208A	36.8528	-116.4668	1466	9	0.500	511 +/- 27	39 +/- 7	n/a	41
102208B	36.8528	-116.4668	1466	5	0.976	2129 +/- 56	97 +/- 17	n/a	112
102208C	36.8528	-116.4668	1466	2.5	0.267	1070 +/- 40	94 +/- 17	n/a	108
DOOZY	36.8528	-116.4668	1466	2	0.750	1475 +/- 59	82 +/- 14	n/a	91
Mega-blocks on hillslope and pediment									
102108B	36.8534	-116.4699	1336	2.5	0.940	1459 +/- 105	60 +/- 11	n/a	65
102108C	36.8538	-116.4708	1323	6.5	0.354	1763 +/- 52	163 +/- 32	n/a	218
102108D	36.8573	-116.4690	1358	3	0.725	456 +/- 26	26 +/- 5	n/a	27
102108E	36.8576	-116.4690	1362	4	0.987	244 +/- 12	10 +/- 2	n/a	10
QA790	36.8578	-116.4694	1361	4	0.988	1103 +/- 71	49 +/- 9	n/a	52
102108F	36.8578	-116.4697	1350	5	0.987	4715 +/- 129	257 +/- 55	2.4	n/a
102108G	36.8577	-116.4697	1345	3.5	0.914	3443 +/- 66	244 +/- 52	2.6	n/a

[a]Ratio of the production rate at the shielded site to that for a 2π surface at the same location calculated using the CRONUS-Earth Geometric Shielding Calculator Version 1.1 (Balco et at., 2008).

[b]Calculated using the KNSTD1600 ^{36}Cl measurement standard and calibration with a ^{36}Cl/^{35}Cl ratio of 2.11 x 10^{-12} (Sharma et al, 1990).

[c]Model exposure age assuming no inheritance, zero erosion, density 2.2 g/cm^3, and standard atmosphere calculated using the exposure age calculation spreadsheet of Schimmelpfennig et al. (2009) using a constant production rate model and scaling scheme for spallation of Lal (1991) / Stone (2000). This calculator uses the spallogenic and muonogenic production rates in Schimmelpfinnig et al. (2009). The quoted uncertainty is the 1σ error, which reflects ^{36}Cl measurement and target element geochemistry uncertainties.

[d]Erosion rate calculated using the same production parameters and scaling schemes and assuming that samples are near or at secular equalibrium.

[e]Exposure age calculated using the same method, except using an erosion rate for 2 m/My.

Table I-3. Summary of intercomparison sample results showing ages calculated using ^{36}Cl in feldspar and ^{10}Be in quartz.

Sample name	^{36}Cl minimum exposure age (ky)[a]	^{10}Be minimum exposure age (ky)[a]
Castle Rock hillslope		
QA767	509 +/- 154	524 +/- 54
Cholla hillslope		
QA774	131 +/- 25	122 +/- 12
SH95 hillslope		
QA122 061808A	222 +/- 46	205 +/- 19
QA122-R*	230 +/- 48	
Coso site		
051908A	114 +/- 23	110 +/- 10

[a]Model exposure age assuming no inheritance, zero erosion, density 2.2 g/cm^3, and standard atmosphere using a constant production rate model and scaling scheme for spallation of Lal (1991) / Stone (2000). The quoted uncertainty is the 1σ error.
   *Replicate of QA122 061808A

^{10}Be Analytical Methods, Data-Reduction, and Exposure Age Calculations

Quartz mineral separates were extracted from the welded Ammonia Tanks Tuff for ^{10}Be analysis. Quartz purification and ^{10}Be extraction was completed at Lawrence Livermore National Laboratory (LLNL). Rock samples were crushed and sieved to 250–500 μm size fractions. Quartz was separated and meteoric ^{10}Be removed using methods described by Kohl and Nishiizumi (1992). The Be carriers used at LLNL are low-background carriers prepared from beryl with $2\pm2\times10^{-16}$ $^{10}Be/^9Be$ ratios. After adding Be carrier, quartz was dissolved in an HF/HN0$_3$ solution. The solution was dried down to

volatilize silicon fluorides, and fumed several times with $HClO_4$ to evaporate residual fluoride. Be was separated using ion exchange chromatography as described in Stone (2004) with anion exchange using HCl and cation exchange using dilute H_2SO_4 and HCl (Ditchburn and Whitehead, 1994). Be was then precipitated as beryllium hydroxide, ignited to beryllium oxide, mixed with niobium powder, and loaded into stainless steel cathodes prior to measurement.

The $^{10}Be/^9Be$ isotope ratios were measured at the Center for Accelerator Mass Spectrometry (CAMS) at LLNL. Process blanks were ~37,000±26,000 ^{10}Be atoms, 0.2 percent to 90.6 percent of the total number of ^{10}Be atoms in the samples. The 1-σ analytical uncertainties for $^{10}Be/^9Be$ ratios were 1.7–12.1 percent. Be isotope ratios were calibrated to the 07KNSTD3110 standard described in Nishiizumi and others (2007); samples normalized to 07KNSTD3110 use the revised nominal isotope ratio and revised ^{10}Be decay constant.

Exposure-age calculations were made with the CRONUS-Earth online exposure age calculator, Version 2.2, as described in Balco and others (2008) using a constant production rate model and the scaling scheme for spallation of Lal (1991) and Stone (2000). This version of the CRONUS calculator uses a reference spallogenic ^{10}Be production rate of 4.49±0.39 atoms g^{-1} yr^{-1} (±1σ, SLHL) and muonogenic production after Heisinger and others (2002a, b). Corrections for topographic shielding and surface geometry are 0–57 percent, calculated using the CRONUS-Earth online geometric shielding calculator, Version 1.1. Sample thickness corrections are all less than 4 percent. Corrections for snow cover should be insignificant and are not applied.

All model exposure ages assume zero inheritance for the sampled boulders. For model exposure ages, boulder ages are calculated both with and without a correction for boulder erosion. In the zero erosion rate calculation, the model ages can be interpreted as minimum exposure ages. For erosion corrected model ages, the boulder erosion rate for each hillslope is estimated using an average of the model erosion rates for a sample from (1) a stable bedrock exposure and (2) the oldest boulder. This method of correcting for boulder erosion assumes that these two samples are near or at secular equilibrium, which is supported by the observation that at each site the oldest boulder and bedrock exposure have similar ^{10}Be nuclide concentrations. Sample information, ^{10}Be concentrations, model exposure ages, and model erosion rates are summarized in table I-1.

^{36}Cl Analytical Methods and Data Reduction

Alkali feldspar mineral separates were extracted from welded tuffs of (1) the Tiva Canyon and Topopah Spring Tuffs at Yucca Mountain and (2) the Ammonia Tanks Tuff. Feldspar mineral separation was completed at the U.S. Geological Survey in Menlo Park and LLNL. Feldspar purification and ^{36}Cl extraction was completed at the CEREGE laboratory in France and LLNL. Rock samples were crushed and sieved to 250–500 µm size fractions. Feldspar was separated using conventional magnetic and density separation techniques. Geochemical analyzes were performed by SGS Mineral Services (Toronto). Whole rock geochemistry was measured by x-ray fluorescence (XRF), inductively coupled plasma mass spectrometry (ICP-MS), and inductively coupled plasma optical emission mass spectrometry (ICP-OES). Mineral separate geochemistry was measured on 0.5-gram (g) feldspar aliquots by ICP-OES with assumed 5 percent uncertainties. Rock densities are estimated at 2.2 g cm^3 based on USGS data from the UZ-N62 and SD-12 borehole cores from Yucca Mountain; measurements were reported by L.E. Flint, U.S. Geological Survey Hydrologic Research Facility (data tacking number GS950308312231.002).

Mineral purification and ^{36}Cl extraction was performed using methods described by Schimmelpfennig and others (2009). The Cl spikes used at CEREGE and LLNL are 99.9 percent^{35}Cl from Oak Ridge National Laboratory. After adding Cl carrier, feldspar was dissolved in a $HF/HN0_3$

solution. AgCl was precipitated with $AgNO_3$, and the AgCl was dissolved in NH_4OH. Sulfur was removed by adding $Ba(NO_3)_2$ to the solution to precipitate $BaSO_4$ and $BaCO_3$. The remaining solution was acidified with HNO_3 to reprecipitate AgCl. The final AgCl was washed, dried, and loaded into AgBr-lined stainless steel cathodes prior to measurement.

The ^{35}Cl, ^{36}Cl, and ^{37}Cl isotope measurements were performed at the Center for CAMS using the high-intensity LLNL-modified Middleton cesium sputter source in combination with the CAMS FN mass spectrometer operating at 8.3 megavolts (MV). $^{36}Cl/^{35}Cl$ ratios were normalized to K. Nishiizumi's KNSTD1600 ^{36}Cl standard of 2.11×10^{-12} (Sharma and others, 1990). The $^{35}Cl/^{37}Cl$ ratio was normalized to the same standard assuming a natural stable isotopic ratio of 3.127. Measured ratios and ^{36}Cl concentrations are reported in table I-2. The 1-σ analytical uncertainties for $^{36}Cl/^{35}Cl$ ratios were between 1.7 and 7.2 percent. Process blanks had approximately $100,000 \pm 200,000$ ^{36}Cl atoms, which is about 0.8–26.9 percent of the total number of ^{36}Cl atoms in the samples. The Cl concentrations in the feldspar mineral separates ranged from about 1 to 17 ppm. Bulk rock Cl concentrations were assumed to be 170 ppm based on data from Peterman and Cloke (2002).

^{36}Cl Exposure Age Calculations

Exposure-age calculations were made as described in and using the ^{36}Cl age calculation spreadsheet of Schimmelpfennig and others (2009). Ages are calculated using a constant-production-rate model and scaling scheme of Lal (1991) and Stone (2000). Production rates and equations are reported in Schimmelpfennig and others (2009). ^{36}Cl atoms produced by spallation reactions on target elements account for 95–98 percent of the total ^{36}Cl atoms in the samples; therefore 71–95 percent of the ^{36}Cl atoms in samples are produced by spallation on potassium alone. Corrections for topographic shielding and surface geometry are 0–73 percent, calculated using the CRONUS-Earth online geometric shielding calculator, Version 1.1 (Balco and others, 2008). Sample thickness corrections are generally less than 5 percent. Corrections for snow cover should be insignificant and are not applied.

All model exposure ages assume zero inheritance for the sampled boulders. For model exposure ages, boulder ages are calculated both with and without a correction for boulder erosion. In the zero erosion rate calculation, the model ages can be interpreted as minimum exposure ages. For erosion-corrected model ages, the boulder erosion rate is estimated using the model erosion rates for samples from (1) stable bedrock exposures on Yucca Mountain crest and (2) the oldest boulders on the northwestern slope of Yucca Mountain. This method of correcting for boulder erosion assumes that these samples are near or at secular equilibrium, which is supported by the observation that the oldest boulders and bedrock exposures have similar ^{36}Cl nuclide concentrations. The secular equilibrium value represents the maximum ^{36}Cl concentration that can be achieved in a sample given an erosion rate, site/sample production rate, and radioactive decay half-life (300 ky for ^{36}Cl). Because the sample production rate and half-life are known or can be independently estimated, the secular equilibrium value can be used to calculate an average erosion rate over relatively long timescales, which is more than 250 ky using ^{36}Cl at Yucca Mountain. Sample information, ^{36}Cl concentrations, model exposure ages, and model erosion rates are summarized in table I-2. Table I-3 compares the minimum ^{10}Be and ^{36}Cl ages calculated using the same scaling scheme for coexisting quartz and feldspar, respectively.

References

Balco, G., Stone, J.O., Lifton, N.A. and Dunai, T.J., 2008, A complete and easily accessible means of calculating surface exposure ages or erosion rates from ^{10}Be and ^{26}Al measurements: Quaternary Geochronology, v.3, no. 3, p. 174–195.

Ditchburn R.G., and Whitehead N.E., 1994, The separation of ^{10}Be from silicates: 3d Workshop of the South Pacific Environmental Radioactivity Association, p. 4–7.

Flint, L.E., 1998, Matrix properties of hydrogeologic units at Yucca Mountain, Nevada: U.S. Geological Survey Water-Resources Investigations Report 97–4243, 64 p., *http://pubs.er.usgs.gov/publication/wri974243/*.

Heisinger, B., Lal, D., Jull, A.J.T., Kubik, P.W., Ivy-Ochs, S., Neumaier, S., Knie, K., Lazarev, V., and Nolte, E., 2002a, Production of selected cosmogenic radionuclides by muons—1. Fast muons: Earth and Planetary Science Letters, v. 200, p. 357–369.

Heisinger, B., Lal, D., Jull, A.J.T., Kubik, P.W., Ivy-Ochs, S., Knie, K., Nolte, E., 2002b, Production of selected cosmogenic radionuclides by muons—2. Capture of negative muons: Earth and Planetary Science Letters, v. 200, p. 357–369.

Kohl, C.P., Nishiizumi, K., 1992, Chemical isolation of quartz for measurement of in situ-produced cosmogenic nuclides: Geochimica et Cosmochimica Acta, v. 56, p. 3583–3587.

Lal, D., 1991, Cosmic ray labeling of erosion surfaces—in situ nuclide production rates and erosion models: Earth and Planetary Science Letters, v. 104, nos. 2–4, p. 424–439.

Nishiizumi, K., Imamura, M., Caffee, M., Southon, J., Finkel, R., and McAnich, J., 2007, Absolute calibration of ^{10}Be AMS standards: Nuclear Instruments and Methods in Physics Research, v. B 258, p. 403–413.

Peterman, Z., and Cloke, P., 2002, Geochemistry of rock units at the potential repository level, Yucca Mountain, Nevada: Applied Geochemistry, v. 17, no. 6, p. 683–698.

Schimmelpfennig, I., Benedetti, L., Finkel, R., Pik, R., Blard, P.-H., Bourlès, D., Burnard, P., and Williams, A., 2009, Sources of in-situ ^{36}Cl in basaltic rocks— implications for calibration of production rates: Quaternary Geochronology, v. 4, no. 6, p. 441–461.

Sharma, P., Kubik, P.W., Fehn, U., Gove, H.E., Nishiizumi, K., Elmore, D., 1990, Development of ^{36}Cl standards for AMS: Nuclear Instruments and Methods in Physics Research Section B, v. 52, p. 410–415.

Stone, J., 2004, Extraction of Al and Be from quartz for isotopic analysis: Seattle, University of Washington, UW Cosmogenic Nuclide Lab Methods and Procedures, available at http://depts.washington.edu/cosmolab/chem.html.

Stone, J.O., 2000, Air pressure and cosmogenic isotope production: Journal of Geophysical Research, v. 105, no. b10, p. 23753–23759.

Appendix II. Erosion-Rate Estimates from Detritus Volumes on the West Face of Yucca Mountain

Figure II-1 below outlines the areas in which Susan Buckingham (then at University of Colorado, Boulder) made the boulder-volume counts on the west face of Yucca Mountain. The Yucca Mountain crest is shown as a solid black line, and each area below it (in green) is divided into an upper, steep-slope area (on which only a thin veneer of cobbles, gravels, and fines reside on bedrock) and a lower, low-slope area on which several meters of alluvium derived from upslope reside. Table II-1 it gives the along-strike (of the Yucca Mountain crest) width (in meters, m) for each of these eight "pediments," the total area (in square meters, m^2) for each of them, and the areas (m^2) for just the lower parts.

Table II-2 gives the volumes (in cubic meters, m^3) of boulders and ground cover (rock fragments probably mobile to down-slope movement). The "South Ravine" column in table II-2 tabulates the volume of these materials in the washes that divide the pediments; volumes in the ravine that form the south boundary of a pediment segment are added to that pediment.

Table II-3 calculates for several time intervals the volume of material released for the given width of each pediment, assuming the Tiva Canyon Tuff along the Yucca Mountain crest releases boulders approximately equivalent to a retreat rate of 1 m/100 ka through its 10-m thickness.

The total boulder/fragment volume for all eight pediments is 3,327 m^3 (Table II-2), only 47 percent of the expected volume of 7,070 m^3 for 100,000 years (Table II-3), and becomes a progressively smaller number with greater age.

Figure II-2 shows the shattered cliffs of Rickey Ridge, losing 2 to 4 m of the cliff face at the time of UNE Rickey.

Figure II-3 is a photograph of the track of a boulder recently released from the Yucca Mountain crest.

Figure 9*A* shows both the "block-by-block" and "grain-by-grain" erosion mechanisms operating on the Tiva Canyon Tuff on the Yucca Mountain crest, looking north. In-place weathering is occurring on the rocks to the left of the vertical cooling joint.
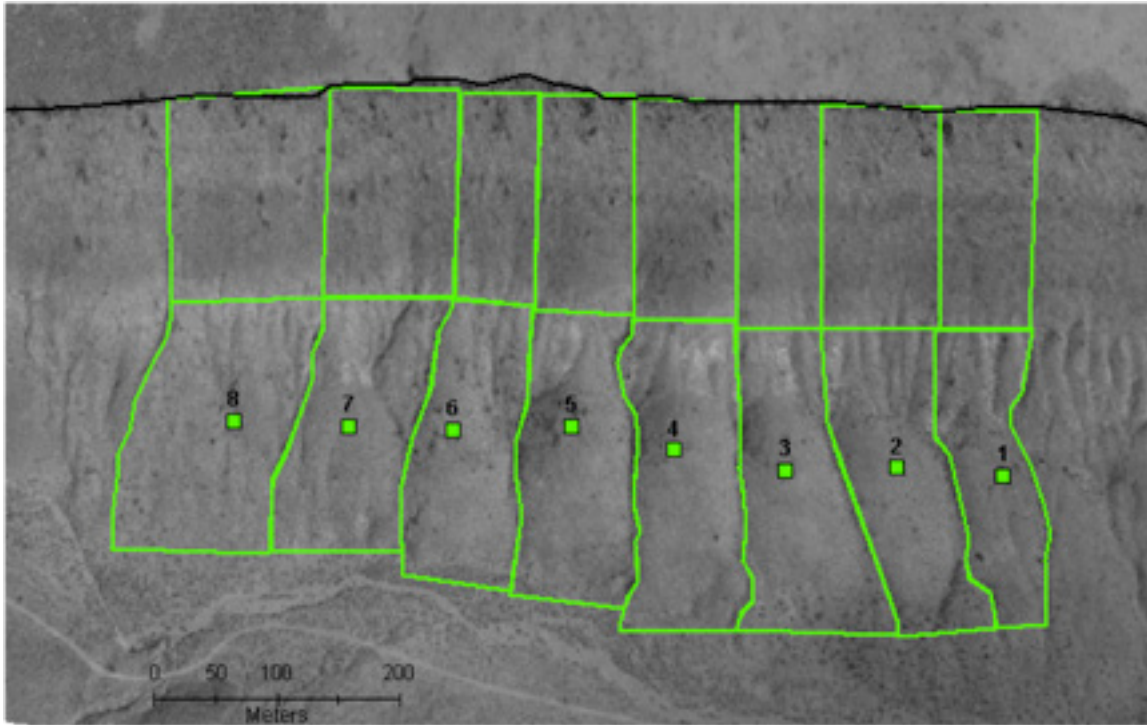
Figure II-1. Aerial photo showing the boulder count study areas on the west face of Yucca Mountain in Solitario Canyon, looking down on much the same view as fig 12. Shown in green are the boundaries of eight areas in which boulders were counted.

Table II-1. Widths and areas for pediments shown in figure II-1.

Pediment	8	7	6	5	4	3	2	1	Total
GIS Width (m)	130	106	64	79	82	70	97	79	707 m
Total Calculated Area	52013	41669	52508	59740	62068	59424	62524	31830	421,776 m^2
Area of lower slope	26307	21137	44088	40313	45561	45147	42915	15860	281,329 m^2

Table II-2. Individual pediment and total volume calculation for the Yucca Mountain hill slope study.

	Square Area	Boulder	Ground Cover	South Ravine	Total
Pediment 1	15,860	253.50	111.02	85.00	449.52
Pediment 2	42,915	85.50	51.50	45.00	182.00
Pediment 3	45,147	105.64	54.18	44.29	204.10
Pediment 4	45,561	56.00	54.67	25.00	135.67
Pediment 5	44,088	163.80	220.44	85.00	469.24
Pediment 6	40,313	331.26	201.57	150.00	682.83
Pediment 7	21,137	254.80	105.68	85.00	445.48
Pediment 8	26,307	542.00	131.53	85.00	758.53
				Total	3,327.38

Table II-3. Calculated boulder volumes for the 8 pediments.

Potential boulder volume	Pediment 8	Pediment 7	Pediment 6	Pediment 5	Pediment 4	Pediment 3	Pediment 2	Pediment 1	Total (m³)
100,000 years	1,300	1,060	640	790	820	700	970	790	7,070
200,000 years	2,600	2,120	1,280	1,580	1,640	1,400	1,940	1,580	14,140
300,000 years	3,900	3,180	1,920	2,370	2,460	2,100	2,910	2,370	21,210

Figure II-2. Photo of the shattered cliffs at Rickey Ridge, which lost 2 to 4 m of cliff face as a result of the underground nuclear explosion Rickey. Photo by J.W. Whitney.

Figure II-3. Photograph taken shortly after a boulder released from the Yucca Mountain crest (white area on skyline). The downslope trajectory of the boulder is indicated by the whitish divots left on the hill slope. The boulder, or what is left of it, is the white, angular slab in the lower left. Note white fragments of boulder left along or near the boulder track. Photo by J.W. Whitney in July 2009.

Appendix III. Fragility Data and Calculations for the Lithophysal Units

1.0   Introduction

The Yucca Mountain Project (YMP) has developed a bounded horizontal PGV hazard curve based on physical limits to the amplitude of ground motions (BSC, 2005). The ground motions propagating through the geological units at Yucca Mountain will induce shearing-strains. If these shearing-strains exceed the capacity of the rock mass, geologically-observable fracturing and other forms of damage will occur. In particular, the repository host horizon (the Topopah Spring densely-welded tuff formation) consists of distinct, horizontally layered, nonlithophysal and lithophysal subunits that are roughly 12.8 million years old[7]. The lithophysal units contain open voids (lithophysal cavities) with diameters of 10 cm to over a meter, and spacings of about 10 to 50 cm. The total lithophysal porosity of these subunits is approximately 20 percent of their volume. The physical characteristics of the lithophysae have been studied in detail via development of a significant number of 3m x 1m geological panel maps created along the ECRB tunnel that transects all the repository subunits. These maps indicate that no discernible physical damage from stressing or shaking has occurred in the lithophysae or the matrix groundmass between them in the roughly 12.8 million years since they were deposited. The approximate "threshold" shear-strain required to have caused observable deformation or collapse of lithophysal voids, or fracturing of the matrix between voids, has been estimated from laboratory compression testing of large-diameter (288 mm) lithophysal cores as well as calibrated discrete element numerical simulations which model fracture of the lithophysal unit in response to stress. Since damage is not observed in the repository units, the threshold shear-strain defines an unexceeded shear-strain level at Yucca Mountain. Stochastic site response modeling of ground motions at Yucca Mountain is used to define the probabilistic distribution of horizontal PGV (as well as the shear-strain) at repository depth for a range of input material properties and potential earthquakes. By relating the calculated PGV (and shear-strain) to the threshold shear-strain defined from the laboratory testing and discrete element modeling, unexceeded horizontal PGV at Yucca Mountain can be determined. This bounded horizontal PGV is used to develop a bounded PGV hazard curve, which is then compared to the unbounded curve defined from past PSHA analyses conducted in the 1990s.

2.0   Geology of the YMP Repository Host Rock Mass

2.1   Topopah Spring Formation

The proposed repository at Yucca Mountain is to be excavated in the silica-rich, densely welded, pyroclastic-flow units of the Topopah Spring Tuff Formation, which are approximately 12.8 million years old (Sawyer and others, 1994). In the densely welded and crystallized rocks of the Topopah Spring Tuff, the flow can be subdivided into distinct zones that are highly laterally continuous. The zones are often identified on the basis of the abundance, size, and distribution (or lack thereof) of lithophysae. Lithophysae are cavities in the rock formed during the welding process as a result of accumulation of exolved vapor-phase gasses. The Topopah Spring Formation has been subdivided into four subunits based on the presence of lithophysae. These are termed, in order of depth (fig.III-1): the Upper Lithophysal (Tptpul), the Middle Nonlithophysal (Tptpmn), the Lower Lithophysal (Tptpll), and the Lower Nonlithophysal (Tptpln) zones. Each of these zones is extensively exposed and geologically mapped in the Exploratory Studies Facility (ESF) and Enhanced Characterization of the Repository

---

[7] Lithophysae are cavities (from 10 cm to over a meter in dimension) formed by exsolution of gas during the cooling process.

Block (ECRB) tunnels excavated by tunnel boring machine within Yucca Mountain in the 1990s. In the proposed repository layout (BSC, 2004a), approximately 85 percent of the emplacement tunnels are excavated within the lithophysal tuff and 15 percent within the nonlithophysal tuffs of the Topopah Spring Formation. The majority of the repository is to be located in the Tptpll unit from about 250 to 300m depth below ground surface.
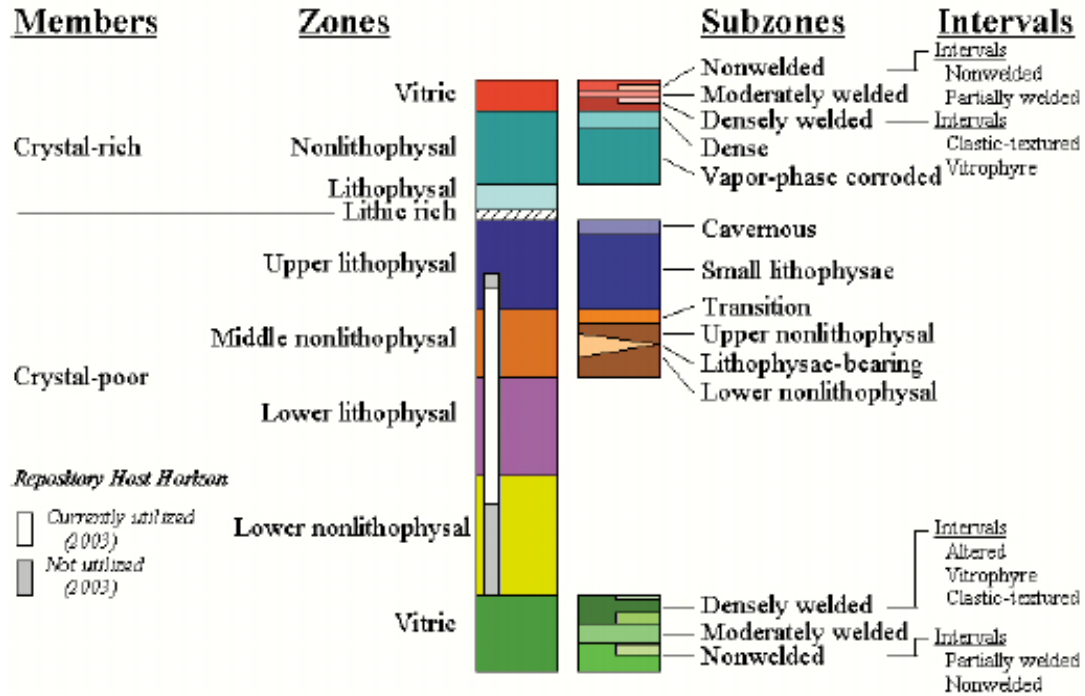
Figure III-1.   Diagram of lithostratigraphic units of the Topopah Spring Tuff. From Case and Buesch (2004).

2.2   Nonlithophysal Subunits of the Topopah Spring Formation

All of the units are composed of the same silica-rich rhyolitic groundmass, which has intergranular porosity of less than 1 percent. The nonlithophysal Tptpmn and Tptpln units are characterized by lithophysal cavities of less than about 3 percent volume and have several sets of cooling-related fractures. These fractures have relatively short continuous trace lengths, and often terminate in solid rock or against another joint set (BSC, 2004a). The result is a highly interlocked rock mass with abundant solid rock "bridges" between fractures. Fractures typically have curved surfaces with little occurrence of post deposition offset of the opposing surfaces. A widely spaced set of flat-dipping, vapor-phase altered fractures also is typically seen with trace lengths that can be 3m or greater in length. These fractures (fig. III-2) are typically strong due to the presence of vapor phase minerals along their surfaces.

Figure III-2. Photo showing typical fracturing in the Middle Nonlithophysal (Tptpmn) subunit. Mapping of fractures included definition of fracture terminations and continuity (indicated by painted lines with arrowheads).

2.3   Lithophysal Subunits of the Topopah Spring Formation

The lithophysal subunits (the Tptpul and Tptpll) are composed of the same silica-rich groundmass as the nonlithophysal units, but contain lithophysal cavities that make up roughly 10 to 30 percent of the rock mass volume. Average lithophysal volume in the Tptpll, the primary repository unit, is about 20 percent. Although the porosity and stratigraphic position of the lithophysae are consistent within each subunit, the character of the lithophysal cavities and matrix fracturing between the two subunits varies significantly. In particular, lithophysae in the Tptpul tend to be roughly spherical and uniform in size and distribution with diameter of 1 to 10 cm, and the matrix material is largely unfractured. In the Tptpll, the lithophysae shape, size and distribution is irregular in nature (fig. III-3). Lithophysae range in size from about 1 cm to nearly 2 m in dimension and have spacing that ranges from about 10 to 50 cm, but may be more closely spaced in local regions. The shapes range from elliptical or spherical to irregular, cuspate and merged cross sections, or elongate along fractures. The matrix between lithophysae often has a fabric of short length (<1m) and discontinuous cooling fractures that have a primary vertical orientation. These fractures typically are not interconnected and do not intersect lithophysal cavities.

The lithophysae and fracture characteristics within the lithophysal units were described in detail via the development of a large number of 3m x1m geological panel maps along the walls of the ECRB exploration drift that cuts down through all of the Topopah Spring subunits. As described in BSC (2005), 1,444 lithophysae were inspected in these panel maps. Only 7 are transected (or intersected) by these discontinuous cooling fractures that have trace length greater than 1 m, and only 5 are transected by shear fractures. Although a few lithophysae are transected by fractures, are the terminal end of fractures, or occur along shears, none have appreciable effects of damage to the walls of the lithophysae. It is concluded in BSC (2005) that none of the lithophysae observed have been damaged, offset or collapsed by shearing as the result of extreme ground motions.
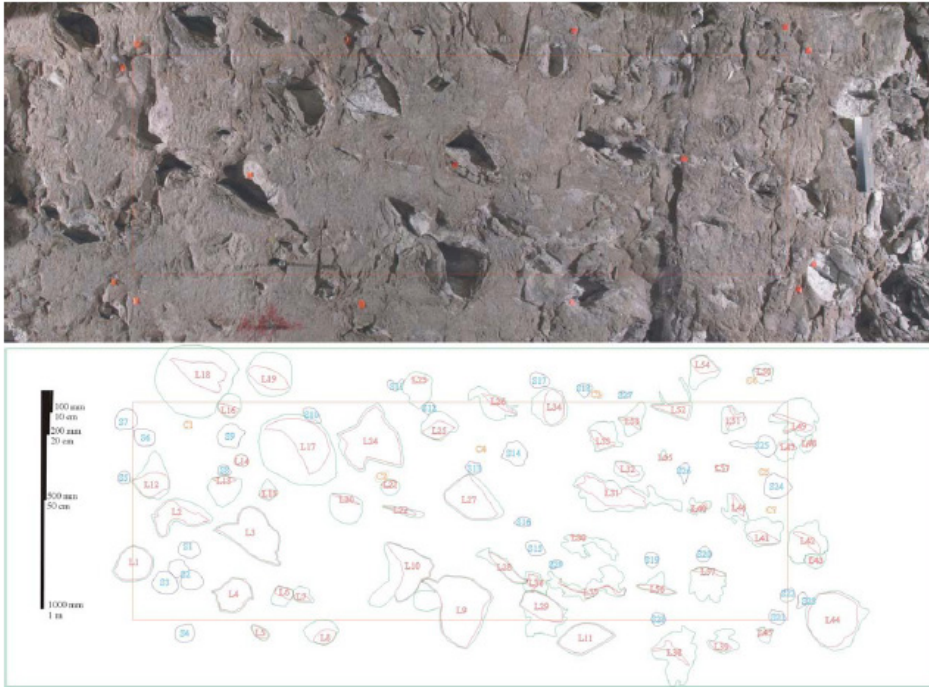
NOTE: Lithophysae have red "L" identifiers with cavities outlined in red and rims in green. Spots have blue "S" identifiers with cyan outlines. Lithic clasts have orange "C" identifiers with gold outlines.

Figure III-3. Panel map (3mx1m) at 14+93 along Enhanced Characterization of the Repository Block tunnel sidewall in the lower lithophysal unit of the Topopah Springs Tuff showing trace map of lithophysal cavities, including the vapor phase alteration that typically rims the cavity surface. Lithophysae have red "L" identifiers with cavities outlined in red and rims in green. Spots have blue "S" identifiers with cyan outlines. Lithic clasts have orange "C" identifiers with gold outlines.

3.0   Use of Lithophysae and Tptpll Fracture Fabric as a Marker for Extreme Ground Motion

3.1   Introduction

The probabilistic seismic hazard assessment (PSHA) process conducted in the 1990s at YMP produced possible extreme ground motions characterized by PGV levels in excess of 4 m/s at the repository emplacement level for the regulatory requirement of annual frequencies of exceedance of as low as 10^{-8}/yr. These extreme PGV levels may be physically unrealizable (for example, Reiter, 2004) as the amplitude of the ground motion traveling through a rock mass is limited by the shear strength of the rock mass through which it propagates. YMP staff theorized that damage resulting from extreme ground motions would potentially be easily observable in the Yucca Mountain rock units. In particular, the lithophysal subunits of the densely welded tuff units may provide relatively sensitive marker units in which shearing damage to the lithophysal cavities could be easily observed in the exploration tunnels driven through them. Damage could include potential crushing of voids, ubiquitous seismically induced shear fracturing between voids, shear displacement offset on cooling fractures that transect cavities, and so on. The absence of any apparent damage to the lithophysal subunits could supply an unexceeded or bounding level of ground motion, as long as a relationship between the shear-strain induced by a given PGV at the lithophysal horizon could be related to the threshold shear-strain resulting in observable damage.

3.2 Approach to Establishing Unexceeded Shear-Strains

The process for estimating a bound to the horizontal PGV at the repository horizon involves use of laboratory strength testing of large cores of lithophysal and nonlithophysal rock, geological observations of lack of damage to the in situ lithophysal rock mass, and ground motion site response predictions. Four analysis steps were performed (BSC, 2005):

- The laboratory strength tests, combined with discrete element numerical simulations of lithophysal rock define the shear strain threshold for observable lithophysal rock mass damage.
- The results of the numerical simulations are used to define the type of damage that should be observable, in situ, if the rock mass were subjected to threshold shearing strains. The geological data, summarized in the previous section, was used to establish that the Topopah Spring lithophysal subunits have not experienced shear strains exceeding the damage threshold.
- Ground motion site response models are used to assess the level of horizontal PGV that would be required to generate shear strains exceeding the shear strain damage threshold.
- Finally, it is concluded that the damage threshold PGV has not been reached at Yucca Mountain since the rocks were deposited 12.8 million years ago. This PGV is then assumed to be a reasonable bound or unexceeded ground motion level.

3.2.1 Laboratory Strength Testing

The elastic properties and compressive strength of lithophysal rock is dependent up on the percent of lithophysal porosity (BSC, 2004a). To establish these properties, a series of uniaxial compression tests were conducted on large (288 mm diameter) core samples taken from the Tptpll and Tptpul units. In total, 19 samples[8] were tested at dry, saturated, room temperature and elevated temperatures (table III-1). A typical stress-strain curve for a sample of Tptpll is given in figure III-4. As seen in this plot, initial nonlinearity (the result of seating of the platens and microcrack closure), is followed by an elastic response, and initiation of failure at the departure from linear behavior at Point A (>80 percent of peak load), active failure and macroscopic damage at Point B, and peak stress capacity at Point C. Macrofracturing is likely visible at the initiation of failure at Point A, and visible interlithophysal fracturing is visible at Point B. The primary failure mode observed in samples after testing is development of new fractures between lithophysal cavities, which eventually form fractures that interconnect multiple lithophysae and intersect sample boundaries. It is noted that the laboratory tests are conducted on unstressed samples. In the actual case, the rock in the lithophysal units has been at significant depth (approximately 250–300 m) approximately since their original deposition. Therefore, the rock mass subjected to ground motion during geologic history has been at significant triaxial stress conditions and thus initial strain as shown in Figure 4, which must be accounted for in the incremental shear-strain at failure calculation as described in the next section.

3.2.2 Estimation of Mean Shear Strain at Failure

The details of the methodology used to estimate the mean shear-strain at failure for lithophysal rock is described in BSC (2005), section B.2.2. The limiting or failure state of lithophysal rock is defined by a Mohr-Coulomb condition, which is defined by the rock mass friction angle (φ) and a cohesion factor (c). The "friction angle" in this context characterizes how the limiting state changes as a function of confining stress. It is assumed that the friction angle for the limiting state is the same as the friction angle related to the yield criterion (or peak stress). In the elastic state, the material is

---

[8] Typically, it was estimated that the diameter of the sample was at least 5 times the diameters of lithophysae in the sample, thus producing results reasonably representative of in situ conditions.

characterized by a Young's Modulus (*E)* and a Poisson's ratio (v). It is assumed that the lithophysal rock mass behaves as a linear elastic material until the limiting state is reached. The stress path from the initial stress state to the limiting damage state during a strong seismic ground motion can be arbitrary. In this analysis, the shear-strain increment is calculated for the stress path in which the mean stress does not change. Cyclic shear strain under constant vertical stress, which is typically a dominant mode of deformation during a seismic ground motion, results in the stress path along which the mean stress is invariant. The shear-strain increment can be determined from simple geometric construction from the Mohr-Coulomb yield function in principal stress space and from Hoek's Law (BSC, 2005, section B.2.2). The input material properties required to estimate the peak shear strain include Young's modulus, Poisson's ratio, friction angle, yield stress, and peak stress are taken from laboratory tests, numerical simulations, or assumed, as appropriate.

The resulting estimates of shear-strain at failure for all laboratory tests are given in figure III-5, and are grouped for samples that have a length to diameter ratio (L:D) of less than and greater than 1.5.[9] The mean shear-strain at failure for L:D>1.5 is 0.16 percent with no obvious relationship to sample porosity due to the lithophysae. The upper and lower bounds of the probability distribution of shear-strain at failure used in estimating the bounding PGV are indicated by the dashed lines in figure III-5 (section 4).

---

[9] An L:D ratio of 2 or more is preferred, however, obtaining large core samples of this length proved quite difficult in the lithophysal material, so samples with shorter lengths were also tested.

Table III-1. Lithophysal Rock Mass Properties Estimated from Large Core Testing in Yucca Mountain.

Test ID	Lithostratigraphic Unit	L:D Ratio[a]	Saturation	Temperature (C)	Ultimate Strength (MPa)	Young's Modulus (GPa)	Poisson's Ratio	Estimated Lithophysal Porosity[b]	Source DTN[c]
YMPLL49A	Tptpll	1.1 : 1	Dry	195	32.2	7.1	—	11.7	SN0211L0207502.002
YMPLL43A	Tptpll	1.1 : 1	Dry	200	31.1	6.5	—	20.3	SN0211L0207502.002
YMPLL23A	Tptpll	1.8 : 1	Room Dry	24	28.7	9.2	—	19.2	SN0211L0207502.002
YMPLL24A	Tptpll	1.8 : 1	Room Dry	24	13.3	5.0	—	22.2	SN0211L0207502.002
YMPLL46A	Tptpll	1.8 : 1	Room Dry	24	21.7	8.5	—	28.4	SN0211L0207502.002
YMPLL87A	Tptpll	1.9 : 1	Saturated	24	15.7	5.3	—	14.5	SN0211L0207502.002
YMPUL59B	Tptpul	1.2 : 1	Dry	190	19.6	7.3	—	39.4	SN0208L0207502.001
YMPUL67A	Tptpul	1.3 : 1	Dry	190	34.8	9.9	—	6.2	SN0208L0207502.001
YMPUL62B	Tptpul	1.0 : 1	Dry	200	37.0	13.7	—	19.3	SN0208L0207502.001
YMPUL50A	Tptpul	1.5 : 1	Room Dry	24	22.1	14.9	0.21	28.5	SN0211L0207502.002
YMPUL59A	Tptpul	2.0 : 1	Room Dry	24	13.5	5.8	0.39	30.3	SN0208L0207502.001
YMPUL61A	Tptpul	1.9 : 1	Room Dry	24	17.7	8.8	—	23.9	SN0208L0207502.001
YMPUL62A	Tptpul	1.8 : 1	Room Dry	24	25.9	13.7	—	12.7	SN0208L0207502.001
YMPUL64A	Tptpul	1.7 : 1	Room Dry	24	33.5	20.5	—	12.8	SN0208L0207502.001
YMPUL65A	Tptpul	2.0 : 1	Room Dry	24	26.2	19.5	—	11.9	SN0208L0207502.001
YMPUL66A	Tptpul	1.7 : 1	Room Dry	24	16.5	12.4	—	16.7	SN0208L0207502.001
YMPUL60A	Tptpul	1.8 : 1	Saturated	24	12.7	6.7	—	18.6	SN0208L0207502.001
YMPUL63A	Tptpul	1.9 : 1	Saturated	24	9.4	5.0	0.24	20.0	SN0208L0207502.001
YMPUL68A	Tptpul	2.1 : 1	Saturated	24	11.6	5.9	0.03	25.8	SN0208L0207502.001

[a] Specimen length-to-diameter ratio.
[b] Lithophysal property data for tests documented in DTNs SN0208L0207502.001 [DIRS 161871] and
  SN0211L0207502.002 [DIRS 161872] are provided by DTN SN0305L0207502.005 [DIRS 163373].
[c] DTN SN0208L0207502.001 has DIRS number 161871 and DTN SN0211L0207502.002 has DIRS number 161872.

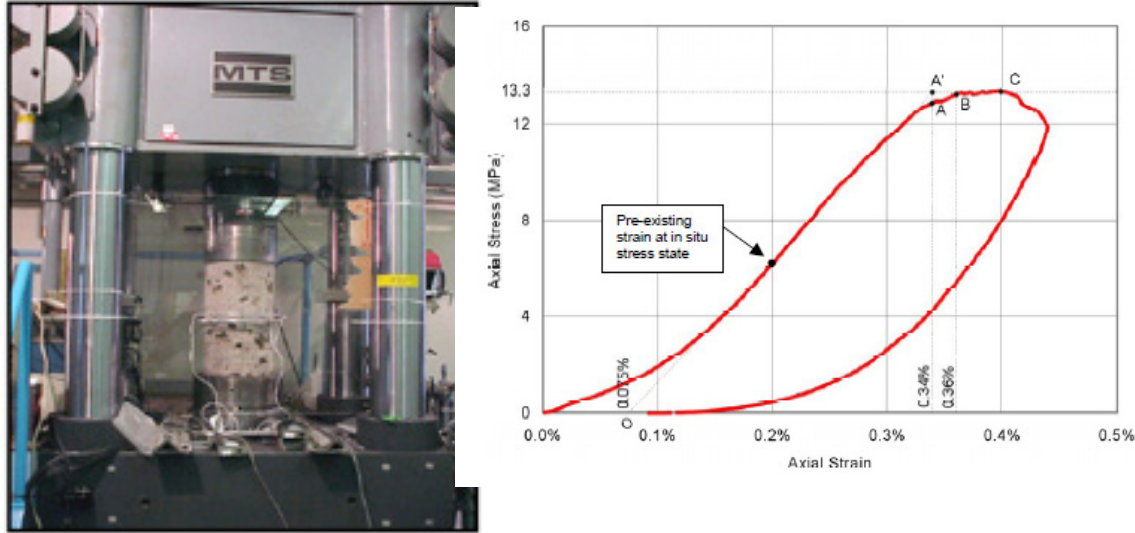Source: BSC (2004 [DIRS 172334], Table 6.3-1).

Figure III-4. Left, photograph of laboratory uniaxial compression testing set-up for 288 mm-diameter lithophysal tuff samples. Right, plot of typical stress-strain response. Peak strength and modulus of lithophysal tuff is lithophysal-porosity dependent. Source: DTN: SN0211L0207502.002 [DIRS161872]. Price (2002 [172061], p. 207–215).
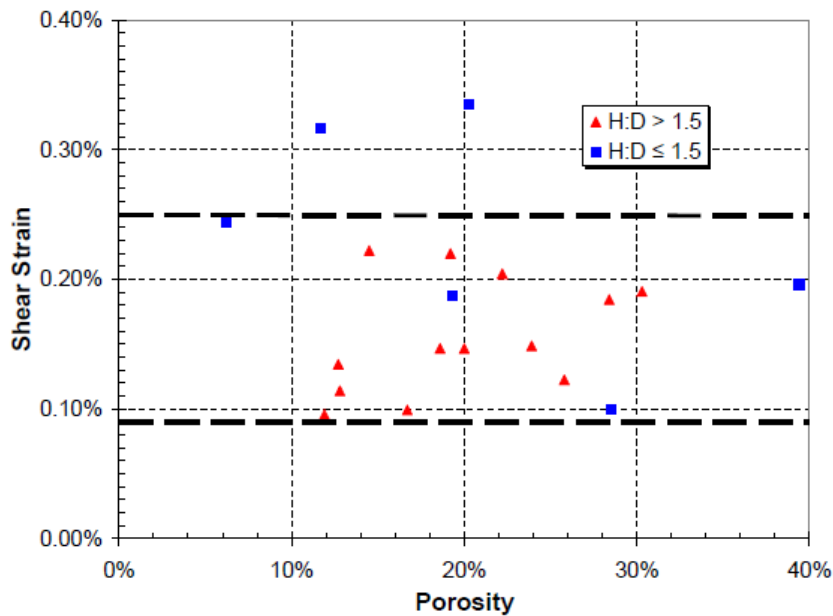
Figure III-5. Plot showing shear strain at failure as a function of lithophysal porosity estimated from large core testing. Shear-strain increments shown are calculated for an overburden depth of 2250m. For this case, the mean shear-strain increment for all 288mm diametersamples is 0.18%. For the samples having ratio L/D>1.5, which are considered the best representation of the mechanical behavior of lithophysal rock, the mean shear-strain increment is 0.16%. The bold horizontal dashed lines indicate the upper and lower bound of the shear strain threshold probability distribution. From BSC (2005), figure 6-5.

3.2.3 Threshold Shear Strain Distribution

The results of laboratory testing, supplemented by numerical simulations of lithophysal rock compression (described in section 3.3), are used to conduct an assessment of the shear-strain level (termed "threshold shear strain") required to result in geologicallyobservable damage. Epistemic uncertainty in the assessment of the threshold shear-strain is represented by the triangular probability distribution in figure III-6. The mode of the distribution is 0.16 percent strain, which is the mean of the testing data for the 288 mm-diameter samples with height-to-diameter ratio H:D>1.5 (table III-1). This value also is consistent with the mean estimates based on the PFC2D numerical simulations (described in the next section), which range from about 0.13 to 0.18 percent (BSC, 2005, table 6-2). The lower limit of the triangular distribution lies at 0.09 percent strain, which bounds the shear-strain increments for the 288 mm-diameter laboratory test data (fig. III-5). The upper limit of the distribution lies at 0.25 percent, which bounds most of the shear strain limits from the laboratory tests (fig. III-5).
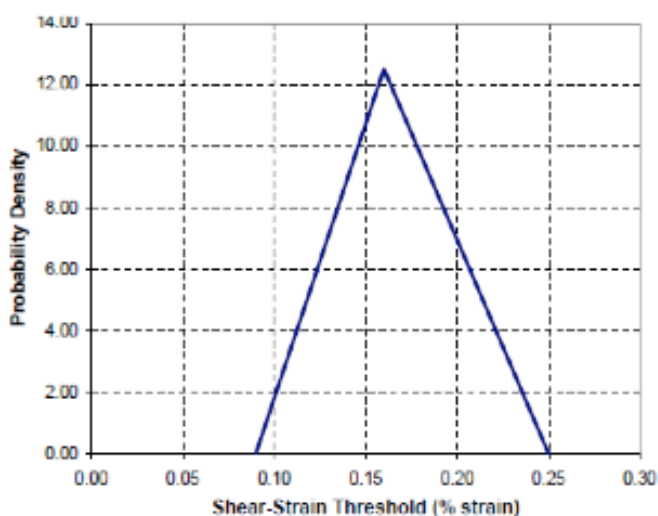

Figure III-6. Plot showing probability distribution of threshold shear strain for Topopah Spring lithophysal rock.

3.3   Analysis of Expected Failure Observations if Threshold Shear Strains are Exceeded

3.3.1   Method of Analysis using the PFC Model

Numerical micromechanical models were used to better understand the mechanics of deformation and failure of lithophysal tuff and to extrapolate laboratory results to loading conditions, lithophysal content, and scales that could not be tested in the laboratory or in the field. In addition, numerical simulation allows full control and monitoring of the testing process (for example, evolution of damage in the sample from microfractures to observable macrofractures and sample failure). In this analysis, the PFC2D program (Itasca, 2002) was used to simulate the compression and failure mechanism of tuff samples with and without lithophysal voids (BSC, 2004a). The PFC2D program represents a rock mass as an assemblage of circular (2D) particles which are bonded at their contacts with shear and tensile strength. If the strength is exceeded, fracture occurs and the resulting particle contact is frictional. The contact strength and stiffness properties of the PFC2D model of the lithophysal rock mass was first calibrated to reproduce the mechanical behavior observed in the laboratory compression tests on samples of nonlithophysal rock (matrix groundmass only) and on tests with particular lithophysal porosity as determined for the laboratory samples. The numerical models,

however, clearly demonstrate the controlling impact of lithophysal voids on strength and elastic modulus, and show the same trends in strength and modulus with porosity as observed in the laboratory.

3.3.2 Numerical Testing of Fracture Growth on Synthetic Lithophysal Samples

Once the properties of the PFC2D particle bonds were calibrated to reproduce the moduli, uniaxial compressive strength and general post peak softening response obtained from laboratory results, the model was used to examine the fracturing response of rock masses with a range of lithophysae shape and porosities. Figure III-7 illustrates the typical fracturing predicted by the calibrated PFC2D model occurring in a simulated ("synthetic") lithophysal rock sample that has been stressed to failure under uniaxial compression. In this simplest of lithophysal models, the voids are represented as circular holes distributed throughout the sample to achieve a desired porosity. The rock matrix in this model is composed of several thousand circular particles (too small to be seen at this scale) which are bonded with tensile and shear bonds at their contacts. Fractures, which occur due to breakage of these contact bonds when the sample is stressed, can be seen as red and blue lines at the contact location. At the peak stress point, there usually is considerable damage (shown by the fractures represented as blue lines in fig. III-7). Analyses of compression of synthetic rock samples show that stress-induced fractures would be expected to interconnect the lithophysae, which act as locations of stress concentration within the mass. This form of predicted fracture development—ubiquitous, long interlithophysal fracturing— would allow such fractures to be distinguished in underground observations from typical short and discontinuous cooling fractures.
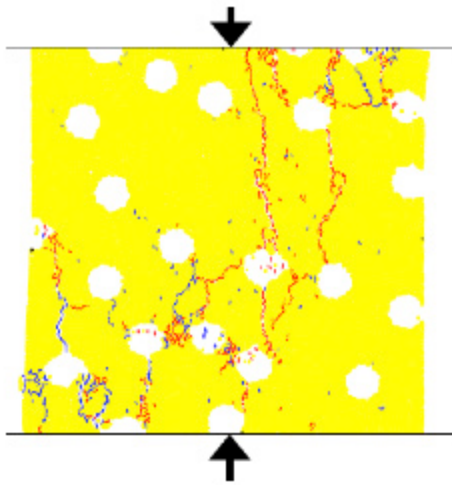

Figure III-7. Example of output from PFC2D model of a lithophysal rock mass and fracturing after peak strength of the sample is reached in uniaxial compression. Lithophysae are represented in this simplified model as circular voids. The blue lines are contact breaks (fractures) formed prior to peak strength and red lines after peak strength. Red lines internal to lithophysae are particles that have broken off from the lithophysae sidewall and fallen into the void. From BSC (2005, figure 6–4).

3.3.3 Application of Model to Examine Expected Fracture Growth in Field-Scale Geometries

The calibrated PFC2D model was then applied to study fracture growth in complex and realistic lithophysae geometries. The field lithophysae panel maps were digitized to create field-representative PFC2D models which were then subjected to a variety of loading conditions to failure. Figure III-8 shows lithophysae panel map in the Tptpll from which a series of PFC2D digitized models have been created (BSC 2004a, section 9.1, attachment V). These models were subject to uniaxial compression to

determine the mode of fracturing that occurs at various levels of shear-strain. The observed ubiquitous short, discontinuous fractures in the matrix groundmass are highlighted in the geologic panel map shown in figure III-8. These fractures clearly are not through-going, have not experienced shearing or offset, and do not interconnect lithophysae, and were judged to be formed during the cooling process shortly after deposition. The result of the numerical compression experiments indicate that relatively long fractures connecting lithophysae begin to form prior to peak strength, and that major shearing fractures that intersect lithophysae boundaries form and extend in the post-peak strain range. It is clear from the numerical modeling results that observable macro-fracturing that intersects lithophysae (and may offset surfaces of the lithophysae) should be visible at strain levels prior to and at peak strength of the rock mass, as indicated in figure III-7. These features are not observable in field observations, and thus it can be assumed that the rock mass has never reached these strain levels in the geologic past.
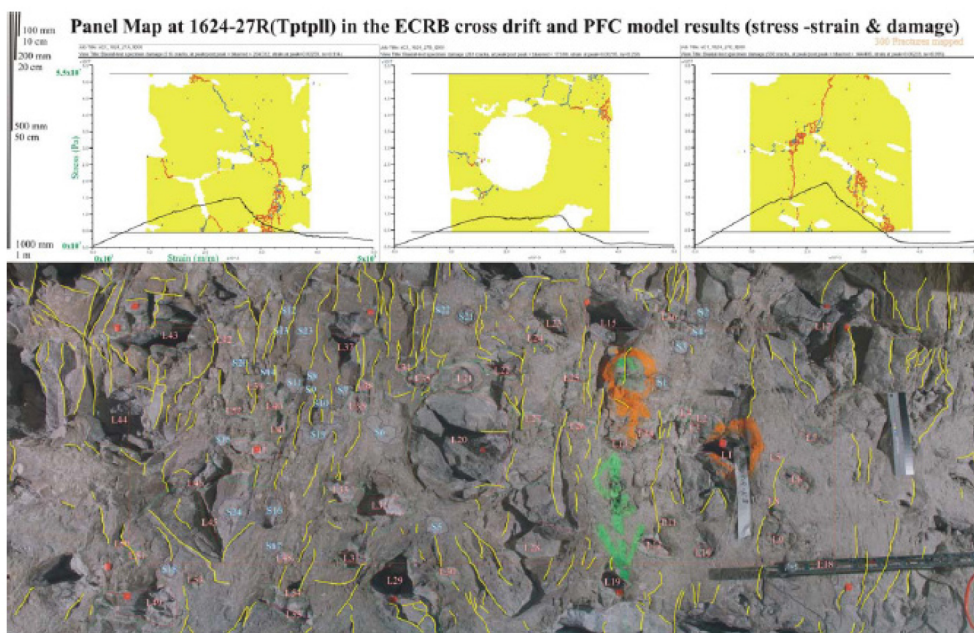
Sources: DTN: GS021008314224.002 [DIRS 161910]; BSC (2003 [DIRS 166660], Attachment V- Appendix B, Figure B-4).

NOTE: Upper part of figure shows stress-strain model results (BSC 2004 [DIRS 172334]) using the software code PFC2D. Blue lines are micro-fractures formed prior to failure at peak strength and red lines are micro-fractures formed post-failure at peak strength. Embedded lithophysae are derived from stencils taken from the panel map below. The lower part of the figure is the panel map at 16+24 on the right wall with 300 photographically interpreted fractures (yellow lines).

Figure III-8.   Three screenshots of PFC2D models created by "stenciling" lithophysae from the 16+24 geologic panel map in the Tptpll. The PFC models show the types of fractures generated by rock mass failure. The panel map, bottom, indicates the observed fractures (interpreted as cooling fractures), in yellow. Completely absent are major, interlithophysal fractures expected if the rock mass had undergone failure-level shear strains.

4.0   Development of a Bounded Horizontal PGV Hazard Curve for the Yucca Mt. Site

4.1   Site Response Modeling and Development of Bounded PGV Distributions

A site response model for Yucca Mountain has been developed and modeling conducted to define the horizontal PGV and dynamic strains induced in the rock mass from ground surface to the depth of the repository host horizon over the postclosure period (BSC, 2004b). BSC (2005) presents further site response modeling in which numerous combinations of the input parameters to the model

and the range of earthquakes that contribute to the annual exceedance frequency at a given level of ground motion are simulated. The following summary is taken from BSC (2005), pages 6–19 and 1–20.

Three earthquakes represent the range of magnitudes for each of the two frequency ranges, resulting in six earthquakes for each component of ground motion (the deaggregation earthquakes) that form the control motion for the site-response model. Finally, both vertically propagating seismic waves and inclined seismic waves were considered in the modeling process. Uncertainty in the physical properties of the rock mass is incorporated through use of alternate base-case velocity profiles and alternate base-case sets of dynamic material property curves. Variability is incorporated by stochastically varying the velocity profiles and dynamic material property curves about their base case.

The uncertainty and variability in the base-case properties translates into uncertainty in the level of horizontal PGV that is associated with a particular shear-strain threshold. For each combination of base-case velocity profile (P1 or P2), base-case dynamic property curves (for the Upper Mean Tuff [UMT] or Lower Mean Tuff [LMT]), and wave propagator type (inclined or vertically incident), site response is determined using the deaggregation earthquakes as the input control motion. For a given combination, each deaggregation earthquake control motion is propagated through 60 randomized velocity profiles with associated randomized dynamic property curves producing 60 curves of horizontal PGV and shear strain versus depth. Results for the three deaggregation earthquakes associated with each frequency range (5 to 10 Hz and 1 to 2 Hz) are combined and then median PGV and median dynamic shear strain values versus depth are determined. To characterize the median PGV and dynamic shear strain for the lithophysal units, PGV and strain are averaged for the depth range from 290 to 392 m (951 to 1,286 ft), the average depth range of the lower lithophysal unit of the Topopah Spring Tuff wave propagators (vertical and inclined) are then averaged resulting in eight pairs of PGV and shear strain corresponding to the combinations examined (1 to 2 Hz/P1/UMT, 1 to 2 Hz/P1/LMT, 1 to 2 Hz/P2/UMT, 1 to 2 Hz/P2/LMT, 5 to 10 Hz/P1/UMT, 5 to 10 Hz/P1/LMT, 5 to 10 Hz/P2/UMT, 5 to 10 Hz/P2/LMT). This process is carried out for 4 hazard levels (10^{-4}/yr, 10^{-5}/yr, 10^{-6}/yr, 10^{-7}/yr) resulting in a suite of values associating horizontal PGV and dynamic shear strain (Table 2). In addition to the 8 pairs of shear strain and corresponding horizontal PGV values determined for the 4 hazard levels and the results also used to linearly interpolate or extrapolate horizontal PGV values for target values of shear strain (0.05, 0.10, 0.20, 0.30, 0.40, and 0.50 percent; table III-2).These results are expressed in terms of probability density functions for bounding horizontal PGV for each of the base-case velocity profiles and tuff properties (fig. III-9). For the LMT grouping of distributions, shear strains associated with the shear-strain threshold distribution are generated at relatively lower ground motions (about 100 to 230 cm/s). For the UMT grouping of distributions, higher ground motions (about 180 to 490 cm/s) are needed to generate the shear-strain threshold level of shear strains.

Table III-2. Modeled and interpolated horizontal peak ground velocity for shear strain values.

[From BSC (2005), table 6-3]

Annual Frequency of Exceedance (1/yr)	Velocity Profile P1 + Upper Mean Tuff Dynamic Material Property Curves + 1 to 2 Hz		Velocity Profile P1 + Lower Mean Tuff Dynamic Material Property Curves + 1 to 2 Hz		Velocity Profile P2 + Upper Mean Tuff Dynamic Material Property Curves + 1 to 2 Hz		Velocity Profile P2 + Lower Mean Tuff Dynamic Material Property Curves + 1 to 2 Hz	
	Modeled Horizontal Peak Ground Velocity (cm/sec)	Modeled Shear Strain (γ_{yz}, %)	Modeled Horizontal Peak Ground Velocity (cm/sec)	Modeled Shear Strain (γ_{yz}, %)	Modeled Horizontal Peak Ground Velocity (cm/sec)	Modeled Shear Strain (γ_{yz}, %)	Modeled Horizontal Peak Ground Velocity (cm/sec)	Modeled Shear Strain (γ_{yz}, %)
1×10^{-4}	45.26	0.020	47.27	0.023	45.17	0.018	43.67	0.024
1×10^{-5}	110.67	0.050	104.48	0.076	111.40	0.048	105.82	0.089
1×10^{-6}	242.65	0.118	231.98	0.263	244.31	0.116	231.41	0.331
1×10^{-7}	512.01	0.270	499.27	0.869	519.61	0.272	494.90	1.041

	Velocity Profile P1 + Upper Mean Tuff Dynamic Material Property Curves + 5 to 10 Hz		Velocity Profile P1 + Lower Mean Tuff Dynamic Material Property Curves + 5 to 10 Hz		Velocity Profile P2 + Upper Mean Tuff Dynamic Material Property Curves + 5 to 10 Hz		Velocity Profile P2 + Lower Mean Tuff Dynamic Material Property Curves + 5 to 10 Hz	
	Modeled Horizontal Peak Ground Velocity (cm/sec)	Modeled Shear Strain (γ_{yz}, %)	Modeled Horizontal Peak Ground Velocity (cm/sec)	Modeled Shear Strain (γ_{yz}, %)	Modeled Horizontal Peak Ground Velocity (cm/sec)	Modeled Shear Strain (γ_{yz}, %)	Modeled Horizontal Peak Ground Velocity (cm/sec)	Modeled Shear Strain (γ_{yz}, %)
1×10^{-4}	31.63	0.016	29.65	0.018	31.33	0.016	30.00	0.021
1×10^{-5}	99.29	0.051	93.24	0.072	99.70	0.049	93.86	0.085
1×10^{-6}	246.20	0.124	237.70	0.276	249.51	0.127	235.68	0.351
1×10^{-7}	520.46	0.286	522.41	0.905	540.36	0.297	518.23	1.089

Target Shear Strain Values (γ_{yz}, %)	Velocity Profile P1 + Upper Mean Tuff Dynamic Material Property Curves + 1 to 2 Hz — Interpolated/Extrapolated Horizontal Peak Ground Velocity (cm/sec)	Velocity Profile P1 + Lower Mean Tuff Dynamic Material Property Curves + 1 to 2 Hz — Interpolated/Extrapolated Horizontal Peak Ground Velocity (cm/sec)	Velocity Profile P2 + Upper Mean Tuff Dynamic Material Property Curves + 1 to 2 Hz — Interpolated/Extrapolated Horizontal Peak Ground Velocity (cm/sec)	Velocity Profile P2 + Lower Mean Tuff Dynamic Material Property Curves + 1 to 2 Hz — Interpolated/Extrapolated Horizontal Peak Ground Velocity (cm/sec)
0.05	110.67	76.09	115.92	68.38
0.10	208.44	120.67	213.93	111.34
0.20	388.85	188.96	392.95	163.43
0.30	566.06	248.31	568.86	215.52
0.40	743.27	292.46	744.78	257.18
0.50	920.48	336.60	920.69	294.27

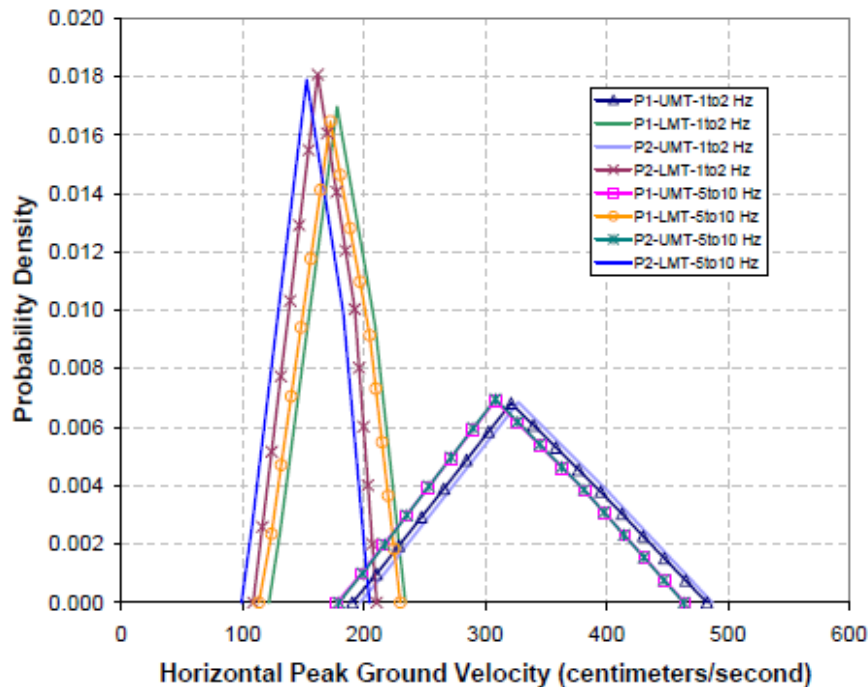| Target Shear Strain Values (γ_{yz}, %)	Velocity Profile P1 + Upper Mean Tuff Dynamic Material Property Curves + 5 to 10 Hz — Interpolated/Extrapolated Horizontal Peak Ground Velocity (cm/sec)	Velocity Profile P1 + Lower Mean Tuff Dynamic Material Property Curves + 5 to 10 Hz — Interpolated/Extrapolated Horizontal Peak Ground Velocity (cm/sec)	Velocity Profile P2 + Upper Mean Tuff Dynamic Material Property Curves + 5 to 10 Hz — Interpolated/Extrapolated Horizontal Peak Ground Velocity (cm/sec)	Velocity Profile P2 + Lower Mean Tuff Dynamic Material Property Curves + 5 to 10 Hz — Interpolated/Extrapolated Horizontal Peak Ground Velocity (cm/sec)
0.05	97.74	67.48	100.73	58.98
0.10	198.04	113.13	197.97	101.63
0.20	375.26	183.91	374.89	155.04
0.30	545.08	248.56	545.47	208.44
0.40	714.90	293.83	716.06	254.44
0.50	884.72	339.09	886.64	292.73

Figure III-9. Plot showing probability distributions of bounding horizontal peak ground velocities for two frequency ranges for base case velocity profiles (P1 and P2) and tuff properties ranges (Upper Mean Tuff and Lower Mean Tuff) as determined from the Yucca Mountain Project site response model. In the legend, the notations refer to the various combinations of repository block velocity profile (P1, P2), dynamic material property curves (Upper Mean Tuff (UMT) and Lower Mean Tuff (LMT)), and response spectrum frequency range (1 to 2 Hz and 5 to 10 Hz). From BSC (2005), figure 6-8.

4.2   Development of a Bounded Horizontal PGV Hazard Curve for Yucca Mountain

To obtain a bounded hazard curve, the triangular distributions for the bounding value of horizontal PGV (fig.III-9) are combined with the unbounded hazard curve derived from the Yucca Mountain PSHA (BSC, 2004b) to generate a new composite hazard curve for the repository horizon. The process used to develop the bounded hazard curve involves two steps. First, each of the 8 bounding horizontal PGV distributions is combined individually with the unbounded hazard curve for the waste emplacement level to produce eight modified mean hazard curves. Then for each value of horizontal PGV, the probabilities of the eight modified curves are averaged (arithmetic mean) to determine points on the final modified mean hazard curve (fig. III-10, top). Equal weighting of the hazard curves is used to reflect the current assessment that the underlying cases representing epistemic uncertainty in site conditions are equally likely to represent actual conditions at Yucca Mountain. The unbounded hazard curve and the composite mean hazard curve reflecting the bound to horizontal PGV are shown in figure III-10, bottom.
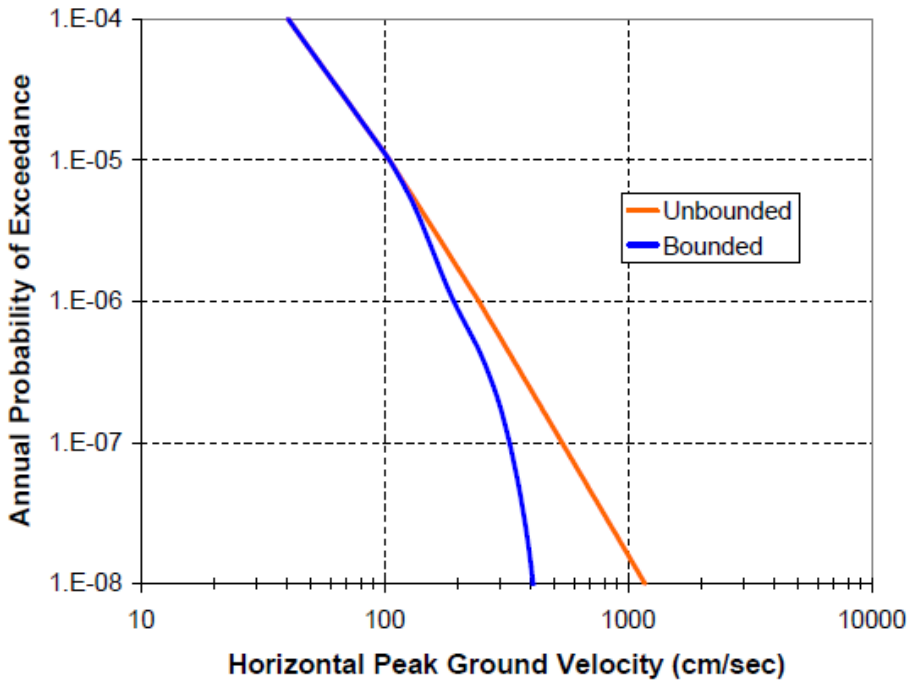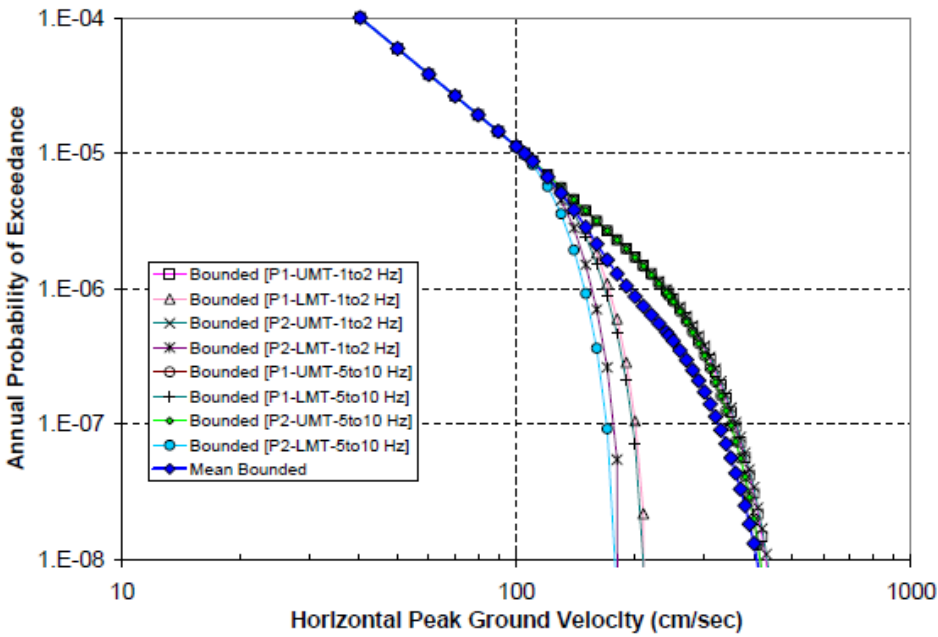
Figure III-10. Plots showing individual and average bounded peak ground velocity (PGV) hazard curves for the waste emplacement level (top) and comparison of the horizontal PGV hazard curves for the bounded and unbounded cases for the waste emplacement level (bottom). The eight hazard curves result from combining the unbounded hazard curve with the eight "triangular" bounds to horizontal PGV. The eight "triangular" bounds represent epistemic uncertainty in the site-response modeling. The Mean Bounded curve represents the average of the other eight curves.From BSC (2005), figures 6-9 and 6-10.

References

BSC (Bechtel SAIC Company), 2004a, Drift degradation analysis, ANL-EBS-MD-000027, Rev. 03,: Las Vegas, Nevada, Bechtel SAIC Company, doi: 10.2172/837516.

BSC (Bechtel SAIC Company), 2004b, Development of earthquake ground motion input for preclosure seismic design and postclosure performance assessment of a geologic repository at Yucca Mountain, Nev., MDL-MGR-GS-000003, Rev. 01: Las Vegas, Nevada, Bechtel SAIC Company, doi:2172/837491.

Case, J.B., and Buesch, D.C., 2004, Simulation of ventilation efficiency and preclosure temperatures in emplacement drifts at Yucca Mountain, Nevada, Using Monte Carlo and Composite Thermal-Pulse Methods *in* 2004 ASME Heat Transfer/Fluid Engineering Summer Conference, July 11-15, 2004, Charlotte, North Carolina: American Society of Mechanical Engineers, p. 1–7.

Itasca Consulting Group, 2002, Itasca software–cutting edge tools for computational mechanics: Minneapolis, Minnesota, Itasca Consulting Group.

Reiter, L., 2004, When are ground motion estimates too high?: Seismological Research Letters, v. 75, no. 2, p. 282.

Sawyer, D.A. Fleck, R.J. Lanphere, M.A. Warren, R.G. Broxton, D.E. and Hudson, M.R., 1994, Episodic caldera volcanism in the Miocene southwestern Nevada Volcanic Field—revised stratigraphic framework, 40Ar/39Ar geochronology, and implications for magmatism and extension: Geological Society of America Bulletin, v. 106, no. 10, p. 1304–1318.